

**ROCK-PHYSICS AND 3C-3D SEISMIC ANALYSIS FOR  
RESERVOIR CHARACTERIZATION: MARCELLUS  
SHALE, PENNSYLVANIA**

---

A Thesis Presented to  
the Faculty of the Department of Earth and Atmospheric Sciences  
University of Houston

---

In Partial Fulfillment  
of the Requirements for the Degree  
Master of Science

---

By  
Fabiola del Valle Ruiz Pelayo

May 2016

**ROCK-PHYSICS AND 3C-3D SEISMIC ANALYSIS FOR  
RESERVOIR CHARACTERIZATION: MARCELLUS  
SHALE, PENNSYLVANIA**

---

Fabiola del Valle Ruiz Pelayo

APPROVED:

---

Dr. Robert R. Stewart, Chairman  
Dept. of Earth and Atmospheric Sciences

---

Dr. John P. Castagna  
Dept. of Earth and Atmospheric Sciences

---

Dr. Richard Verm  
Geokinetics Inc.

---

Dean, College of Natural Sciences and Mathematics

To my angels, Carmen Zamora and Olga Perez de Ruiz,  
To my parents, Morelia Pelayo and Jose Felix Ruiz,  
Gracias.

# Acknowledgements

I would like to express my deepest gratitude to my advisor Dr. Robert Stewart. Thank you for letting me become part of the Allied Geophysical Laboratories (AGL) group and for your continuous support during my Master studies. Thank you for taking the time to listen to my ideas, for your guidance, patience, and for always encouraging us to improve our work and seek excellence.

Special thanks go to Dr. John Castagna. Thank you for always being available, for your insightful advice and enlightening discussions. Thank you for your enthusiasm and for always making geophysics exciting.

I would like to thank Dr. Richard Verm from Geokinetics Inc. for accepting to be part of my committee and for providing the seismic data for this work. Thanks to Anadarko, Chesapeake and the Pennsylvania Department of Conservation and Natural Resources (DCNR) for providing the well log and VSP data. Thanks to Schlumberger, CGG-HR, and Ikon Science for providing the software used in this project.

I would like to acknowledge Angel Zea, Ramses Meza, and Daniel Naval for their help with PROMC and gather conditioning. Special thanks go to Venkatesh Anantharamu for his patience and disposition to help me with RokDoc.

I would like to thank my friends and colleagues Alberto Bernaez, Lourdes Rodriguez, Mari Tesi, Daniel De Lilla, Joan Marie Blanco, Karilys Castillo, and Orietta Mata. I thank you for your assistance, encouragement, and for the fun we had all

these years.

Many thanks to all the AGL'ers for their support and for being wonderful office-mates. Special thanks to Long Huang for helping me with Vista and answering ALL my LaTeX questions, and Elita de Abreu for answering my rock-physics questions and sharing her knowledge with me.

I would like to thank my family for their spiritual support and for always believing in me. Thanks to my not so little sister, Andrea Ruiz, for your wisdom and for always having the right word at the right time.

I would have not being here writing this thesis without my parents, Morelia Pelayo, and Jose Felix Ruiz. Thank you for your continuous effort and for always helping me achieve everything I have wanted in life. I have no words to express my gratitude to you. My only hope is always to make you proud. Gracias.

Finally, I want to thank my love and life companion, William Marin. This work would not have been possible without you. Thank you for always being with me every step of the way and in every single moment of stress and happiness. Thank you for your patience and for answering all my questions. Thank you for your love, understanding, and for making me believe I could finish this work.

**ROCK-PHYSICS AND 3C-3D SEISMIC ANALYSIS FOR  
RESERVOIR CHARACTERIZATION: MARCELLUS  
SHALE, PENNSYLVANIA**

---

An Abstract of a Thesis

Presented to

the Faculty of the Department of Earth and Atmospheric Sciences

University of Houston

---

In Partial Fulfillment

of the Requirements for the Degree

Master of Science

---

By

Fabiola del Valle Ruiz Pelayo

May 2016

# Abstract

The elastic properties (density and velocity) of organic shales are largely controlled by kerogen content, porosity, clay content, and effective pressure. Since surface-seismic measurements can have a complicated dependence on rock properties, it is essential to understand the relationship between the elastic response and variations in rock properties to correctly assess the target reservoir. In this sense, a combination of rock-physics and seismic modeling is applied to relate variations in key properties, such as kerogen content and porosity, to differences in the elastic response of a 3C-3D seismic volume in the Marcellus Shale (Bradford County, Pennsylvania). Well log analysis and rock physics modeling indicate that density is more sensitive to kerogen content than  $V_p/V_s$  or P-impedance. Organic-rich intervals (kerogen content  $> 6$  wt. %) are characterized by densities lower than 2.5 g/cc.  $V_p/V_s$  and P-impedance are more sensitive to variations in clay content than density;  $V_p/V_s$  values lower than 1.6 are attached to clay content lower than 25 %. The interplay between mineralogy and kerogen content causes an increase in velocity in the organic-rich interval, where the effect of kerogen on the elastic moduli seems to be masked by a decrease in clay content and increase in quartz and calcite. Elastic AVA modeling shows that the sensitivity to the presence of the organic-rich facies increases with angle for both PP and PS (converted-wave) reflections. Additionally, the compressibility seems to be more sensitive to the organic-rich facies than the rigidity. A comparison between PP and PP-PS inversions show that the addition of PS data decreases the P-impedance, S-impedance and density estimation errors by 58, 80, and 17 %, respectively. We used this procedure to create 3D-density maps to

indicate promising reservoir quality. These predictions suggest good reservoirs where two gas wells (not used in the analysis) are producing.

# Contents

<b>1</b>	<b>Introduction</b>	<b>1</b>
1.1	Marcellus Shale . . . . .	1
1.2	Motivation . . . . .	8
1.3	Objectives . . . . .	9
1.4	Available data . . . . .	9
1.4.1	Seismic data . . . . .	9
1.4.2	Well-log data . . . . .	14
1.4.3	Software . . . . .	15
<b>2</b>	<b>Well-log analysis and petrophysical properties</b>	<b>17</b>
2.1	Clay volume estimation . . . . .	21
2.2	TOC estimation . . . . .	26
2.3	Total porosity estimation . . . . .	33
2.4	Cross-plot analysis . . . . .	37
2.5	Brittleness estimation . . . . .	48
2.6	Seismic and rock-physics modeling . . . . .	53
2.6.1	AVO seismic modeling . . . . .	53
2.6.2	Rock-physics model . . . . .	59
<b>3</b>	<b>Seismic interpretation</b>	<b>71</b>

3.1	PP seismic interpretation . . . . .	71
3.1.1	Well-to-seismic tie and seismic resolution . . . . .	71
3.1.2	Geometric attributes . . . . .	77
3.2	PP and PS joint interpretation . . . . .	82
<b>4</b>	<b>Seismic Inversion</b>	<b>93</b>
4.1	PP-PS registration . . . . .	97
4.2	PP-PS post-stack joint inversion . . . . .	102
4.3	Comparison between PP pre-stack inversion and PP-PS pre-stack joint inversion . . . . .	116
4.4	Identification of high-TOC and brittle facies . . . . .	120
<b>5</b>	<b>Conclusions, recommendations, and future work</b>	<b>131</b>
5.1	Recommendations and future work . . . . .	133
	<b>Appendices</b>	<b>134</b>
	Appendix A PP seismic gather conditioning	136
	Appendix B PS seismic gather conditioning	147
	<b>References</b>	<b>154</b>

# List of Figures

1.1	Comparison between natural gas production of different shale gas plays in the U.S from April 2015 to April 2016 (EIA Drilling Productivity Report, March 2016). . . . .	2
1.2	Map showing the boundary of the Interior Marcellus Assessment Unit (AU) in the Appalachian Basin Province. The Interior Marcellus AU is generally defined by shale thickness greater than or equal to 50 ft (U.S. Geological Survey Assessment of the Middle Devonian Marcellus Shale of the Appalachian Basin Province, 2011). . . . .	3
1.3	Map of Marcellus Shale thickness in Pennsylvania. Bradford County is outlined in black and the approximate location of the 3D-3C survey is outlined in red (Modified from Piotrowski and Harper, 1979). . . .	4
1.4	Stratigraphic chart and a section of the P-wave stacked seismic data showing the seismic expression of the Middle Devonian units, specifically the top and base of the Tully limestone and the Marcellus interval (Upper Marcellus and Lower Marcellus). . . . .	5
1.5	Ternary plot showing the characteristics of the mineral composition and organic matter richness and the classification method of Marcellus Shale lithofacies based on core data. The organic-rich facies are characterized by TOC values higher than 6.5% wt, indicated by the warmer colors (From Wang, 2012). . . . .	6
1.6	Regional distribution of the J1 and J2 joint sets in Pennsylvania. The red box shows the approximate study area (modified from Smith and Leone, 2010). . . . .	7
1.7	Crosscutting J1 and J2 joints in the Marcellus black shale exposed in Oatka Creek, Le Roy, New York. View is to the eastnortheast (From Engelder et al., 2009). . . . .	8

1.8	Base map showing the location of the VSP calibration well (OTIS 2H) relative to planned positions of source and receiver stations used for 3C-3D seismic survey (From Hardage et al., 2011). . . . .	11
1.9	Comparison between the P-wave cdp gathers and the PS1 ccp gathers in their native times, at an inline going through the well OTIS 2H location (well path shown in red). Both volumes show high- and low-frequency noise as well as multiples that need to be attenuated. . . .	13
1.10	Comparison between the P-wave and PS1 stacked sections in their native times. The red polygon encloses the target interval: around 1,000 ms for the P-wave section and around 1,300 ms for the PS1 section. . . . .	14
1.11	Base map showing the location of the available wells and the 3D-seismic volume (outlined in red). . . . .	15
2.1	West-east cross-section going through the available wells (flattened at the Stafford top), showing the total gamma-ray log in the first track and the uranium (U) and density (RHOB) logs in the second track. The Marcellus Shale interval can be easily recognized in total gamma-ray logs (highlighted by the red polygon), showing an increase in radioactivity, which translates in API values higher than 150 API in this wells, compared to the inorganic Hamilton shale (highlighted by the brown polygon). Areas with high TOC and potential for gas accumulation are highlighted in red (U-RHOB crossover) . . . . .	20
2.2	OTIS 2H well logs. From left to right, total GR and the corrected GR (thick black curve), uranium, potassium, and thorium content, neutron porosity and density, and the comparison between both clay volumes ( $V_{clay_{PHI}}$ and $V_{clay_{PHI}}$ ) estimated for the OTIS 2H well. Clay volumes calculated with the two different methods show very similar results, and both follow the separation trend between NPHI and RHOB: the higher the separation, the higher the clay volume. . . .	23
2.3	Cross-plot between the clay volumes calculated in the Upper and Lower Marcellus intervals at OTIS 2H using the porosity logs ( $V_{clay_{PHI}}$ ) and the corrected GR log ( $V_{clay_{CGR}}$ ), colored by GR. The linear regression has a correlation coefficient ( $R^2$ ) of 0.83, which indicates a very good agreement between both curves . . . . .	24

2.4	Cross-plot between density and PEF for the Upper and Lower Marcellus intervals. Both intervals show low densities ( $< 2.75$ g/cc) and low-PEF values ( $< 8$ b/e), indicating a marginal pyrite content . . . .	25
2.5	Cross-plot between potassium and thorium for clay classification in the Upper and Lower Marcellus intervals (green and red samples, respectively). The clay mineralogy in the Marcellus Shale seems to be dominated by illite, however there are also smectite-illite mixed clays	29
2.6	Comparison between the TOC estimations at the EICK 1H and OTIS 2H wells. From left to right, total gamma-ray (GR) and uranium-corrected gamma-ray (GRC), uranium (U), potassium (K), and thorium (Th), comparison between the TOC curves, and the resistivity (RT)-density (RHOB) overlay for $\Delta \log R$ calculation, where areas highlighted in blue correspond to high organic-matter zones. Note the good agreement between the TOC curves, where high TOC values are associated with high GR, high U, high RT, and low RHOB. . . . .	31
2.7	Correlation between TOC curves estimated by (a) Passey and PNS, (b) Vernik and PNS, and (c) multi-variate regression and PNS at the EICK 1H well. Samples are colored by uranium values. There highest correlation is found for the TOC curve estimated through multi-variate regression. However, they all show consistent estimations for the high TOC area (6 to 7 wt. %). . . . .	32
2.8	TOC vs. density cross-plot for EICK 1H (the well that has TOC calculated through PNS) in the Upper and Lower Marcellus intervals. Samples are colored by uranium values. Note the correlation between high uranium, low density, and high TOC content. . . . .	33
2.9	Schematic of a clay-rich organic rock solid, water, and hydrocarbons. Modified from Asquith (2014). . . . .	34
2.10	OTS 2H well logs. From left to right, total gamma-ray (GR), uranium (U), potassium (K), and thorium (Th), comparison between density (RHOB) and neutron porosity (NPFI), TOC estimation using multi-variate analysis and total porosity (PHIT) estimation. . . . .	36

2.11	Vp vs. Vs cross-plot for EICK 1H, THOMAS 1H, and OTIS 2H, color-coded by (a) formation and (b) GR. Note how both Upper and Lower Marcellus deviate from the Castagnas mudrock line (Castagna et al., 1985) towards lower velocities. This could be caused by both gas saturation and TOC content. The excellent correlation between Vp and Vs allows an adequate linear fit. . . . .	38
2.12	Density vs. Vp crossplot for EICK 1H, THOMAS 1H, and OTIS 2H, color coded by (a) formation and (b) GR. Note the lithological trend, where the Upper and Lower Marcellus organic-rich shale can be easily identified in the density domain, showing values lower than 2.65 g/cc.	39
2.13	Density vs. Vp cross-plots for the Marcellus interval, including the wells EICK 1H, THOMAS 1H and OTIS 2H. Cross-plots are color-coded by (a) TOC (PNS TOC for the EICK 1H well and Vernik and Landis' TOC for OTIS 2H and THOMAS 1H), (b) Vclay, (c) unit and (d) well. The high TOC interval correlate to low densities, high velocities and low-clay content, and are separated in a unit called "Hot" Lower Marcellus, enclosed by the black polygons. . . . .	41
2.14	Density vs. Vp/Vs cross-plots for the Marcellus interval, including the wells EICK 1H, THOMAS 1H and OTIS 2H. Cross-plots are color-coded by (a) TOC (PNS TOC for the EICK 1H well and Vernik and Landis' TOC for OTIS 2H and THOMAS 1H), (b) Vclay, (c) unit and (d) well. The black polygon encloses the low-density organic-rich "Hot" Lower Marcellus interval, with TOC values higher than 6 wt. %. Vp/Vs and is a good lithological indicator, showing an increase in their values as clay content increases. . . . .	43
2.15	Density vs. acoustic impedance (AI) cross-plots for the Marcellus interval, including the wells EICK 1H, THOMAS 1H, and OTIS 2H. Cross-plots are color-coded by (a) TOC (PNS-TOC for the EICK 1H well and Vernik and Landis' TOC for OTIS 2H and THOMAS 1H), (b) Vclay, (c) unit and (d) well. The black polygon encloses the low-density organic-rich "Hot" Lower Marcellus interval, with TOC values higher than 6 wt. %. Acoustic impedance is also a good lithological indicator, showing an increase in their values as clay content increases.	45

2.16	Comparison between THOMAS 1H and OTIS 2H well-logs. The Upper Marcellus shows high clay content, low total porosities and low TOC content, while the Lower Marcellus shows low clay content, high total porosities and high TOC. Lower Marcellus has more brittle mineral content (e.g. quartz and calcite) than the Upper Marcellus and it could be more amenable to open and maintain fractures during hydraulic fracturing. . . . .	46
2.17	Acoustic impedance vs. poisson's ratio (a) and $\lambda\rho$ vs. $\mu\rho$ (b) cross-plots of the Marcellus interval, colored by unit. The "Hot" Lower Marcellus unit (black) cannot be easily discriminated in any of these domains. . . . .	48
2.18	Well section through the THOMAS 1H, EICK 1H, and OTIS 2H wells, showing a comparison between the mineral volumes (third track) and the brittleness indexes (fourth track) derived using $E\rho/\nu$ (blue curve), Rickmans formulation (magenta curve) and the mineral volumes (green curve). The fifth track shows the $E\rho$ calculation for comparison. . . . .	52
2.19	Comparison between the original Vp, Vs, density, P-impedance (AI) and S-impedance (SI) logs from the OTIS 2H well (black) and the edited logs (red). The red polygon encloses the low TOC upper part of the Lower Marcellus and the grey polygon the high TOC "Hot" Lower Marcellus. . . . .	55
2.20	Comparison between the PP AVO synthetic gathers generated with the original logs (left) and the edited logs (right). The amplitudes picked at the Lower Marcellus trough are seen in the AVA plot. The red and blue AVA curves correspond to the amplitudes picked in the synthetic generated using the original and the edited logs, respectively. Both synthetics show negative intercept and positive gradient, that is, the amplitude becomes less negative with offset (AVO Class IV). . . .	57
2.21	Comparison between the PS AVO synthetic gathers generated with the original logs (left) and the edited logs (right). The amplitudes picked at the Lower Marcellus trough are seen in the AVA plot. The red and blue AVA curves correspond to the amplitudes picked in the synthetic generated using the original and the edited logs, respectively.	58
2.22	Incidence angle vs. amplitude percentage difference. The percentage corresponds to the difference between the AVA curves seen in Figures 2.20 and 2.21 for the PP (a) and PS (b) synthetic seismograms. . . .	59

2.23	Example of the variations in the effective bulk moduli resulting from adding quartz to a clay matrix using different number of steps (1 to 100) (a) and the percentage difference between the results (b). . . . .	61
2.24	Difference between incrementally adding 20 % quartz (aspect ratio = 0.1) and 20 % kerogen (aspect ratio = 0.01) to a clay matrix in 100 steps starting with quartz first (black line) and then with kerogen first (magenta line). A zoom-in is seen in (b), where the difference between the two lines can be better depicted. . . . .	62
2.25	Backscattered electron image of Marcellus Shale showing the difference in aspect ratio between the compliant matrix-related pores and the rounded (stiffer) kerogen-related pores. (From Curtis et al., 2012) . . .	63
2.26	OTIS 2H well showing the gamma-ray and uranium logs, the mineral volumes (including the kerogen volume), the facies classification and the total porosity log. Facies are defined in terms of porosity, clay volume, and TOC content. The black facies represents porosities lower than 3 % and clay volumes higher than 35 %, red and cyan facies indicate clay content lower than 35 % and porosities lower and higher than 5 %, respectively, the blue facies are the interbedded limestones (including the Cherry Valley limestone), and the green facies represents TOC content higher than 10 % (in volume), porosities higher than 8 % and clay content lower than 25 %. . . . .	66
2.27	P-wave velocity vs. porosity for the Marcellus Shale interval at the OTIS 2H well color-coded by the previously defined facies. The magenta model line is calculated to fit the green "Hot" Lower Marcellus facies and is composed by 15 % clay, 60 % quartz, 10 % calcite, and 15 % kerogen. . . . .	67
2.28	Rock-physics modeling results showing the separate effects of kerogen and clay content variation on density and P-impedance. The OTIS 2H Marcellus Shale well-log data is plotted in the background colored by clay (a) and kerogen (b). . . . .	69
2.29	Rock-physics modeling results showing the separate effects of porosity and clay content variation on density and P-impedance. The OTIS 2H Marcellus Shale well-log data is plotted in the background colored by clay (a) and kerogen (b). . . . .	70

3.1	PP full wavelet and its corresponding frequency spectrum. The full wavelet extraction is performed in a window from 600 to 1035 ms (a 435 ms window length). . . . .	73
3.2	OTIS 2H well-to-seismic tie and VSP comparison. From left to right, tracks show the P-wave, density, and P-impedance logs ( $Z_p$ ), a zero-offset synthetic computed using an 80 Hz Ricker wavelet, the P-wave VSP corridor stack, the P-wave VSP corridor stack filtered (5-10-40-60 Hz bandpass filter), the zero-offset synthetic computed with the wavelet extracted from the seismic, the trace extracted from the real seismic at the well location and the real PP seismic going through the well location. There is an excellent agreement between the synthetics, the corridor stack and the seismic data. . . . .	74
3.3	Wedge model generated using the PP extracted wavelet. The Lower Marcellus (golden color wedge) thickness is varied from 0 (right) to 500 ft (left). The OTIS 2H P-wave log is inserted at the real Lower Marcellus thickness (130 ft). The thin Stafford limestone (62 ft thick) causes a 90° phase-shift in the resulting waveform. At 130 ft thick we are above one-half of the dominant period of the wavelet (peak-to-through time), which corresponds to Widess vertical-resolution limit. . . . .	76
3.4	Arbitrary line running from north to south, showing a series of inverse faults that affect the Marcellus interval. . . . .	77
3.5	Vertical slice through the PP seismic amplitude co-rendered with the most negative curvature. Note how the most negative curvature values are associated with the footwall blocks of the faults. . . . .	79
3.6	Comparison between the most negative curvature co-rendered with similarity extracted at the Onondaga top, and the Onondaga time-structure map. E-W trending faults are easily depicted in the curvature and similarity extractions. The most negative curvature highlights the downthrown side of the faults. The NW-SE lines (parallel to the crossline direction) showing in the curvature are acquisition footprint. . . . .	81
3.7	Comparison between the local azimuth and most negative curvature time-slices at 1000ms, which corresponds to approximately the middle of the Marcellus interval. The local azimuth attribute highlights small east-west and southeast-northwest directions. Both attributes are affected by acquisition footprint. . . . .	82

3.8	PP (green) and PS (blue) full wavelets and their corresponding frequency spectrum. The extractions were performed in a window from 800 to 1400 ms for the PS volume and from 600 to 1035 ms for the PP volume. The PS frequency spectrum shows a higher peak frequency than the PP spectrum. . . . .	84
3.9	PS data well tie for the Otis 2H well. From left to right, S-wave sonic, density (RHOB) and S-impedance (Zs) logs, the 20° incidence-angle synthetic seismogram (blue traces), the real trace extracted from the well location (red traces), and an inline going through the well with the synthetic inserted at the well location. The yellow lines indicate the correlation window. . . . .	85
3.10	20° PS wedge model generated using the PS extracted wavelet. The Lower Marcellus (golden color wedge) thickness is varied from 0 (right) to 500 ft (left). The OTIS 2H S-wave log is inserted at the real Lower Marcellus thickness (130 ft). The thin Stafford limestone (62 ft thick) causes a 90° phase-shift in the resulting waveform. At 130 ft thick, we are above one-half of the dominant period of the wavelet (peak-to-through time), which corresponds to Widess vertical-resolution limit. . . . .	87
3.11	Comparison between the PS1 data in PS time and the PP data in PP time. Major faults are more evident in the PS section, however, some smaller faults that are visible in the PP section are not observable on the PS data. . . . .	88
3.12	Comparison between the PS1 data in PP time and the PP data in PP time. Dotted horizons in the PS1 data correspond to the horizons interpreted in the PP volume. . . . .	88
3.13	Comparison between the Upper Marcellus PP (a) and PS (b) time-structure maps and the Onondaga PP (c) and PS (d) time-structure maps. The main east-west structural trends interpreted in the PP data tend to agree with the converted-wave interpretation. The PS time-structure maps show higher detail than the PP time-structure maps. . . . .	90
3.14	Comparison between the Upper Marcellus PP (a) and PS (b) isochrons and the Lower Marcellus PP (c) and PS (d) isochrons. The east-west valley features (downthrown side of the faults) show the highest time-thickness. . . . .	91

3.15	Interval $V_p/V_s$ maps for the Upper (a) and Lower Marcellus (b). These maps were generated for both units using the previously calculated isochrons by taking their ratio from the same interpreted horizons. The thicker east-west Valley features also exhibit the highest interval $V_p/V_s$ values. . . . .	92
4.1	PP-PS joint inversion workflow. Modified from the Hampson-Russel PROMC manual. . . . .	96
4.2	Comparison between the $V_p/V_s$ calculated from the dipole sonic log (blue), from the well-to-seismic tie (red) and the zero-offset VSP (black) at the OTIS 2H well. The $V_p/V_s$ from the well-to-seismic tie is in agreement with the $V_p/V_s$ from the VSP and shows slightly lower values than the $V_p/V_s$ calculated from the well-logs (8.5% for the Hamilton shale and 6.45% for the Marcellus interval). . . . .	98
4.3	Comparison between the PP (green) and PS (blue) frequency spectra. Note that both PP and PS bandwidths are very similar. . . . .	99
4.4	3D view showing the comparison between the PP (left) and PS (right) volumes after the registration. Both volumes are in PP time domain. Red arrows indicate the location of the Tully, Upper Marcellus, and Onondaga events. Note the good correlation between the two volumes, which is indicative of a correct registration. . . . .	101
4.5	Comparison between frequency spectra from the PP seismic data in PP time (blue) and the PS seismic data converted to PP time (green). Note the increase in both bandwidth and peak frequency of the PS data when converted to PP time. . . . .	102
4.6	NW-SE sections of (a) P-impedance ( $Z_p$ ) and (b) S-impedance ( $Z_s$ ) low-frequency models going through the OTIS 2H well location. . . .	104
4.7	NW-SE sections of (a) density and (b) $V_p/V_s$ low-frequency models going through the OTIS 2H well location. . . . .	105
4.8	Cross-plots between the natural logarithm of P-impedance ( $\ln(Z_p)$ ) and S-impedance ( $\ln(Z_s)$ ) (a) and between the natural logarithm of P-impedance ( $\ln(Z_p)$ ) and density ( $\ln(\rho)$ ), colored by interval. The linear-regressions for both plots are the background models for the inversion. The coefficients for each regression are seen in Table 4.1 .	106

4.9	PP-PS post-stack joint-inversion results at the OTIS 2H well location. Black, blue, and red logs correspond to the initial models, the filtered logs (0-0-40-50 Hz), and the inverted result, respectively. The yellow polygon denotes the Marcellus interval. There is a very good correlation between the inversion results and the original logs. . . . .	108
4.10	Comparison between the PP (left) and PS (right) synthetic traces generated in the inversion and the original traces at the OTIS 2H. The difference between the synthetics and the original traces corresponds to the error. . . . .	109
4.11	Difference between the PP seismic and the PP synthetic at an inline going through the well location. Note that the amplitude of the traces is almost zero, which means that the real seismic and the synthetic seismogram are almost identical. . . . .	110
4.12	NE-SW line going through the OTIS 2H well and showing the P-impedance (a) and S-impedance (b) inverted results. The displayed logs are the P-impedance (a) and S-impedance (b) logs upscaled to the seismic frequency. . . . .	111
4.13	NE-SW line going through the OTIS 2H well and showing the density (a) and Vp/Vs (b) inverted results. The displayed logs are the density (a) and Vp/Vs (b) logs upscaled to the seismic frequency. . . . .	112
4.14	Arbitrary inverted-density volume line going through the three wells located inside the seismic survey: LILLIE 2H, BRINK 2H, and OTIS 2H. The density logs upscaled to the frequency of the seismic are displayed at each well location. The inverted-density volume shows the same general trend as the LILLIE 2H and BRINK 2H density logs, which were not included in the inversion. . . . .	114
4.15	Cross-plots showing the cross-correlation coefficients between the original density logs and inverted-density values at the LILLIE 2H and BRINK 2H wells. . . . .	115
4.16	PP (a) and PS (b) statistical zero-phase extracted wavelets for 5-13° (blue), 13-21° (green), 21-29° (yellow), and 29-27° (magenta) and their corresponding amplitude spectra. Note that the PS angle-gathers have higher bandwidth and peak-frequency than the PP angle-gathers. . .	117

4.17	PP (a) and PS (b) angle-gathers well-to-seismic ties in their native times. Figures show the impedance logs, the zero-offset (20° in the case of the PS data) synthetic seismograms (blue), the extracted traces from the 5-13° angle-stack, and the real angle-stacks. There is a very good correlation for both PP and PS well-to-seismic ties (0.74 for the PP and 0.86 for the PS) . . . . .	118
4.18	Comparison between the PP pre-stack simultaneous inversion (a) and the PP-PS pre-stack joint inversion (b) results at the OTIS 2H well location. Note that by incorporating the shear-wave information the inversion error decreases substantially for all the inversion products. . . . .	119
4.19	Upper Marcellus (a) and Lower Marcellus (b) density maps showing the mean-density values over both intervals. The Upper Marcellus shows higher-density values than the Lower Marcellus, mainly due to the difference in kerogen content and possibly porosity between the two intervals. The three known gas-producing wells fall within density values lower than, approximately, 2.51 g/cc in the Lower Marcellus interval. . . . .	121
4.20	Density vs. P-impedance (a) and density vs. $V_p/V_s$ (b) cross-plots showing the inverted data overlaid by the upscaled logs (squares). Both well-logs and inverted data are colored by interval. Note that after upscaling the logs, the "Hot" Lower Marcellus (black squares) cannot be discriminated from the rest of the Lower Marcellus interval in the density vs. $V_p/V_s$ space. . . . .	123
4.21	Density vs. P-impedance cross-plot highlighting the high-TOC "Hot" Lower Marcellus interval (a) and the OTIS 2H log-plot showing the backtrack of the highlighted interval in red (b). . . . .	125
4.22	Vertical (a) and areal (b) distribution of the high-TOC "Hot" Lower Marcellus interval. The upscaled density log is plotted at the OTIS 2H well location and the map is extracted at 8 ms above the reservoir base. . . . .	126
4.23	Comparison between the mean density (a), $E\rho$ (b) and P-impedance (c) values over the Lower Marcellus Formation. Dotted polygons indicates the main low-density trend. Blue arrows indicate low-density zones that exhibit high P-impedance and high $E\rho$ values. This may indicate a change in mineralogy or increase in brittleness. . . . .	127

4.24	Density vs. $E\rho$ cross-plot highlighting the following: low-density and low- $E\rho$ (densities and $E\rho$ values lower than 2.5 g/cc 67 GPa $\times$ g/cc, respectively) the red polygon, slightly higher densities and low $E\rho$ (densities between 2.5 and 2.52 g/cc, and $E\rho$ values lower than 67 GPa $\times$ g/cc) the orange polygon, low-density values and higher $E\rho$ values (densities lower than 2.5 g/cc and $E\rho$ values higher than 67 GPa $\times$ g/cc) the cyan polygon, and higher densities and higher $E\rho$ values (densities between 2.5 and 2.52 g/cc and $E\rho$ values higher than 67 GPa $\times$ g/cc) the blue polygon. . . . .	129
4.25	Vertical (a) and areal (b) distribution of the polygons highlighted in Figure 4.24. The upscaled density log is plotted at the OTIS 2H well location and the map is extracted at 7 ms above the reservoir base. . . . .	130
A.1	P-wave pre-stack offset gathers overlaid by the incident angle. The target interval is enclosed in the red polygon. The maximum recovery angle for an offset of 14,700 ft (maximum offset) is higher than 45° for the target depth. Angles higher than 45°. . . . .	138
A.2	$F - k$ spectrum plot of the PP data. Coherent low-frequency linear noise is identified in the dipping event (a), while reflection signal is situated around the frequency axes (b). . . . .	138
A.3	Comparison between the migrated P-wave pre-stack gathers near the OTIS 2H well location before (left panel) and after the 3-8-50-80 Hz bandpass filter (middle panel), and the residual (right panel), that is, the original P-wave gathers minus the filtered P-wave gathers. . . . .	139
A.4	Comparison between amplitudes of primaries after multiple suppression using the $f - k$ (green) and the parabolic-Radon (red) methods. The blue line shows the exact AVO of the primaries (From Ross, 1999). . . . .	140
A.5	Graphic explanation of the modeled primaries (blue) and multiples (red) in the parabolic-Radon filter (Modified from Hampson-Russell AVO workshop tutorial, 2015). . . . .	141
A.6	Comparison between the filtered migrated P-wave pre-stack gathers near the OTIS 2H well (left panel), after the parabolic-Radon transform for random noise attenuation using a window between -20 and 100 ms (middle panel), and the residual (right panel). . . . .	142

A.7	Comparison between the migrated P-wave pre-stack gathers near the OTIS 2H well before the parabolic-Radon transform for multiple attenuation (left panel), after the application of the transform (middle panel), and the residual (right panel). The parabolas are modeled between -100 and 100 ms. . . . .	143
A.8	Comparison between the migrated P-wave pre-stack gathers near the OTIS 2H well before the bandpass filter (left panel), after the bandpass filter (middle panel), and the residual (right panel). . . . .	143
A.9	Comparison between the migrated P-wave pre-stack gathers near the OTIS 2H well before (left panel) and after trim statics are applied (right panel). The red polygon encloses the target interval. Note that the shifts are applied mostly to the far-offset traces. . . . .	144
A.10	Comparison between the original migrated P-wave pre-stack gathers near the OTIS 2H well (left panel) and the gathers after the application of the conditioning workflow (right panel). Note how the high-frequency noise, multiples and ground-roll has been effectively removed. . . . .	145
A.11	Comparison between the synthetic PP AVO response (red) and the real gathers AVO response before (blue) and after (yellow) multiple attenuation using the Radon transform. . . . .	146
B.1	PS migrated pre-stack gathers near the OTIS 2H well overlaid by the P-wave incidence angle. The red polygon encloses the target area, where the maximum P-wave incidence angle is, approximately, 38°. . . . .	148
B.2	$f - k$ spectrum plot of the PS data. PS data show less random and coherent noise than the PP data. . . . .	149
B.3	Comparison between the migrated PS pre-stack gathers near the OTIS 2H well location before (left panel) and after the 3-8-50-80 Hz band-pass filter (middle panel), and the residual (right panel), that is, the original PS gathers minus the filtered PS gathers. . . . .	149
B.4	Comparison between the filtered migrated PS pre-stack gathers near the OTIS 2H well (left panel), after the parabolic-Radon transform for random noise attenuation using a window between -20 and 30 ms (middle panel), and the residual (right panel). . . . .	150

B.5	Comparison between the migrated PS pre-stack gathers near the OTIS 2H well before the bandpass filter (left panel), after the bandpass filter (middle panel), and the residual (right panel). . . . .	150
B.6	Comparison between the original migrated PS pre-stack gathers near the OTIS 2H well (left panel) and the gathers after the application of the conditioning workflow (right panel). Note how the high-frequency noise has been effectively removed. . . . .	151
B.7	Comparison between the synthetic PS AVO response (red) and the real gathers AVO response after the conditioning process (blue). . . .	152
B.8	Comparison between the PP (a) and PS (b) amplitude spectra after conditioning. Their bandwidths are very similar, however the PS data shows higher amplitudes at high frequencies. . . . .	153

# List of Tables

1.1	Inventory of existing logs in the available wells. The OTIS 2H well is located inside the seismic survey, along with LILLIE 2H and BRINK 2H, however this two do not reach the reservoir interval. EICK 1H, THOMAS 1H and WEISBROD 4H are located outside the seismic survey. . . . .	16
2.1	Mean $V_p$ , $V_s$ , density, P-impedance (AI), and S-impedance (SI) values for the upper part of the Lower Marcellus (low TOC) and the "Hot" Lower Marcellus. These values are calculated from the OTIS 2H well logs. The fourth column indicates the percentage of change of each property and the arrows indicate whether the value increased or decreased. . . . .	54
2.2	Coefficients for the fitting of the Aki-Richards AVO approximation of the Zoeppritz equation for the AVA curves seen in Figure 2.20. Coefficients A, B and, C correspond to the intercept, gradient and curvature, respectively. . . . .	57
2.3	Elastic moduli and densities used in the model. . . . .	64
3.1	Parameters for the PP full-wavelet extraction at the OTIS 2H well. . . . .	73
3.2	Parameters for the PS statistical wavelet extraction at the OTIS 2H well. . . . .	83
4.1	Background linear trend coefficients used in the PP-PS post stack joint inversion: $\ln(Z_s) = 0.910905 \ln(Z_p) + 0.434333 + \Delta \ln(Z_s)$ and $\ln(Z_p) = 0.189866(Z_p) + -1.0132 + \Delta \ln(\rho)$ . . . . .	107

4.2	Comparison between the PP simultaneous inversion (PP only) and the PP-PS joint inversion (PP-PS joint) RMS errors for P-impedance, S-impedance, and density estimations at the OTIS 2H well location. The last row shows the percent difference between the errors of both inversion methods for each parameter. . . . .	120
A.1	Aki-Richards three-term AVO approximation coefficients for the AVO curves shown in Figure A.11. Coefficients A, B and C correspond to the intercept, gradient and curvature, respectively. The gradient changes from negative to positive after attenuating the multiples, matching the negative gradient of the modeled AVO response. The modeled AVO curvature is negative, while the real gathers AVO curvature is positive before and after multiples attenuation. . . . .	146

# Chapter 1

## Introduction

In the last decade, unconventional reservoirs have revolutionized the oil and gas industry, transforming the US in one of the world's biggest oil and gas producers, reaching a peak production of 79.13 bcf/d of natural dry gas and 9,604 Mbbl/d of crude oil in 2015 (EIA, 2015). These reservoirs are distinguished from conventional plays in the fact that their permeabilities are very low (in the order of nano-Darcys) (Smith et al., 2009), so they need to be artificially stimulated to produce hydrocarbons at economic rates.

### 1.1 Marcellus Shale

Among the different gas and oil shales in the US, Marcellus Shale is the largest gas producer (Figure 1.1), accounting for almost 40 % of the entire U.S. shale gas

production (74.24 bcf/d in January 2016).

Marcellus Shale is a Middle Devonian marine black shale deposited in the Appalachian Foreland Basin in the eastern United States. The Interior Marcellus Shale Assessment Unit is widely distributed across New York, Pennsylvania, and West Virginia, where the shale thickness is greater or equal to 50 ft (Figure 1.2). In the study area, located in Bradford County, Pennsylvania (Figure 1.3), the Marcellus interval lies at depths between 5600 and 6200 ft, and its thickness varies between 150 and 400 ft.

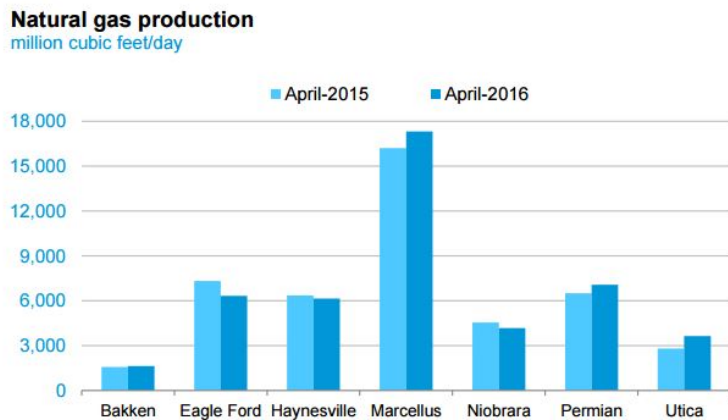


Figure 1.1: Comparison between natural gas production of different shale gas plays in the U.S from April 2015 to April 2016 (EIA Drilling Productivity Report, March 2016).

The Marcellus Shale is situated at the base of the Hamilton Group and is divided into three members, consisting of two organic-rich members (Upper Marcellus and Lower Marcellus) separated by the thin Cherry Valley limestone. The interval of interest is shown on a seismic section (Figure 1.4) to be discussed in detail later.

Natural gas present in the low-porosity Marcellus interval is typically trapped between grains and in natural fractures already present in the shale (Enomoto et al., 2011). In the study area, the Marcellus interval is bounded by two limestones: the Stafford limestone above and the Onondaga limestone below.

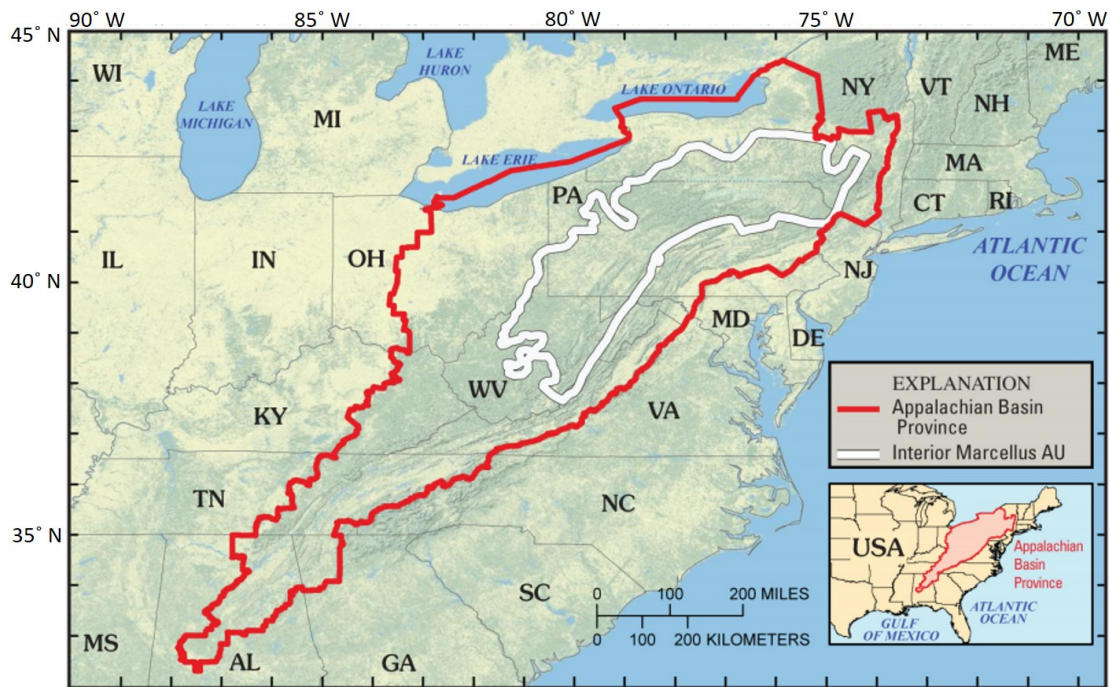


Figure 1.2: Map showing the boundary of the Interior Marcellus Assessment Unit (AU) in the Appalachian Basin Province. The Interior Marcellus AU is generally defined by shale thickness greater than or equal to 50 ft (U.S. Geological Survey Assessment of the Middle Devonian Marcellus Shale of the Appalachian Basin Province, 2011).

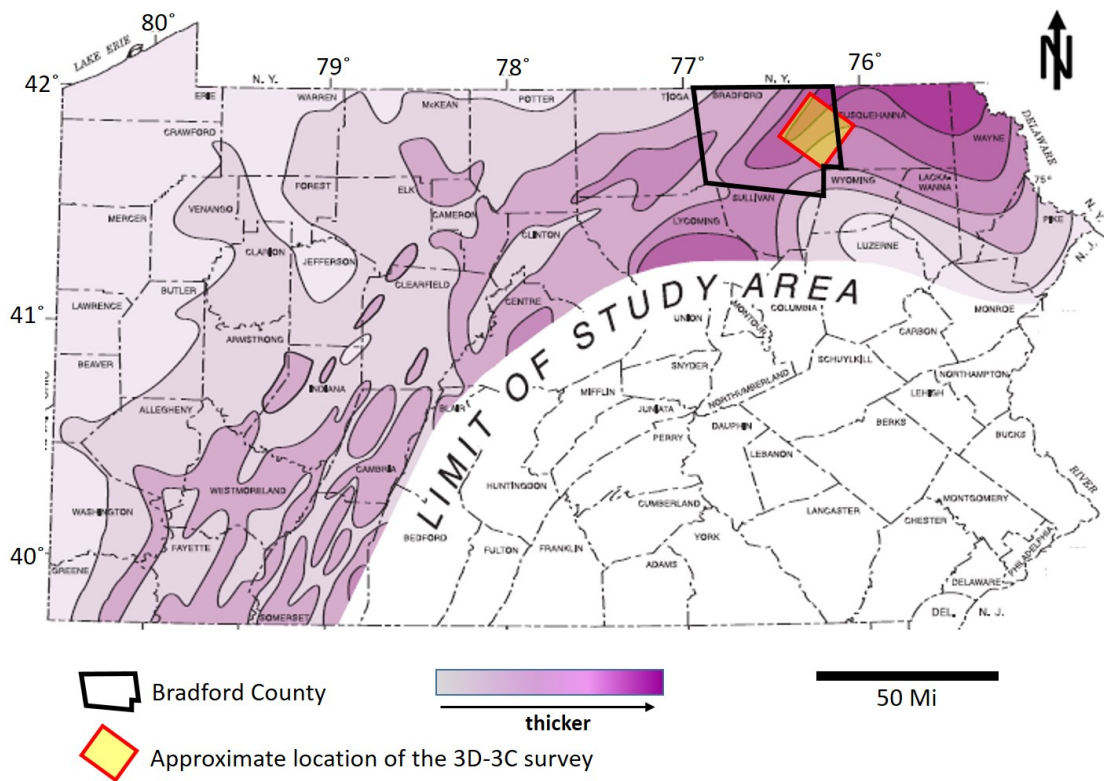


Figure 1.3: Map of Marcellus Shale thickness in Pennsylvania. Bradford County is outlined in black and the approximate location of the 3D-3C survey is outlined in red (Modified from Piotrowski and Harper, 1979).

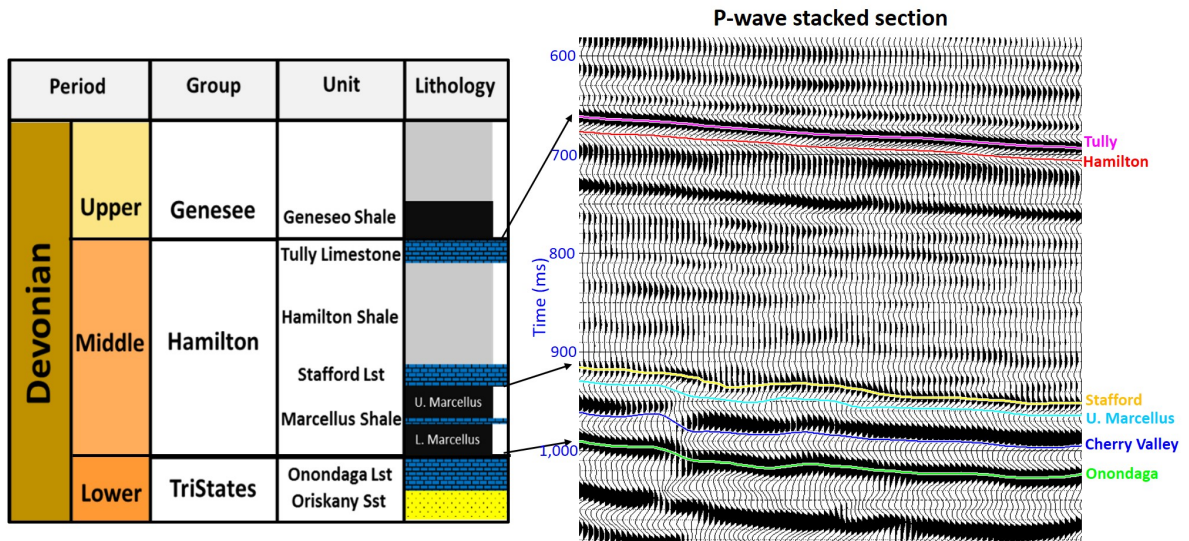


Figure 1.4: Stratigraphic chart and a section of the P-wave stacked seismic data showing the seismic expression of the Middle Devonian units, specifically the top and base of the Tully limestone and the Marcellus interval (Upper Marcellus and Lower Marcellus).

Wang (2012) studied the Marcellus Shale lithofacies distribution in West Virginia and Pennsylvania. He found that Marcellus Shale mineralogy varies both vertically and laterally throughout the formation, where the most abundant minerals are quartz and illite, with an average content of over 35% and 25%, respectively (Figure 1.5). Chlorite, pyrite, calcite, dolomite, and plagioclase are next in abundance, followed by K-feldspar, kaolinite, mixed-layer illite-smectite and apatite. Regarding TOC content, he found a median value of about 5 wt. %, and characterized organic-rich facies by those whose TOC is higher than 6.5 wt. %. The highest TOC value can reach up to 20 wt. %.

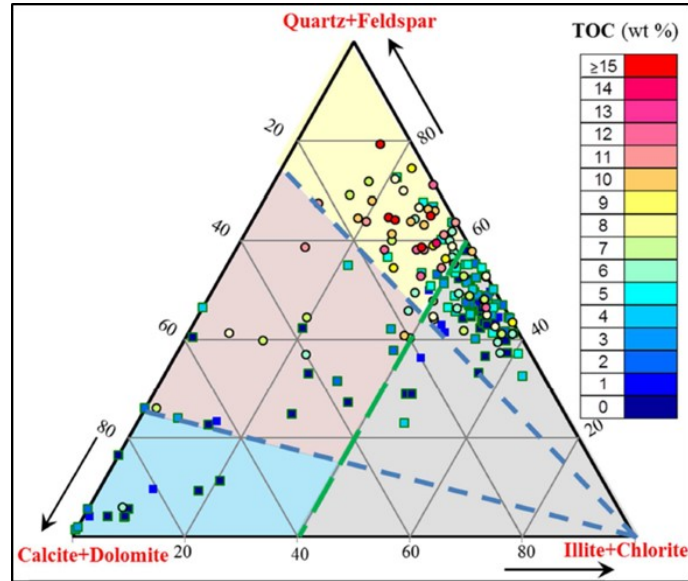


Figure 1.5: Ternary plot showing the characteristics of the mineral composition and organic matter richness and the classification method of Marcellus Shale lithofacies based on core data. The organic-rich facies are characterized by TOC values higher than 6.5% wt, indicated by the warmer colors (From Wang, 2012).

Besides mineral and TOC content, natural fractures also play a major role in the production of unconventional reservoirs. Gas production in Marcellus Shale is enhanced by the presence of two regional joint sets, J1 and J2, (Figure 1.6) since successful horizontal drilling may depend on the presence of systematic fractures (Engelder et al., 2009). These joints formed in the black shale units as the result of hydraulic fractures induced by abnormal fluid pressures during thermal maturation of organic matter.

The J1 joints are closely spaced (Figure 1.7), striking to the east-northeast, and are almost parallel to the maximum compressive normal stress of the contemporary tectonic stress field ( $S_{Hmax}$ ) (Engelder et al., 2009). These joints are crosscut by the later northwest-striking J2 joints set (see Figure 1.7), which are more pervasive

but less closely spaced.

Engelder et al., (2009) state that horizontal drilling and hydraulic fracturing benefit from these joint sets. By drilling in the north-northwest-south-south-east directions, horizontal wells cross and drain the J1 sets, while later hydraulic stimulation run east-north-east (parallel to J1) under the influence of the contemporary stress field, crosscutting and draining J2 sets.

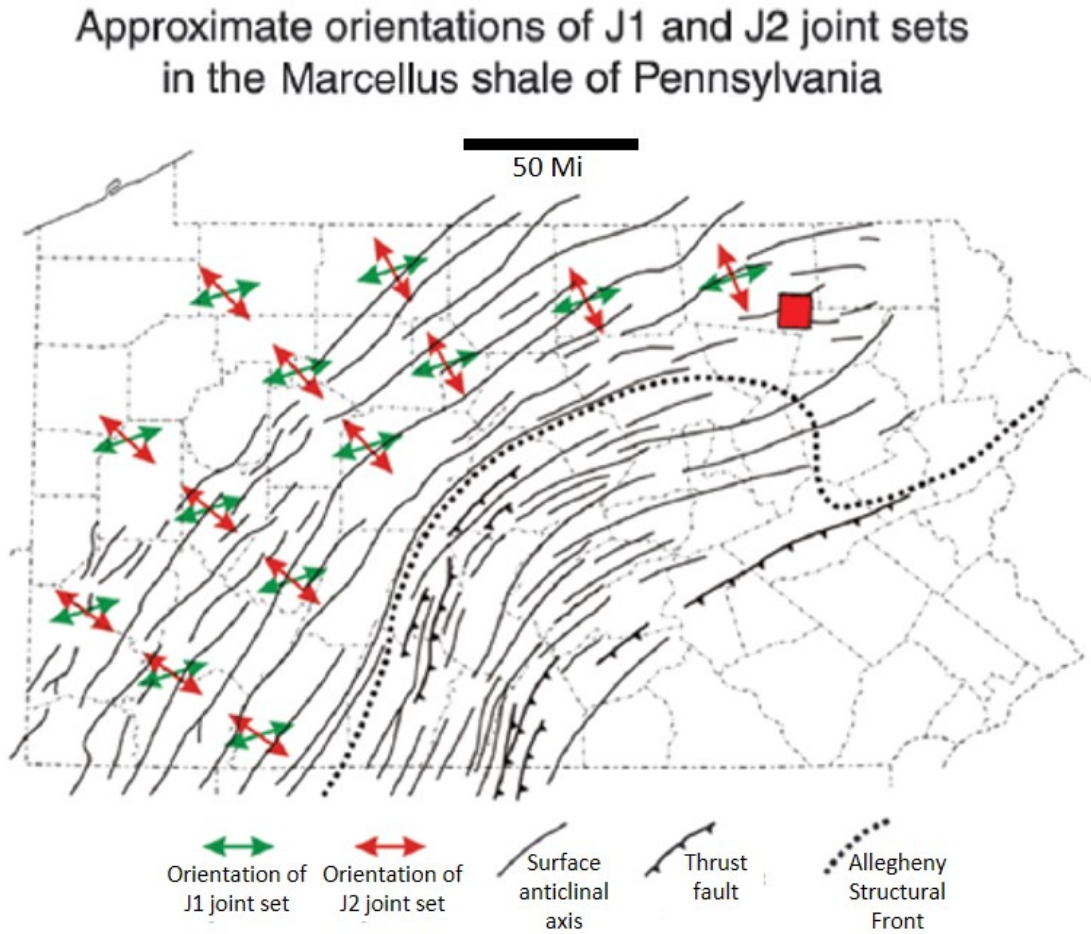


Figure 1.6: Regional distribution of the J1 and J2 joint sets in Pennsylvania. The red box shows the approximate study area (modified from Smith and Leone, 2010).

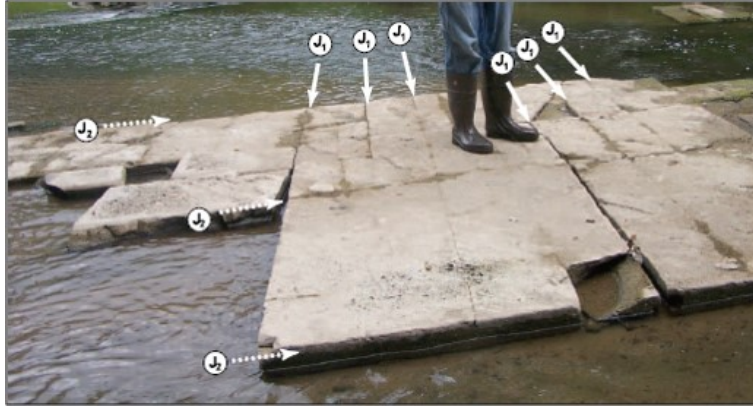


Figure 1.7: Crosscutting J1 and J2 joints in the Marcellus black shale exposed in Oatka Creek, Le Roy, New York. View is to the eastnortheast (From Engelder et al., 2009).

## 1.2 Motivation

Shales are a very complicated subject of study due to their highly variable mineralogy, friability, and anisotropic characteristics. Additionally, hydrocarbon production is not only determined by kerogen content but is highly dependent on the natural fractures framework, the distribution of quartz and/or carbonate within the reservoir, and the completion technique. Not all shales are alike, so it is necessary to understand the mechanical and lithological properties of the specific reservoir rock to correctly assess the target. Even though the Marcellus Shale has been subject of intense investigation, unconventional reservoirs technology, in general, is still subject of study, and geophysicists are continuously looking for seismic attributes and specific-rock properties that help locate the best areas to produce hydrocarbons.

## 1.3 Objectives

This study aims to investigate the rock properties of the Marcellus Shale through rock-physics analysis and seismic modeling to link the variation of key petrophysical parameters (e.g., kerogen, porosity, clay content) to variations in the elastic response (P- and S-wave velocities and density). The seismic sensitivity to variations in this parameters will aid in the characterization of the Marcellus Shale reservoir from surface seismic, which comprises the second part of this study.

The main problem to be assessed is the relation between rock properties and elastic parameters in the Marcellus Shale. This includes questions as:

- How are density and velocities affected by kerogen and clay content?
- How does the variation in clay and kerogen content affect the PP and PS seismic character?
- Is the seismic sensitive to small variations in kerogen content?
- Do "sweet spots" have a characteristic seismic signature in the study area?

## 1.4 Available data

### 1.4.1 Seismic data

The 3C-3D seismic data used in this study was acquired by Geokinetics and Geophysical Pursuit in 2009. The survey covers an area of, approximately, 9 mi<sup>2</sup> oriented

NE-SW, that is, parallel to the Appalachian Mountain range. The acquisition was done in conjunction with a larger P-wave survey. The acquisition parameters for the multicomponent survey are summarized in Figure 1.8.

The 3C-3D field data were processed by Geokinetics, and three migrated data sets were obtained: the reflected P-wave, and the two PS-modes, PS1 and PS2. To process the P-wave data, the vertical component is selected and the following processing workflow was used by Geokinetics:

1) First Arrival Picking Refraction Statics Calculations

Datum: 1,600 ft

Repl. Vel.: 14,000 ft/s

2) Spherical Divergence Correction

3) Surface Consistent Scaling and Surface Consistent Deconvolution

4) Velocity Analysis (1 mi analysis interval, 2 passes)

5) Residual Statics (2 passes)

6) Kirchhoff PSTM velocity analysis

7) Kirchhoff PSTM

8) Residual velocity analysis

Additionally, the following steps were applied to generate the stacked volumes:

9) Mute

- 10) Stack
- 11) TV Filter
- 12) TV Scaling

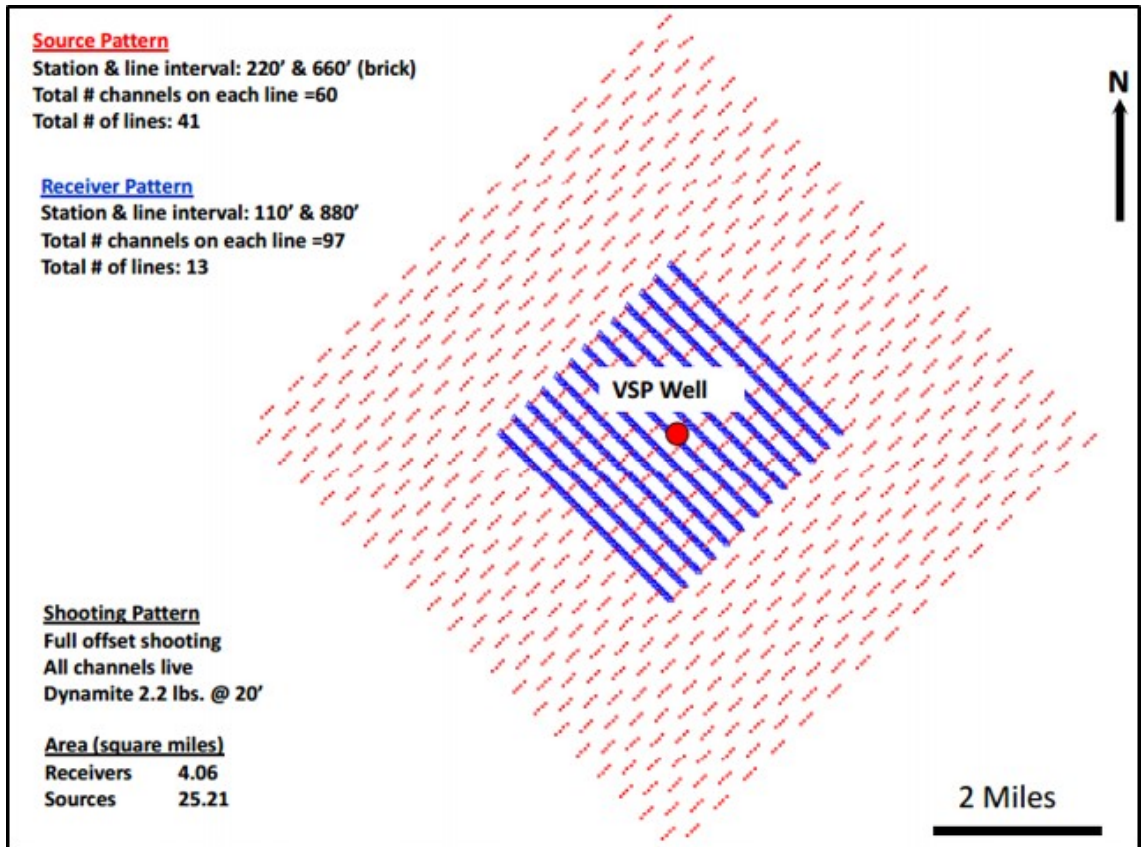


Figure 1.8: Base map showing the location of the VSP calibration well (OTIS 2H) relative to planned positions of source and receiver stations used for 3C-3D seismic survey (From Hardage et al., 2011).

The two PS-modes need to be separated before seismic processing. To separate PS1 and PS2, the azimuth of the principal anisotropy direction needs to be determined during data processing with common-receiver gather stacks, sectorized and sorted by azimuth (Chaveste et al., 2013). The azimuth of the fast PS-wave (PS1)

is determined to be N80E (assumed constant over the survey), and the horizontal components are again analytically rotated, this time in the directions of fast and slow polarizations (Chaveste et al., 2013). PS1 and PS2 data sets are then processed and migrated following a similar workflow than the P-wave, with the addition of a third residual shear statics pass.

The PP CDP and PS1 CCP pre-stack gathers are evidently affected by high-frequency noise (Figure 1.9). The PP CDP gathers show strong low-frequency and high-amplitude noise that appears to be ground roll or guided waves. Multiples are also present. This noise should be suppressed and gathers should be conditioned before attempting to do any quantitative analysis of these data. The gather conditioning process I applied is seen in Appendix A.

Figure 1.10 shows a comparison between the PP and PS1 full-stacked sections in their native times. The target interval (enclosed in the red polygon) is located at, approximately, 1,000 ms in the PP section (PP time) and 1,300 ms in the PS section (PS time). Both volumes show good data quality and continuity of events.

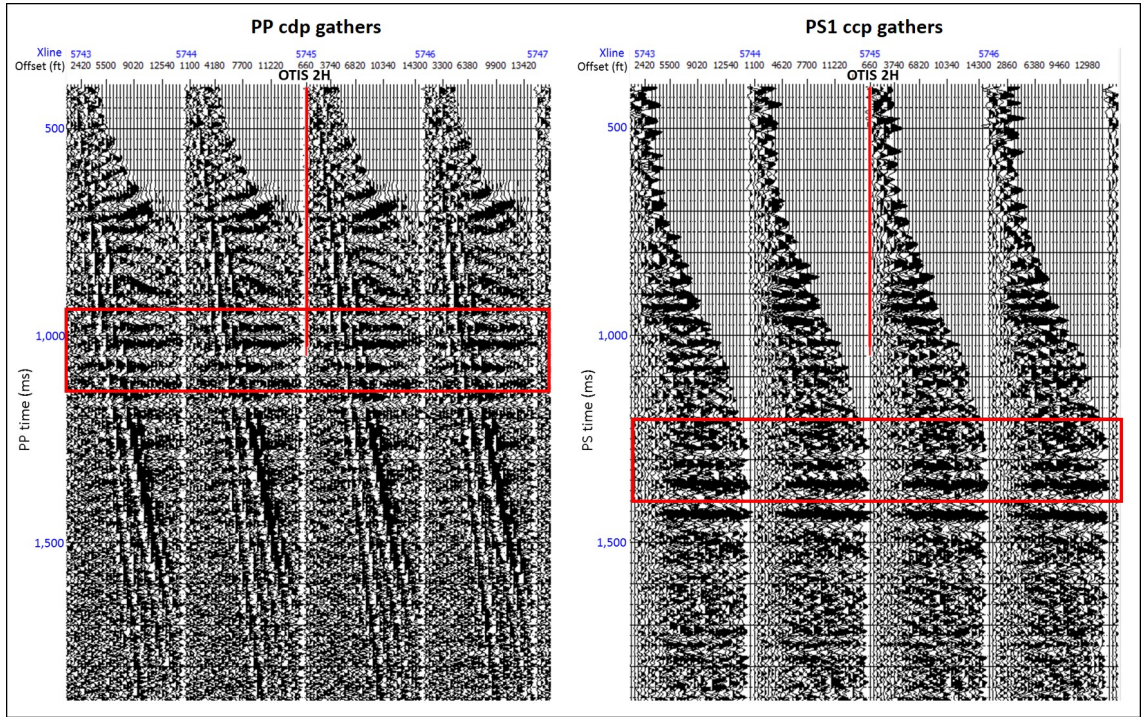


Figure 1.9: Comparison between the P-wave cdp gathers and the PS1 ccp gathers in their native times, at an inline going through the well OTIS 2H location (well path shown in red). Both volumes show high- and low-frequency noise as well as multiples that need to be attenuated.

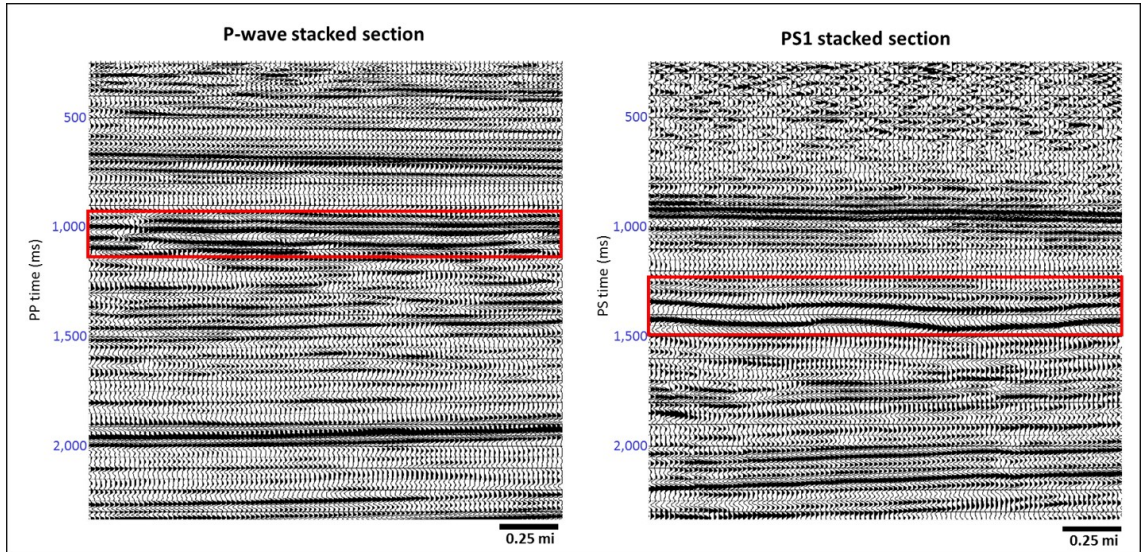


Figure 1.10: Comparison between the P-wave and PS1 stacked sections in their native times. The red polygon encloses the target interval: around 1,000 ms for the P-wave section and around 1,300 ms for the PS1 section.

## 1.4.2 Well-log data

The OTIS 2H well is a gas-producer well drilled in the middle of the 3C-3D survey (see Figure 1.8). Log data from the OTIS 2H well was provided by Chesapeake for this research. The suite of logs include spectral GR, caliper, density, dipole sonic, resistivity, neutron porosity, and photoelectric (PEF). VSP data was also acquired in this well for calibration, and the zero-offset VSP is also available

The Bradford County well-log database from the Pennsylvania Department of Conservation and Natural Resources was provided for this study. From this database, only three wells with measured dipole sonic were found. These are gas producer wells

located outside the seismic survey: THOMAS 1H, EICK 1H, and WEISBROD 4H (see Figure 1.11). Two of them (EICK 1H and THOMAS 1H) have petrophysical evaluation, with mineralogy and TOC calculated through pulse neutron spectroscopy (PNS). This data will be very helpful in the petrophysical analysis of the OTIS 2H well, serving as a way of calibrating results. Two other gas-producer wells located inside the seismic survey were found (LILLIE 2H and BRINK 2H). However, their logs do not reach the reservoir, and no sonic logs are available. Figure 1.11 shows the location of the available wells with respect to the seismic volume (outlined in red). The inventory of logs available for each well is shown in Table 1.1

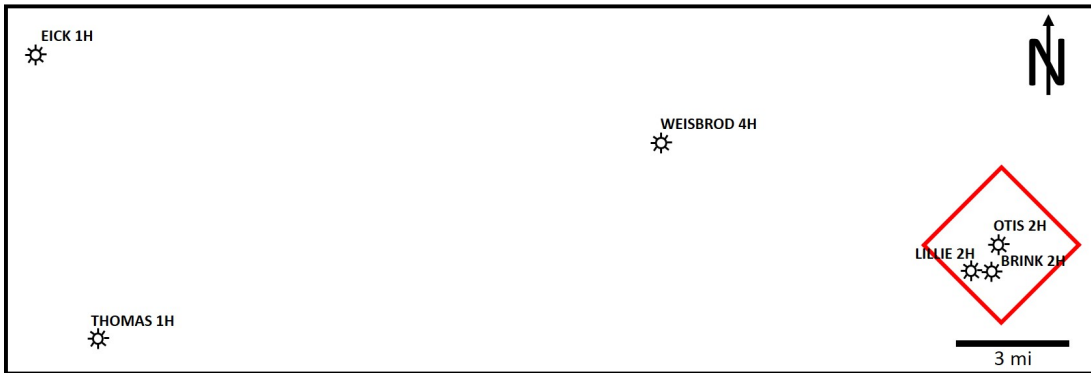


Figure 1.11: Base map showing the location of the available wells and the 3D-seismic volume (outlined in red).

### 1.4.3 Software

Petrel is used for the structural seismic interpretation and post-stack attributes calculation. The gather conditioning, seismic modeling, well-ties, and inversions are performed in Hampson-Russell. The well-log analysis and facies classification are carried out in RokDoc. Matlab is used for the rock-physics modeling.

LOGS	WEISBROD 4H	EICK 1H	THOMAS 1H	OTIS 2H	LILLIE 2H	BRINK 2H
GR	yes	yes	yes	yes	yes	yes
Spectral GR	yes	yes	yes	yes	no	no
Caliper	yes	yes	yes	yes	yes	yes
Dipole sonic	yes	yes	yes	yes	no	no
Density	yes	yes	yes	yes	yes	yes
Resistivity	yes	yes	yes	yes	yes	yes
PEF	yes	yes	yes	yes	no	no
Petrophysical evaluation	no	yes	yes	no	no	no
TOC from PNS	no	yes	no	no	no	no

Table 1.1: Inventory of existing logs in the available wells. The OTIS 2H well is located inside the seismic survey, along with LILLIE 2H and BRINK 2H, however this two do not reach the reservoir interval. EICK 1H, THOMAS 1H and WEISBROD 4H are located outside the seismic survey.

## Chapter 2

# Well-log analysis and petrophysical properties

Well-log analysis is crucial to understand the petrophysical properties of the reservoir and how they relate to the elastic parameters. The main objective of this chapter is to use the available log data to investigate the rock properties of the Marcellus Shale in the study area, describe its mineralogy, porosity, and kerogen content and try to understand the relationship between these parameters and the elastic response (i.e. velocity and density).

As mentioned in Chapter 1, four wells with measured dipole sonic are available for this study. The suite of logs include caliper, spectral gamma-ray, dipole sonic, density, neutron porosity, resistivity, and photoelectric factor (PEF). In addition to log data, two of these wells, EICK 1H and THOMAS 1H, contain petrophysical

evaluation from pulse neutron spectroscopy (PNS): mineral volumes, porosity, and TOC.

The thickness of the Marcellus Shale interval in the study area increases from west to east, towards the location of the seismic survey, where it reaches a maximum thickness of 310 ft in the OTIS 2H well (see Figure 2.1). Note that the Marcellus Shale interval can be easily recognized in total gamma-ray logs (highlighted by the red polygon in Figure 2.1). It shows an increase in radioactivity, which translates into API values higher than 150 API in this wells, compared to the inorganic Hamilton shale (highlighted by the brown polygon in Figure 2.1), with gamma-ray values lower than 100 API. Passey et al., (2010) state that the high gamma-ray values encountered in organic shales are related to the presence of radioactive materials, specifically uranium, contained in shales deposited under marine conditions (type II kerogen), like the Marcellus Shale. In this case, a strong correlation exists between TOC and uranium content, which can be exploited using K, Th, and U fractions from spectral-gamma logs. Boyce and Carr, (2010) found a relationship between uranium and density porosity in West Virginia and Southwestern Pennsylvania, and showed that the crossover between uranium and bulk density curves is indicative of areas with high TOC content and potential for both free and bound gas. Figure 2.1 shows a west-east cross-section of the four available wells. The first track shows the total gamma-ray curve and the second track shows the comparison between uranium and bulk density logs. The crossover between uranium and density is highlighted in red, where the cutoff values are taken from Boyce and Carr, (2010). The crossover indicates that the base of the Lower Marcellus has the highest potential for gas

saturation and high TOC content while the Upper Marcellus seems to decrease its potential from west to east, towards the location of the seismic survey.

The Marcellus Shale mineralogy varies both vertically and laterally throughout the formation, where the most abundant minerals are quartz and illite, with an average content of over 35 % and 25 %, respectively, followed by chlorite, pyrite, calcite, dolomite, and plagioclase (Wang, 2012). He found a median TOC value of about 5 wt. %, and characterized organic-rich facies by those whose TOC is higher than 6.5 wt. %, while the highest TOC value can reach up to 20 wt. %. Since mineralogy and porosity logs were only available for EICK 1H and THOMAS 1H, an approximate estimation of clay volume, TOC, and porosity should be performed for OTIS 2H, using the other two wells to calibrate the observations.

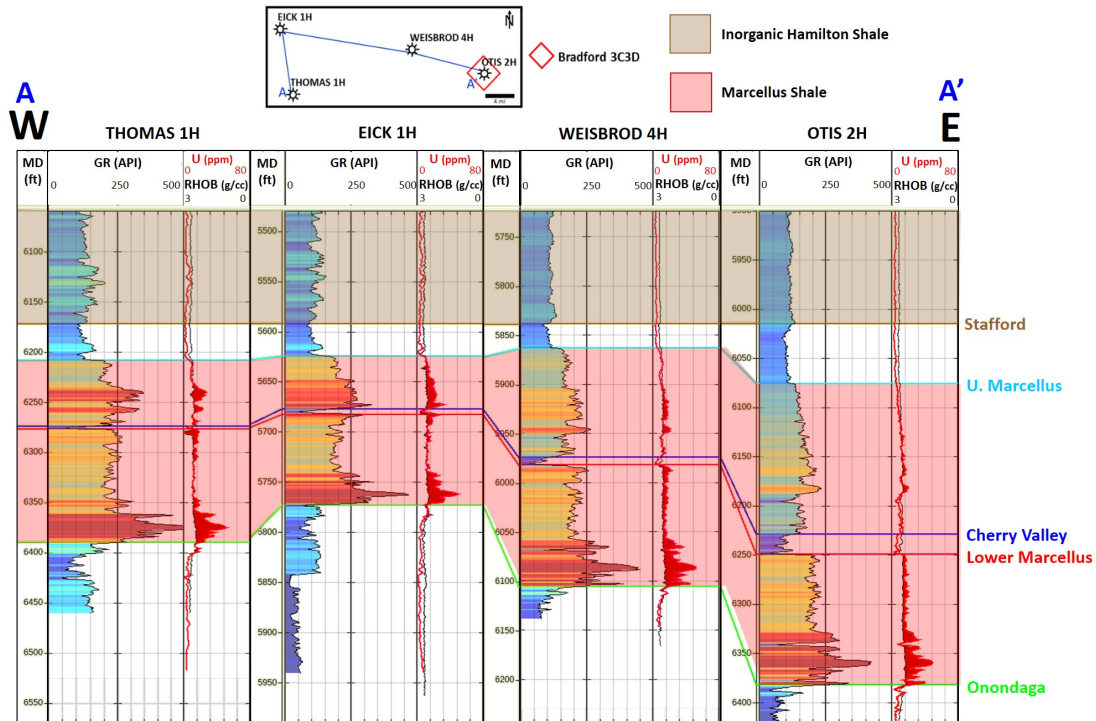


Figure 2.1: West-east cross-section going through the available wells (flattened at the Stafford top), showing the total gamma-ray log in the first track and the uranium (U) and density (RHOB) logs in the second track. The Marcellus Shale interval can be easily recognized in total gamma-ray logs (highlighted by the red polygon), showing an increase in radioactivity, which translates in API values higher than 150 API in this wells, compared to the inorganic Hamilton shale (highlighted by the brown polygon). Areas with high TOC and potential for gas accumulation are highlighted in red (U-RHOB crossover)

## 2.1 Clay volume estimation

Vclay is estimated in two ways in the OTIS 2H well, using the GR log corrected for uranium ( $GRC$ ), and using both density and neutron porosity logs. Since uranium is poorly soluble in the oxygen-poor, reducing conditions where source-rocks are generated, is commonly found concentrated in organic matter (Rowan et al., 2011). Hence, the total GR log should be corrected for uranium before estimating clay content to remove the effect of the organic matter (Crain et al., 2014):

$$GRC = GR - 8U \quad (2.1)$$

Where,  $GRC$  = corrected  $GR$ ,  $GR$  = total  $GR$ , and  $U$  = uranium in ppm.

The  $GRC$  is then used to estimate clay content in the following way:

$$Vclay_{GRC} = \frac{GRC - GRC_0}{GRC_{100} - GRC_0} \quad (2.2)$$

Where,  $Vclay_{GRC}$  = Vclay from  $GRC$ ,  $GRC$  = corrected GR,  $GRC_0$  = cutoff for 0 % clay,  $GRC_{100}$  = cutoff for 100 % clay.

The cutoffs for 0 and 100 % clay are calibrated using the THOMAS 1H and EICK 1H corrected GR logs and the clay volumes estimated from PNS. To calculate  $Vclay$  from density and neutron porosity, the following methodology was applied:

$$PHID = \frac{RHO_B - RHO_{ma}}{RHO_{fl} - RHO_{ma}} \quad (2.3)$$

Where,  $PHID$  = density porosity,  $RHOB$  = density log,  $RHO_{ma}$  = matrix density, and  $RHO_{fl}$  = pore-fluid density.

The matrix density is assumed to be 2.71 g/cc, based on average mineralogy from THOMAS 1H and EICK 1H. The effective pore-fluid density is taken as a constant 0.6 g/cc, calculated using Wood's equation assuming the rock is 70 % gas-saturated.

$$V_{clay_{PHI}} = \frac{DIFFND - PHID_{cl}}{NPHI_{cl} - PHID_{cl}} \quad (2.4)$$

Where,  $V_{clay_{PHI}} = V_{clay}$  from density logs,  $DIFFND$  = difference between neutron and density porosities,  $PHID_{cl}$  = density porosity at pure clay, and  $NPHI_{cl}$  = neutron porosity at pure clay. The density porosity and neutron porosity of pure clay are 0 and 0.4, respectively. The neutron porosity at pure clay is taken from literature (Asquith, 2014).

Figure 2.2 shows, from left to right, the total GR and the corrected GR (thick black curve), the uranium, potassium, and thorium content, neutron porosity and density, and the comparison between both clay volumes ( $V_{clay_{GRC}}$  and  $V_{clay_{PHI}}$ ) estimated for the OTIS 2H well. Note how the  $GRC$  log resembles the thorium log, showing a decrease at the base of the Lower Marcellus, which indicates a decrease in clay content, as showed in the  $NPHI - RHOB$  crossover. Both clay volumes are very similar, which is highlighted by cross-plotting the two curves in Figure 2.3, where the linear regression has a correlation coefficient of 0.83.

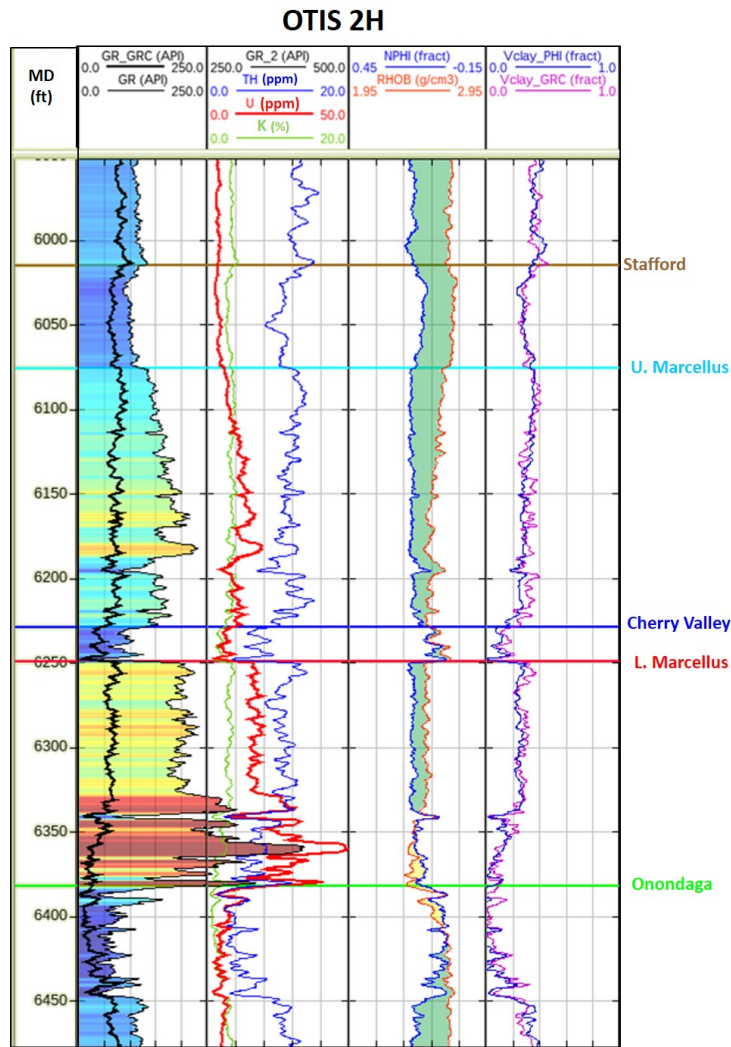


Figure 2.2: OTIS 2H well logs. From left to right, total GR and the corrected GR (thick black curve), uranium, potassium, and thorium content, neutron porosity and density, and the comparison between both clay volumes ( $V_{clay_{PHI}}$  and  $V_{clay_{GRC}}$ ) estimated for the OTIS 2H well. Clay volumes calculated with the two different methods show very similar results, and both follow the separation trend between NPHI and RHOB: the higher the separation, the higher the clay volume.

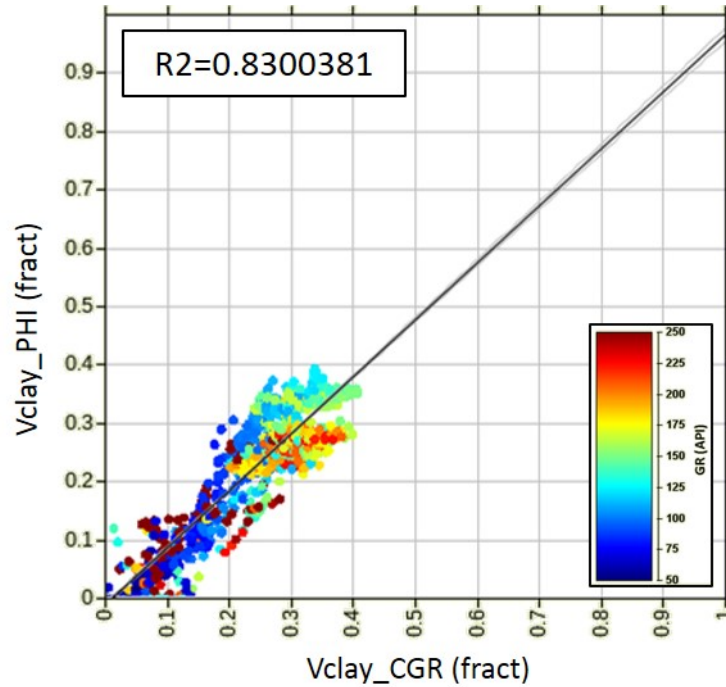


Figure 2.3: Cross-plot between the clay volumes calculated in the Upper and Lower Marcellus intervals at OTIS 2H using the porosity logs ( $V_{clay_{PHI}}$ ) and the corrected GR log ( $V_{clay_{CGR}}$ ), colored by GR. The linear regression has a correlation coefficient ( $R^2$ ) of 0.83, which indicates a very good agreement between both curves

Pyrite has a density of 4.93 g/cc and a PEF value of 18 b/e (Mavko et al., 2008), and according to Clavier et al., (1976) if found in great amounts it could affect sonic, neutron, and density logs. A cross-plot between PEF and density for all the wells (Figure 2.4) show low densities ( $< 2.75$  g/cc) and low-PEF values ( $< 8$  b/e), which correlates with the pyrite volume from the petrophysical evaluation of THOMAS 1H and EICK 1H ( $< 5\%$ ). In this sense, log data is not corrected for pyrite.

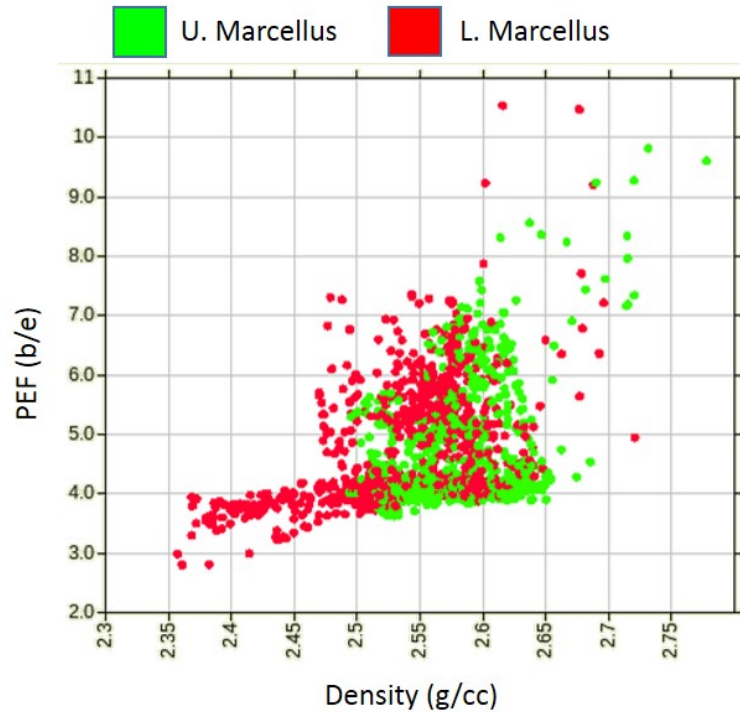


Figure 2.4: Cross-plot between density and PEF for the Upper and Lower Marcellus intervals. Both intervals show low densities ( $< 2.75$  g/cc) and low-PEF values ( $< 8$  b/e), indicating a marginal pyrite content

Since pyrite content seems to be minimal and not affecting the logs in a significant way, calcite and quartz are the other major inorganic constituents of the rock. The calcite volume ( $V_{cal}$ ) was estimated scaling the sonic log, using THOMAS 1H and EICK 1H for calibration, and assuming the calcite content in Onondaga and Cherry Valley limestones does not change dramatically. Then, the quartz volume ( $V_{qz}$ ) is calculated as:

$$V_{qz} = 1 - (V_{clay} + V_{cal}) \quad (2.5)$$

The final mineral volumes for OTIS 2H are shown at the end of the Chapter.

## 2.2 TOC estimation

Total organic carbon (TOC) is important in shale-gas reservoirs because total porosity and gas saturation are directly associated with the TOC content of the rock (Passey et al., 2010). Numerous geochemical and petrophysical techniques have been developed to characterize organic-rich rocks. The usual workflow includes the computation of TOC from logs which are then calibrated using TOC (in weight %) from pyrolysis of cutting core data (Alfred and Vernik, 2012). Unfortunately, core data is not available for this study, so the TOC estimation of the OTIS 2H well will be calibrated only with the TOC calculation from pulse-neutron spectroscopy (PNS) in EICK 1H. The PNS logging tools measure gamma-ray spectra at specific energy levels, can accurately determine the primary mineral concentration and other components like kerogen and barite in organic-rich shales (Wang and Carr, 2013). Moreover, Charsky, and Herron (2013) showed that this technique is more robust than conventional methods for TOC estimation (e.g., Passey, 1990; Schmoker, 1979).

Alkahtani and Tutuncu (2014) state that the density log can be the best method to estimate TOC while taking into consideration that (1) heavy minerals (e.g. pyrite)

are present as trace minerals (i.e. not in significant quantities), (2) there is no variation in porosity, fluid phases and lithology over an interval of interest, and (3) good borehole conditions because density logs are sensitive to the borehole rugosity (e.g. shale washout) (Passey et al., 1990; Sondergeld et al., 2010). From the various existing methods for TOC estimation, the Passey (1990) method seems to be the most popular. It employs an overlay of porosity logs (sonic, density or neutron) with a deep resistivity log, assuming that porosity logs respond to kerogen/matrix and fluids, while resistivity logs respond to fluids, and that the scaled difference ( $\Delta \log R$ ) between them is related to the TOC content through level of thermal maturation, LOM. In organic-rich rocks, the separation between resistivity and porosity logs results from the low velocity and low-density kerogen and the increased deep resistivity due to the generated hydrocarbons (Alfred and Vernik, 2012). TOC (in weight %) estimation using the density log is shown below:

$$\Delta \log R = \log_{10} \frac{RT}{RT_{baseline}} - ScalingFactor \times \frac{RHOB}{RHO_{baseline}} \quad (2.6)$$

Where,  $RT$  = deep resistivity log,  $RT_{baseline}$  = resistivity in the organic-lean zone,  $RHOB$  = density log, and  $RHO_{baseline}$  = density in the organic-lean zone.

$$TOC(wt\%) = \Delta \log R \times 10^{(2.297 - 0.168 \times LOM)} \quad (2.7)$$

Where,  $\Delta \log R$  = scaled difference between deep resistivity and density logs and  $LOM$  = level of organic maturity.

The level of organic maturity can be estimated from vitrinite reflectance data,

where the higher the vitrinite reflectance, the more thermally mature the formation and the higher the LOM (Passey, 1990). In thermally overmature formations, as the case of the Marcellus Shale, a value of 10.5 should be used (Charsky and Herron, 2013). Vernik and Landis (1996) also proposed an empirical formulation for TOC estimation using the density log:

$$TOC(wt\%) = 67 \times \frac{RHO_K(RHO_S - RHOB)}{RHOB(RHO_S - RHO_K)} \quad (2.8)$$

Where,  $RHOB$  = density log,  $RHO_S$  = clay density and  $RHO_K$  = kerogen density, assumed to be 1.42 g/cc from Yenugu and Vernik's (2015) work in the Marcellus Shale.

Both Passey and Vernik's formulations rely on the assumptions that matrix porosity remains invariant through zones in the organic shale. The density of the clay varies as a function of burial depth, and since the exact mineralogical composition is not known, the clay density is an adjustable parameter. The Marcellus Shale is known to be rich in illite. However, it also contains other clay minerals that can vary its elastic moduli. The Schlumberger Lith-2 plot uses the Th/K value to determine the type of clay minerals in a shale formation (Figure 2.5), where clays dominated by illite have Th/K between 2 and 3.5. The cross-plot shows that illite is the principal clay mineral in both Upper and Lower Marcellus. However, smectite-illite mixed clays are also present in the formation. Shales tend to be rich in smectite down to temperatures of about 70° C, when smectite transforms to illite, with microcrystalline quartz as a by-product (Avseth and Carcione, 2014). Smectite has lower density than illite (2.2

g/cc versus 2.9 g/cc). Hence the presence of smectite will significantly soften the rock (Carcione and Avseth, 2015).

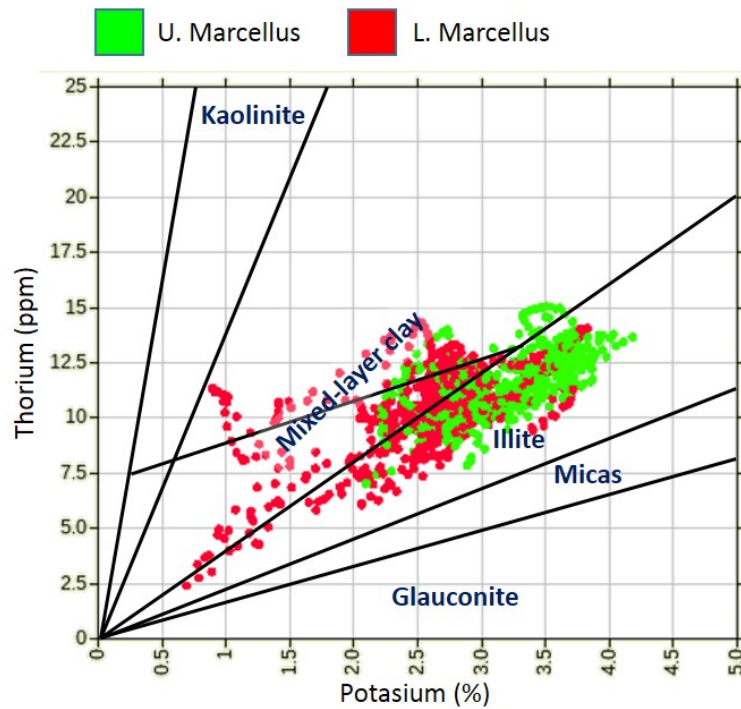


Figure 2.5: Cross-plot between potassium and thorium for clay classification in the Upper and Lower Marcellus intervals (green and red samples, respectively). The clay mineralogy in the Marcellus Shale seems to be dominated by illite, however there are also smectite-illite mixed clays

The EICK 1H well was used to obtain and calibrated clay density in Vernik and Landis (1996) empirical formula. A clay density of 2.71 g/cc is needed to get a relatively good match between the PNS-TOC and Verniks-TOC. Hence, a clay density of 2.71 g/cc is assumed for the OTIS 2H well.

As a third way of estimating TOC, a multi-variate regression is derived in the EICK 1H well to calculate the PNS-TOC curve through a multi-variable transform that includes the uranium, GR, density, and Poisson's ratio logs. The combination of logs that best estimate the TOC curve is found using the step-wise regression method (Hampson et al., 2001).

Figure 2.6 shows the comparison between the three calculated TOC curves and the PNS-TOC at the EICK 1H well and the TOC estimations at the OTIS 2H well. The inorganic Hamilton Shale was taken as the baseline for  $\Delta\log R$  calculation in Passeys formulation. The three estimations follow the PNS-TOC trend (black curve) very closely, especially in the high TOC zone at the base of Lower Marcellus, they tend to overestimate TOC values in very low TOC zones. Linear regressions (Figure 2.7) show that the highest correlation for the Marcellus interval is achieved by the multi-variate TOC estimation ( $R^2=0.55$ ). At the OTIS 2H well, the multi-variate TOC (green) shows slightly lower TOC values than the Passey (blue) and Vernik's TOC (magenta) at the Upper Marcellus interval. Note how the multi-variate TOC follows the uranium curve very closely. A relation between uranium, density and TOC content has been reported by several authors (Vernik et al., 2013; Passey et al., 2010; Milliken et al., 2013), where high uranium correlates to low densities and high TOC values. Such relationship can be depicted by cross-plotting uranium vs. density, colored by TOC content in the Marcellus interval for the EICK 1H well (see Figure 2.8).

Passeys TOC is influenced by resistivity spikes that seem to be noisy readings and shows lower values than the multi-variate and Vernik's TOC at the top of the

Lower Marcellus interval. The three curves are in excellent agreement at the base of the Lower Marcellus, showing TOC values higher than 6 wt. %.

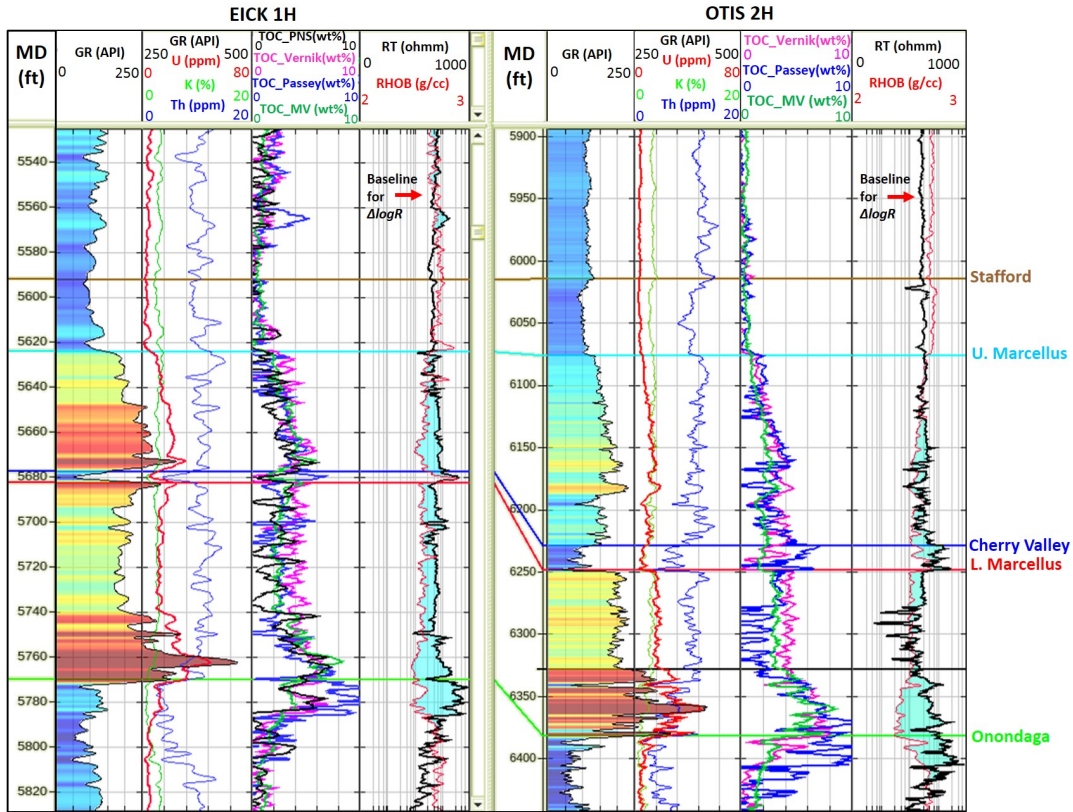


Figure 2.6: Comparison between the TOC estimations at the EICK 1H and OTIS 2H wells. From left to right, total gamma-ray (GR) and uranium-corrected gamma-ray (GRC), uranium (U), potassium (K), and thorium (Th), comparison between the TOC curves, and the resistivity (RT)-density (RHOB) overlay for  $\Delta \log R$  calculation, where areas highlighted in blue correspond to high organic-matter zones. Note the good agreement between the TOC curves, where high TOC values are associated with high GR, high U, high RT, and low RHOB.

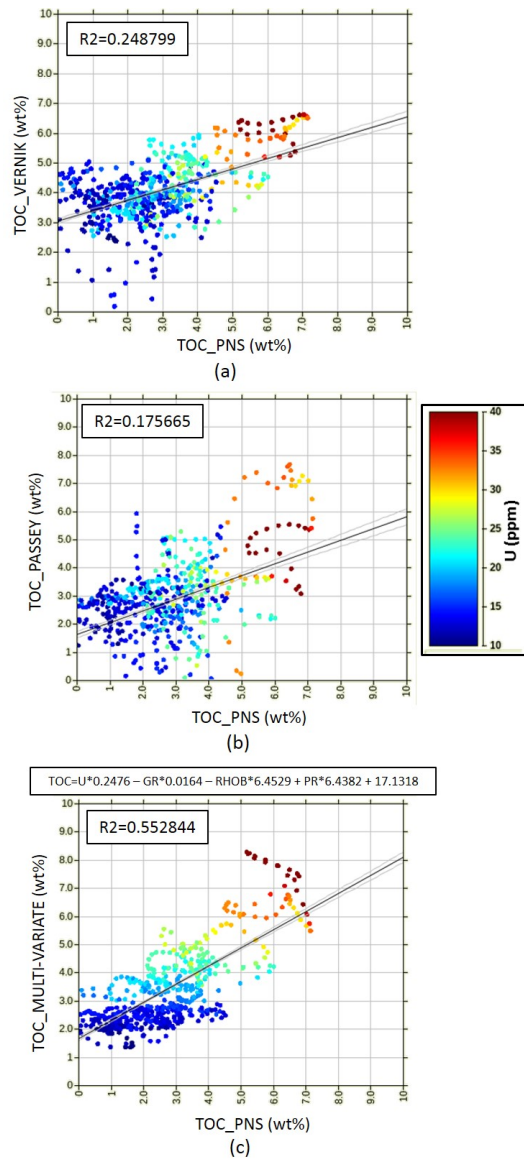


Figure 2.7: Correlation between TOC curves estimated by (a) Passey and PNS, (b) Vernik and PNS, and (c) multi-variate regression and PNS at the EICK 1H well. Samples are colored by uranium values. There highest correlation is found for the TOC curve estimated through multi-variate regression. However, they all show consistent estimations for the high TOC area (6 to 7 wt. %).

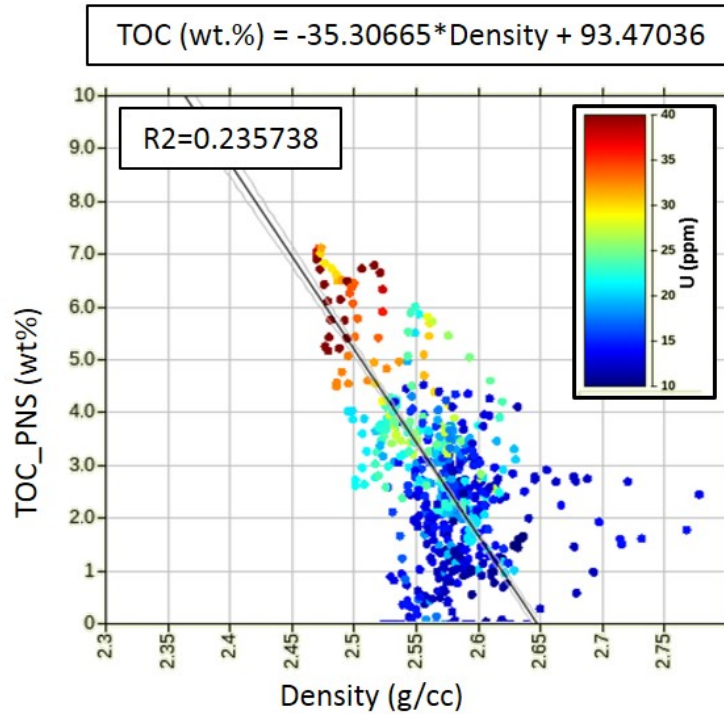


Figure 2.8: TOC vs. density cross-plot for EICK 1H (the well that has TOC calculated through PNS) in the Upper and Lower Marcellus intervals. Samples are colored by uranium values. Note the correlation between high uranium, low density, and high TOC content.

## 2.3 Total porosity estimation

A typical shale-gas rock is composed of a matrix made up of inorganic minerals and organic matter (kerogen), along with pore space between these components (Figure 2.29). Porosity is also generated in kerogen as a result of maturation and kerogen shrinkage (Prasad and Zargari, 2014). Loucks et al., (2012) defined three pore types

in organic-rich rocks based on vastly available SEM images from different shale samples. They defined: two types of pores associated with the minerals (interparticle and intraparticle mineral porosity,  $\phi_{mm}$ ) and the third type associated with the organic matter (organic porosity,  $\phi_{om}$ ). Burial and maturation of the source rock affect all types of pores, and clay minerals also undergo significant porosity reduction due to compaction (Kuila and Prasad, 2013). Unlike conventional reservoirs, shale reservoirs can produce both free gas and adsorbed gas present in kerogen porosity, where the water saturation is zero (Asquith, 2014).

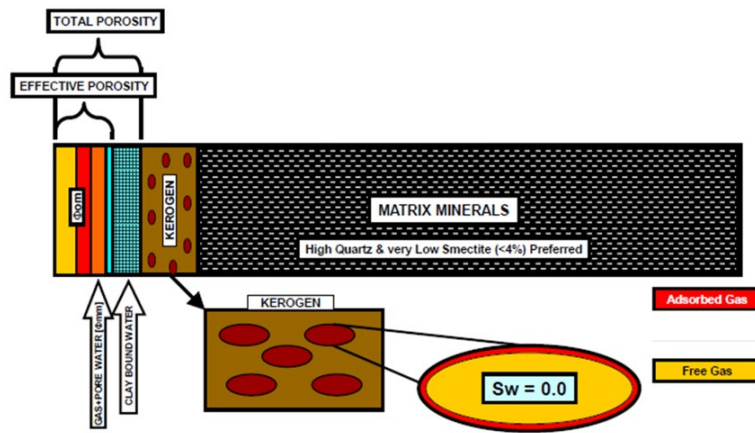


Figure 2.9: Schematic of a clay-rich organic rock solid, water, and hydrocarbons. Modified from Asquith (2014).

In practice, is very difficult to accurately quantify effective and total porosity in shales, due to the inaccuracy in the calculation of the amount of clay-bound water (Passey et al., 2010). Total density porosity can be estimated by taking into account the effect of the mineral matrix and TOC:

$$PHIDT = \frac{RHO_{ma} - RHOB}{RHO_{ma} - RHO_{fl}} \quad (2.9)$$

Where,  $PHIDT$  = total density porosity,  $RHOB$  = density log, and  $RHO_{fl}$  = pore-fluid density.

$$RHO_{ma} = \frac{V_{cal} \times RHO_{cal} + V_{qz} \times RHO_{qz} + V_{ker} \times RHO_{ker} + V_{clay} \times RHO_{clay}}{V_{cal} + V_{qz} + V_{ker} + V_{clay}} \quad (2.10)$$

Where,  $V_{cal}$  = calcite volume,  $V_{qz}$  = quartz volume,  $V_{ker}$  = kerogen volume,  $V_{clay}$  = clay volume,  $RHO_{cal}$  = calcite density (2.71 g/cc),  $RHO_{qz}$  = quartz density (2.65 g/cc),  $RHO_{ker}$  = kerogen density (1.42 g/cc), and  $RHO_{clay}$  = clay density (2.71 g/cc).

The kerogen density is taken from Yenugu and Vernik (2015). The kerogen volume is calculated from the estimated Verniks TOC using Asquith's (2014) formulation:

$$Kerogen(vol) = \frac{TOC(wt.\%) \times RHOB \times K_{vr}}{RHO_{kerogen}} \quad (2.11)$$

Where  $TOC(wt.\%)$  is the TOC calculated in weight percent,  $RHOB$  is the density log,  $K_{vr}$  is the kerogen maturity constant (1.3 for type II kerogen), and  $RHO_{kerogen}$  is the kerogen density (1.42 g/cc).

In the OTIS 2H well, Upper Marcellus shows in average lower total porosity values than Lower Marcellus, which reaches a maximum porosity of approximately 11% at the base of the Lower Marcellus (Figure 2.10), which also shows the highest TOC values (up to 9 wt. %).

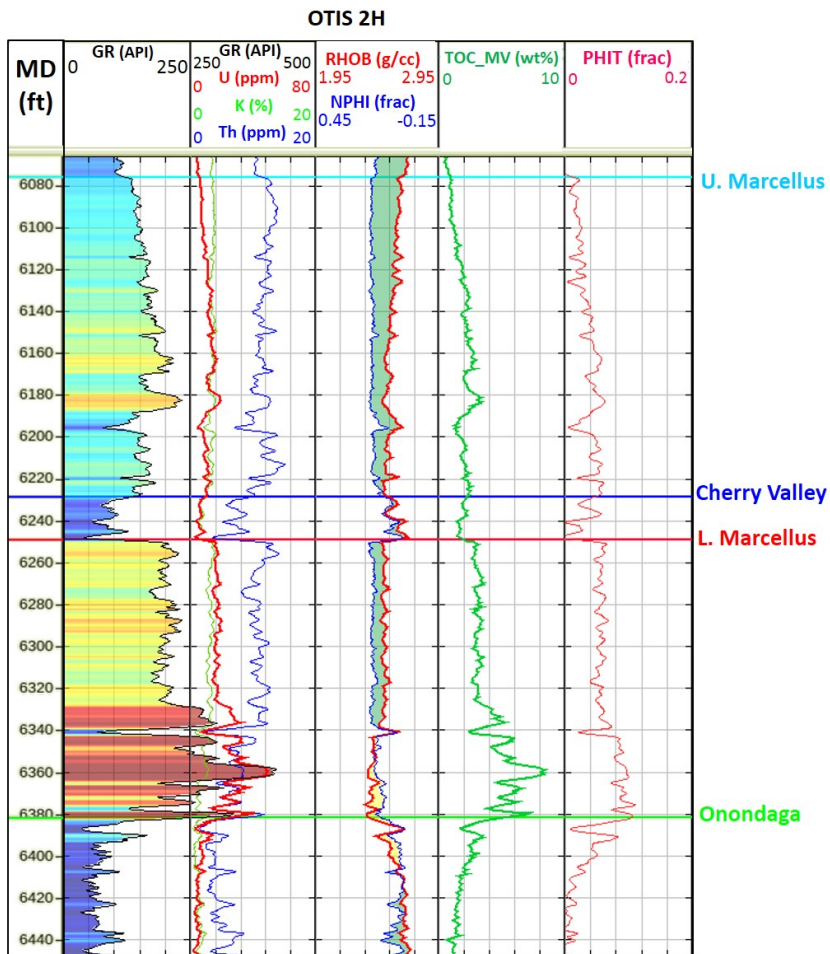


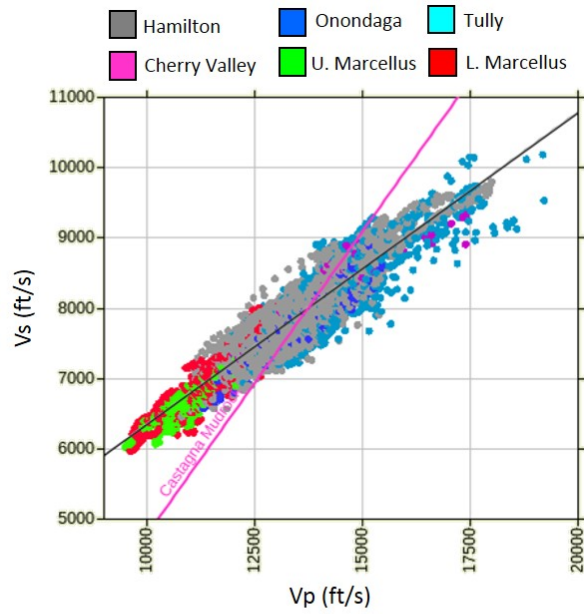
Figure 2.10: OTS 2H well logs. From left to right, total gamma-ray (GR), uranium (U), potassium (K), and thorium (Th), comparison between density (RHOB) and neutron porosity (NPHI), TOC estimation using multi-variate analysis and total porosity (PHIT) estimation.

## 2.4 Cross-plot analysis

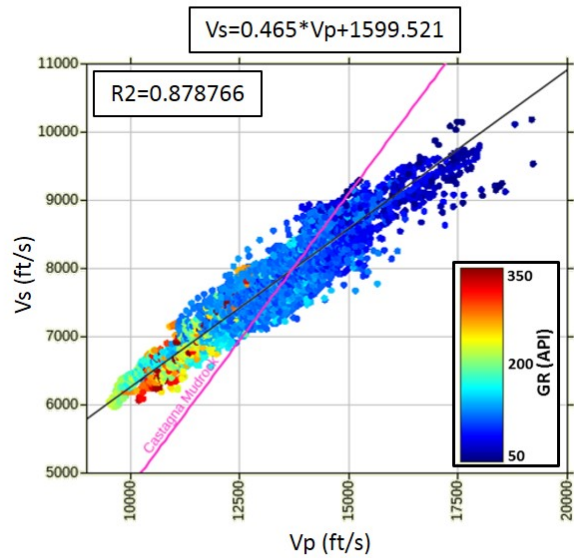
Cross-plots are used to understand the elastic characteristics of the Marcellus Shale and their relationship with the previously estimated petrophysical properties. EICK 1H, THOMAS 1H, and OTIS 2H wells were evaluated and compared.

Figure 2.11 shows cross-plots between  $V_p$  and  $V_s$  for the three wells, color-coded by (a) formation and (b) gamma-ray. The Castagna mudrock line for brine-saturated siliciclastic rocks (Castagna et al., 1985) was plotted as a guideline. Stafford, Tully, and Cherry Valley are high-velocity carbonates that plot towards high  $V_p/V_s$  values, the Hamilton Shale falls somewhat within the mudrock line trend, however both Upper and Lower Marcellus Shale deviate significantly from the trend and show lower P and S-wave velocities, and hence lower  $V_p/V_s$  ratios (around 1.5). This deviation from the background trend might be caused by a combination of fluid (gas saturation) and TOC content. The excellent correlation between  $V_p$  and  $V_s$  allows an adequate linear fit with a correlation coefficient of 0.895.

A lithological trend can be observed in the density vs. P-wave velocity cross-plots (Figure 2.12). The Stafford, Tully, and Onondaga limestones are recognized by their high velocities (<15,000 ft/s) and organic matter rich shales from Upper and Lower Marcellus can be easily discriminated from the inorganic Hamilton Shale in the density domain, showing density values lower than 2.65 g/cc. Gas saturation makes the rock more compressible, causing a substantial decrease in velocity and a moderate decrease in density. The low density of kerogen also has a substantial effect on the elastic properties of the rock (Prasad and Zargari, 2014).

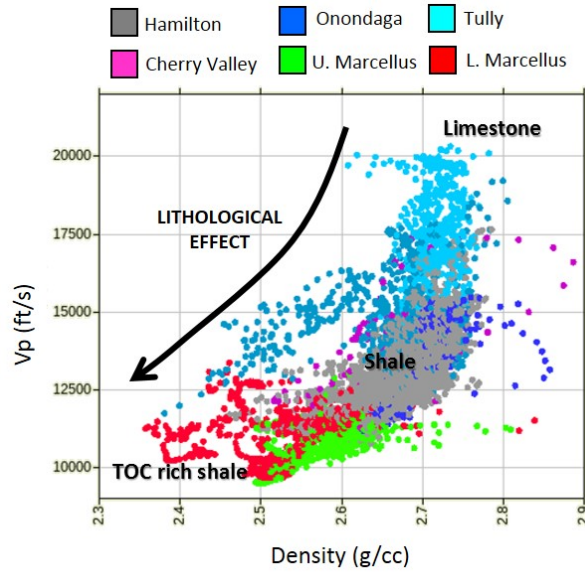


(a)

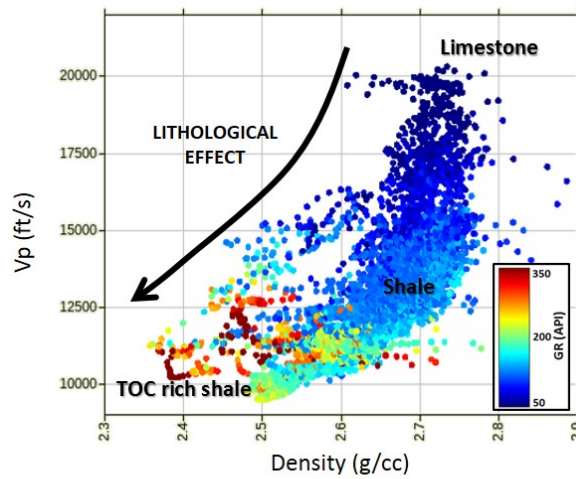


(b)

Figure 2.11:  $V_p$  vs.  $V_s$  cross-plot for EICK 1H, THOMAS 1H, and OTIS 2H, color-coded by (a) formation and (b) GR. Note how both Upper and Lower Marcellus deviate from the Castagna mudrock line (Castagna et al., 1985) towards lower velocities. This could be caused by both gas saturation and TOC content. The excellent correlation between  $V_p$  and  $V_s$  allows an adequate linear fit.



(a)



(b)

Figure 2.12: Density vs.  $V_p$  crossplot for EICK 1H, THOMAS 1H, and OTIS 2H, color coded by (a) formation and (b) GR. Note the lithological trend, where the Upper and Lower Marcellus organic-rich shale can be easily identified in the density domain, showing values lower than 2.65 g/cc.

Although both Upper and Lower Marcellus are organic-rich shales, their mineralogy and elastic properties are different. To understand the behavior of the reservoir rocks, Figure 2.13 shows cross-plots of density vs. P-wave velocity for the Marcellus interval only. These plots include samples from the three wells: EICK 1H, THOMAS 1H, and OTIS 2H. Within the Marcellus interval, rocks with high TOC content higher than 6 wt. % clearly deviate from the ones that have lower TOC content in the density domain, and exhibit lower densities ( $<2.5$  g/cc) and slightly higher velocities. This observation differs from what one would expect. The presence of kerogen leads to a decrease in all the elastic moduli (Sayers, 2013), so a decrease in both density and velocities caused by an increase in TOC is expected. These high TOC rocks also show lower clay content ( $<20$  %) than those with lower TOC content (0.25-0.4 wt. %). These observations agree with previous studies (Luker, 2012; Wang and Carr, 2013). They studied stratigraphy and mineralogic content of the Marcellus Shale using well logs and XRD and found that the most organic-rich sediments tend to be associated with high quartz, calcite, and pyrite content.

Based on this observation and following Wang's (2012) facies classification, where the organic-rich facies have densities lower than 2.5 g/cc, this interval can be separated from the Lower Marcellus, and will now be called "Hot" Lower Marcellus (see Figure 2.15c). Within the "Hot" Lower Marcellus, there is also what seems to be a mineralogic trend, where the lower the density and velocity the lower the clay content. When looking at the cross-plot colored by well (Figure 2.15d), one can note that from the three wells, the OTIS 2H (cyan color) has the lowest clay content within the Marcellus interval and also the "Hot" Lower Marcellus unit.

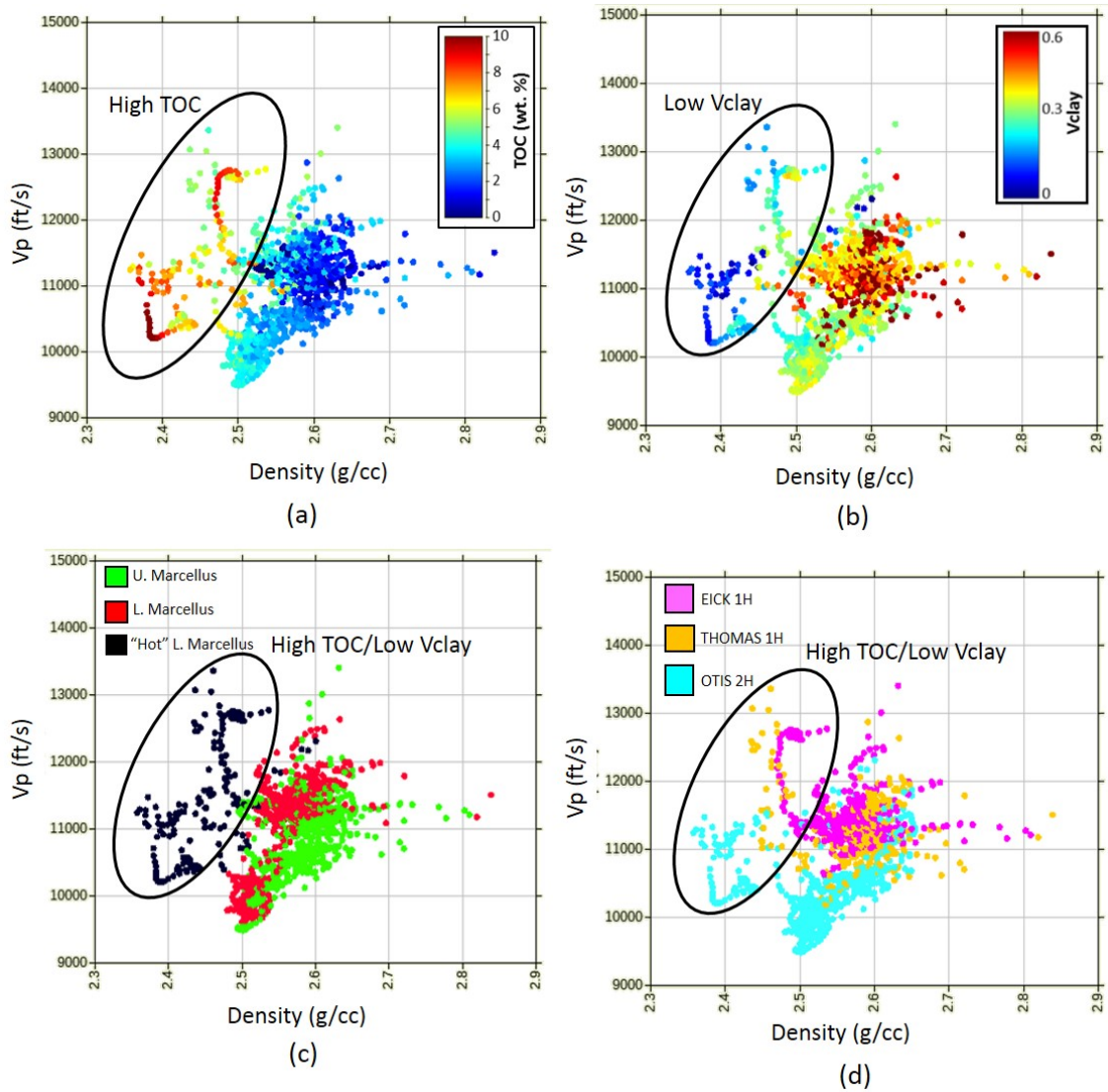


Figure 2.13: Density vs. Vp cross-plots for the Marcellus interval, including the wells EICK 1H, THOMAS 1H and OTIS 2H. Cross-plots are color-coded by (a) TOC (PNS TOC for the EICK 1H well and Vernik and Landis' TOC for OTIS 2H and THOMAS 1H), (b) Vclay, (c) unit and (d) well. The high TOC interval correlate to low densities, high velocities and low-clay content, and are separated in a unit called "Hot" Lower Marcellus, enclosed by the black polygons.

TOC seems to be the principal factor affecting the density in these wells. However, the TOC effect in the velocity seems to be masked by the decrease of clay content and increase of quartz and calcite, which causes an increase in velocity in the "Hot" Lower Marcellus interval. In this sense, the interplay between inorganic minerals seems to be the principal factor driving velocity changes in the high TOC interval.

Figure 2.14 shows cross-plots between  $V_p/V_s$  and density for the three wells color-coded by TOC (2.14a),  $V_{clay}$  (2.14b), interval (2.14c), and well (2.14d). The observations are similar to the previous case: TOC and clay content are the main properties affecting changes in density and  $V_p/V_s$  for the Marcellus interval. In areas with TOC lower than 5 wt. %,  $V_p/V_s$  clearly separates areas with clay content higher than 50 %, where  $V_p/V_s$  values are higher ( $V_p/V_s > 1.65$ ) and areas with clay content lower than 50 %, where  $V_p/V_s$  shows lower values ( $V_p/V_s < 1.65$ ). A similar relation is observed in the high TOC interval, where low  $V_p/V_s$  values correlate to cleaner shales with low clay content ( $> 20$  %). The TOC effect in  $V_p/V_s$  is not as clear as the clay effect. In general, the Marcellus interval shows lower  $V_p/V_s$  values than the inorganic Hamilton shale (see Figure 2.17) due to the presence of TOC and gas content. Within the Marcellus interval,  $V_p/V_s$  seems to slightly decrease in the "Hot" Lower Marcellus interval for the OTIS 2H and THOMAS 1H well samples (cyan and yellow, respectively), however that decrease could be a result of the decrease in clay, since  $V_p/V_s$  is practically not changing, and seems to be even increasing, for the EICK 1H well, where the clay content is more or less constant for the entire Marcellus interval.

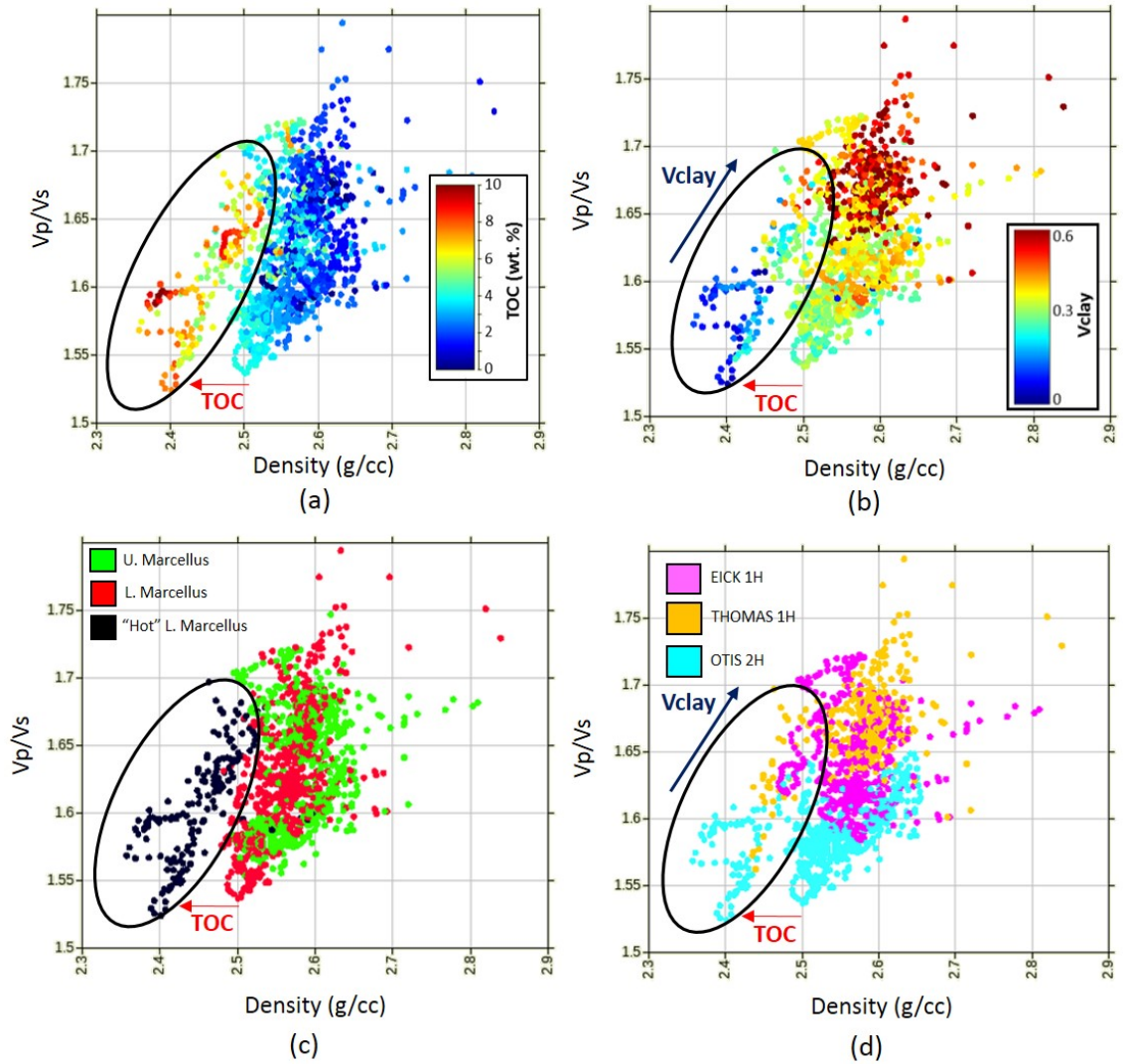


Figure 2.14: Density vs.  $V_p/V_s$  cross-plots for the Marcellus interval, including the wells EICK 1H, THOMAS 1H and OTIS 2H. Cross-plots are color-coded by (a) TOC (PNS TOC for the EICK 1H well and Vernik and Landis' TOC for OTIS 2H and THOMAS 1H), (b)  $V_{clay}$ , (c) unit and (d) well. The black polygon encloses the low-density organic-rich "Hot" Lower Marcellus interval, with TOC values higher than 6 wt. %.  $V_p/V_s$  is a good lithological indicator, showing an increase in their values as clay content increases.

Since  $V_p$  is increasing and density is decreasing in the high TOC "Hot" Lower Marcellus interval, the acoustic impedance is kept more or less constant through the whole Marcellus interval (Figure 2.15). However, acoustic impedance discriminates between low and high clay content in the "Hot" Lower Marcellus, where organic shales with low clay content show lower acoustic impedance than organic shales with higher clay content.

Figure 2.16 shows a comparison between the THOMAS 1H and OTIS 2H logs. Tracks show, from left to right, gamma-ray, uranium, mineral volumes, neutron porosity and density, TOC and total porosity, P and S-wave velocities, P and S-wave impedances, and  $V_p/V_s$ . The THOMAS 1H well has a water-saturation log ( $S_w$ ) that was provided by the petrophysical evaluation of the oil company and shows how both Upper and Lower Marcellus are fully saturated with gas, showing an average of 80 % gas saturation for the whole interval. Even though there is gas present in the whole system, production is optimized by finding zones of high TOC content and high brittleness values. The well-section is colored by the previously defined units. It can be seen that, in general, the Upper Marcellus shows high clay content (0.25 to 0.45), low total porosities (2 to 4 %), low TOC content (2 to 4 wt.%), while the Lower Marcellus shows low clay content (20 to 40 %, however, it can get as low as 0.15 in the "Hot" Lower Marcellus), high total porosities (8 to 11 %), and high TOC (4 to around 10 wt. %). The  $V_p/V_s$  curve decreases at the "Hot" Lower Marcellus due to the decrease in clay and increase in quartz content. Lower Marcellus has more brittle mineral content (e.g. quartz and calcite) than the Upper Marcellus, and it could be more amenable to open and maintain fractures during hydraulic fracturing.

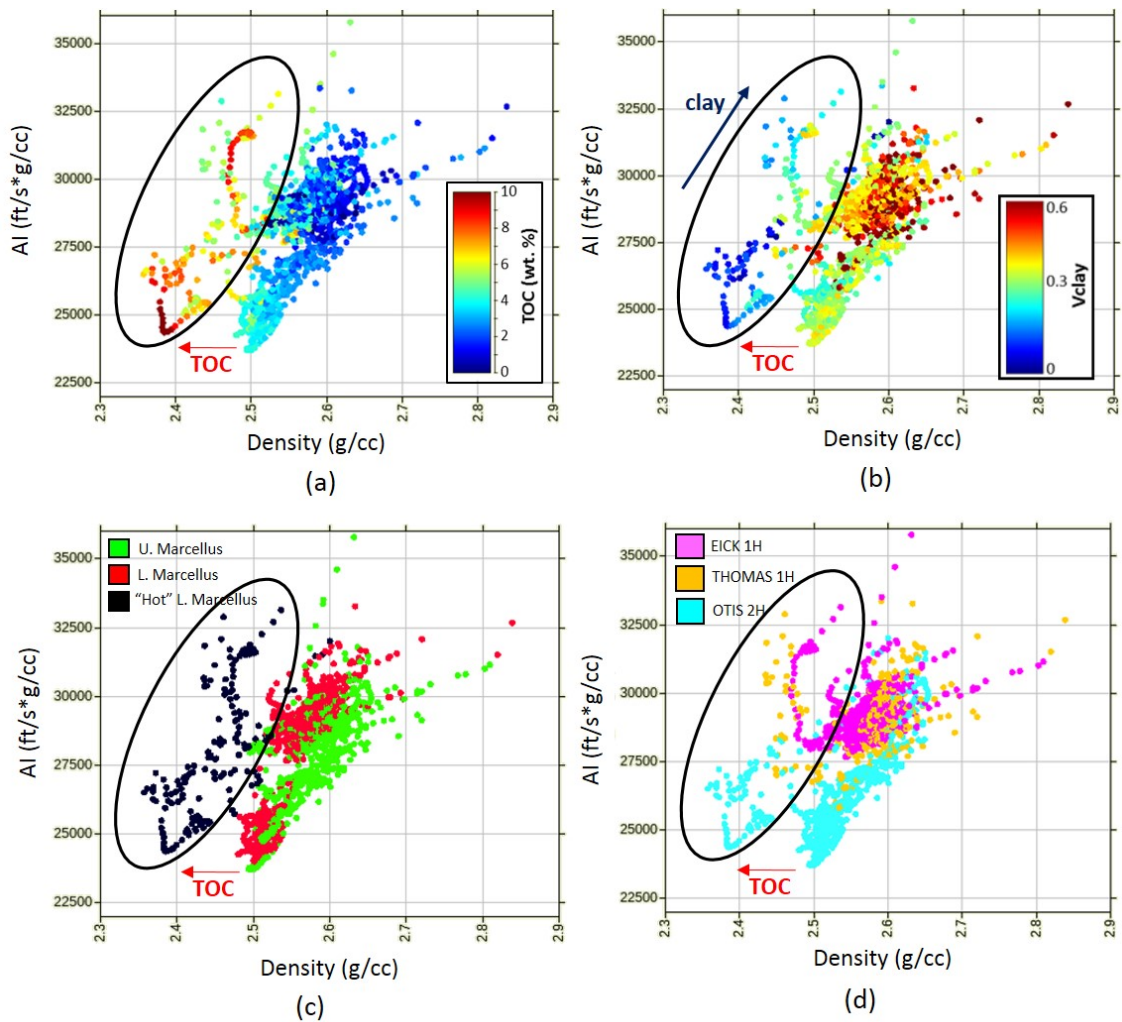


Figure 2.15: Density vs. acoustic impedance (AI) cross-plots for the Marcellus interval, including the wells EICK 1H, THOMAS 1H, and OTIS 2H. Cross-plots are color-coded by (a) TOC (PNS-TOC for the EICK 1H well and Vernik and Landis' TOC for OTIS 2H and THOMAS 1H), (b)  $V_{clay}$ , (c) unit and (d) well. The black polygon encloses the low-density organic-rich "Hot" Lower Marcellus interval, with TOC values higher than 6 wt. %. Acoustic impedance is also a good lithological indicator, showing an increase in their values as clay content increases.

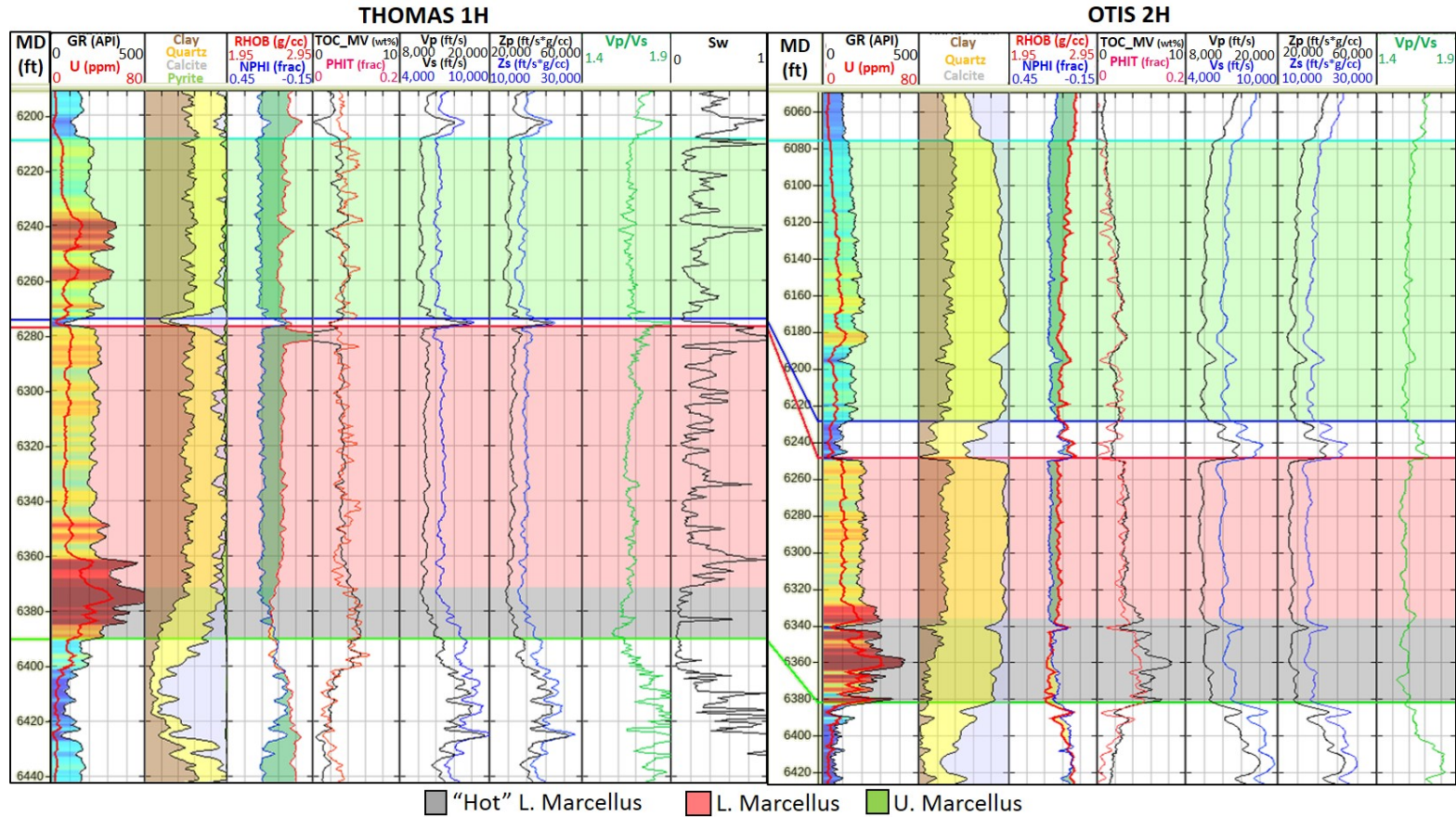


Figure 2.16: Comparison between THOMAS 1H and OTIS 2H well-logs. The Upper Marcellus shows high clay content, low total porosities and low TOC content, while the Lower Marcellus shows low clay content, high total porosities and high TOC. Lower Marcellus has more brittle mineral content (e.g. quartz and calcite) than the Upper Marcellus and it could be more amenable to open and maintain fractures during hydraulic fracturing.

It has been shown earlier that density is a good lithological indicator and organic matter-rich rocks can also be identified in this domain, where a cutoff around 2.5 g/cc separates facies with low TOC content (lower than 6 wt. %) from facies with high TOC content (higher than 6 wt. %). Poisson's ratio, acoustic impedance,  $\lambda/\rho$ , and  $\mu/\rho$  (compressibility and rigidity scaled by density) are commonly used in unconventional reservoirs to extract lithology and pore-fluid information from seismic and well-log data (Goodway, 2001). To test the feasibility of these domains in discriminating high TOC areas, cross-plots of AI vs. Poisson's ratio and  $\lambda/\rho$  vs.  $\mu/\rho$  were generated for the reservoir interval (Figure 2.17) color-coded by unit (Upper Marcellus, Lower Marcellus and "Hot" Marcellus). The high TOC "Hot" Marcellus interval cannot be discriminated in any of these domains, which indicates that the inversion for density is the best attribute that could be potentially used as a proxy for organic content in the study area.

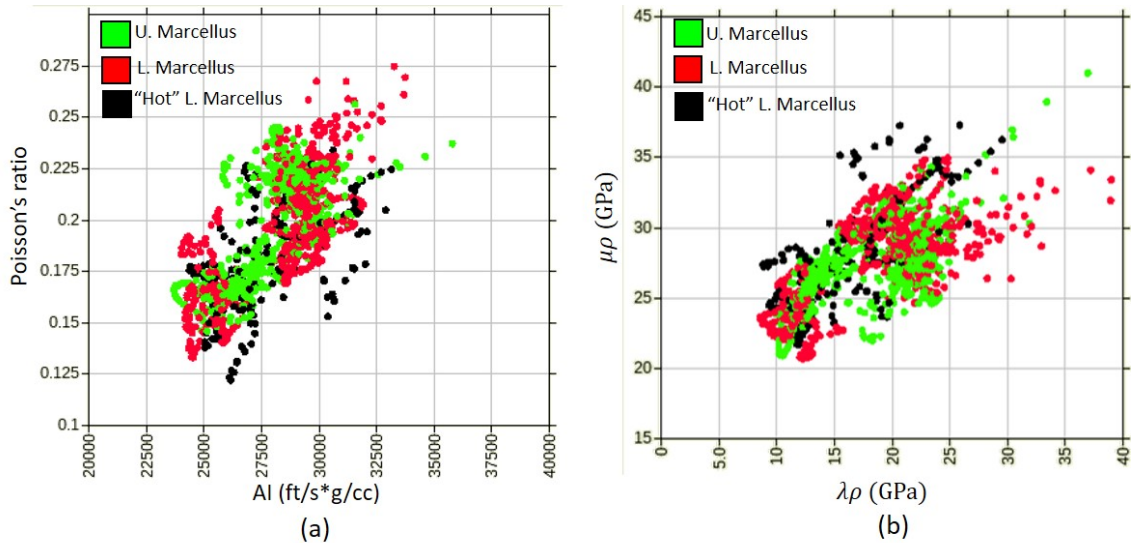


Figure 2.17: Acoustic impedance vs. poisson's ratio (a) and  $\lambda\rho$  vs.  $\mu\rho$  (b) cross-plots of the Marcellus interval, colored by unit. The "Hot" Lower Marcellus unit (black) cannot be easily discriminated in any of these domains.

## 2.5 Brittleness estimation

The key elements for shale resource evaluation are the mineral content (e.g. clay, quartz, and calcite), the total organic carbon (TOC) content, the brittleness and some mechanical properties of the shale rocks (Sharma and Chopra, 2015).

A rocks response to stress can generally be considered either ductile or brittle, and can be differentiated based on the amount of plastic deformation that the rock undergoes before fracture occurs (Sharma and Chopra, 2015). If the rock deforms plastically (e.g. bends or flow), meaning that it absorbs a high amount of energy

before fracturing is considered ductile. Brittle rocks are unable to accommodate significant strain before failure. Hence, they tend to break more easily and can therefore potentially generate microfractures that could remain open during hydraulic fracturing.

Quartz and calcite are brittle materials while clays are more ductile. Hence, high content of quartz and calcite make the rock more brittle, and high content of clay makes the rock more ductile. The mineral volumes of the rock can be estimated by XRD analysis of shale samples (the most accurate method) or evaluation of the log curves. For this study, XRD information was not available. Hence, the mineral volumes were estimated from the log curves. Given the mineral volumes, the brittleness index can be estimated as the fraction of brittle minerals (Jarvie et al., 2007):

$$BI = \frac{V_{qz}}{V_{cal} + V_{qz} + V_{clay}} \quad (2.12)$$

Where  $V_{qz}$ ,  $V_{cal}$ , and  $V_{clay}$  are the quartz, calcite and clay mineral volumes (from 0 to 1).

Rickman et al., (2008) related the brittleness of a rock to the elastic constants Youngs modulus and Poissons ratio, stating that brittle rocks exhibit high values of Youngs modulus and low Poissons ratio. He suggests that a brittleness index (BI) can be computed by a renormalization of Youngs modulus ( $E$ ) and Poissons ratio ( $\nu$ ) over the zone of interest:

$$E_{BRIT} = \frac{E - E_{min}}{E_{max} - E_{min}} \quad (2.13)$$

$$\nu_{BRIT} = \frac{\nu - \nu_{min}}{\nu_{max} - \nu_{min}} \quad (2.14)$$

$$BI = \frac{E_{BRIT} - \nu_{BRIT}}{2} \quad (2.15)$$

This method has been proven useful in many circumstances. However, the renormalization process is somewhat arbitrary and subjective in defining the upper and lower bounds. This results in a BI that provides information only in a relative sense (Cho and Perez, 2014).

Sharma and Chopra (2015) proposed another attribute,  $E\rho$ , which is the product of Young's modulus and density. They state that  $E\rho$  accentuates lithology detection in terms of brittleness since for a brittle rock, Young's modulus would be high, and density might be high too. A variation of this method could be the ratio  $E/\nu$ . They emphasize that this ratio is especially useful when seismic data is being used for determination of  $E$ , which would require the density data. It is usually difficult to determine density from seismic data. Instead,  $E\rho$  can be determined which only requires P and S-impedance, easily derived by impedance inversion of seismic data (Chopra and Sharma, 2015).

Figure 2.18 shows the comparison of the brittleness indexes derived using the mineral volumes, using Rickmans approach and using  $E/\nu$  for the THOMAS 1H, EICK 1H, and OTIS 2H wells. The computed  $E\rho$  curve is also seen. It can be noticed that, even though the scales are different, the four curves show similar trends of increasing brittleness towards the base of the Lower Marcellus, except in the THOMAS 1H

well. For this well, the brittleness calculated through Rickmans approach shows a brittleness decrease at the base of the Lower Marcellus, while the other four curves show a brittleness increase at that level.

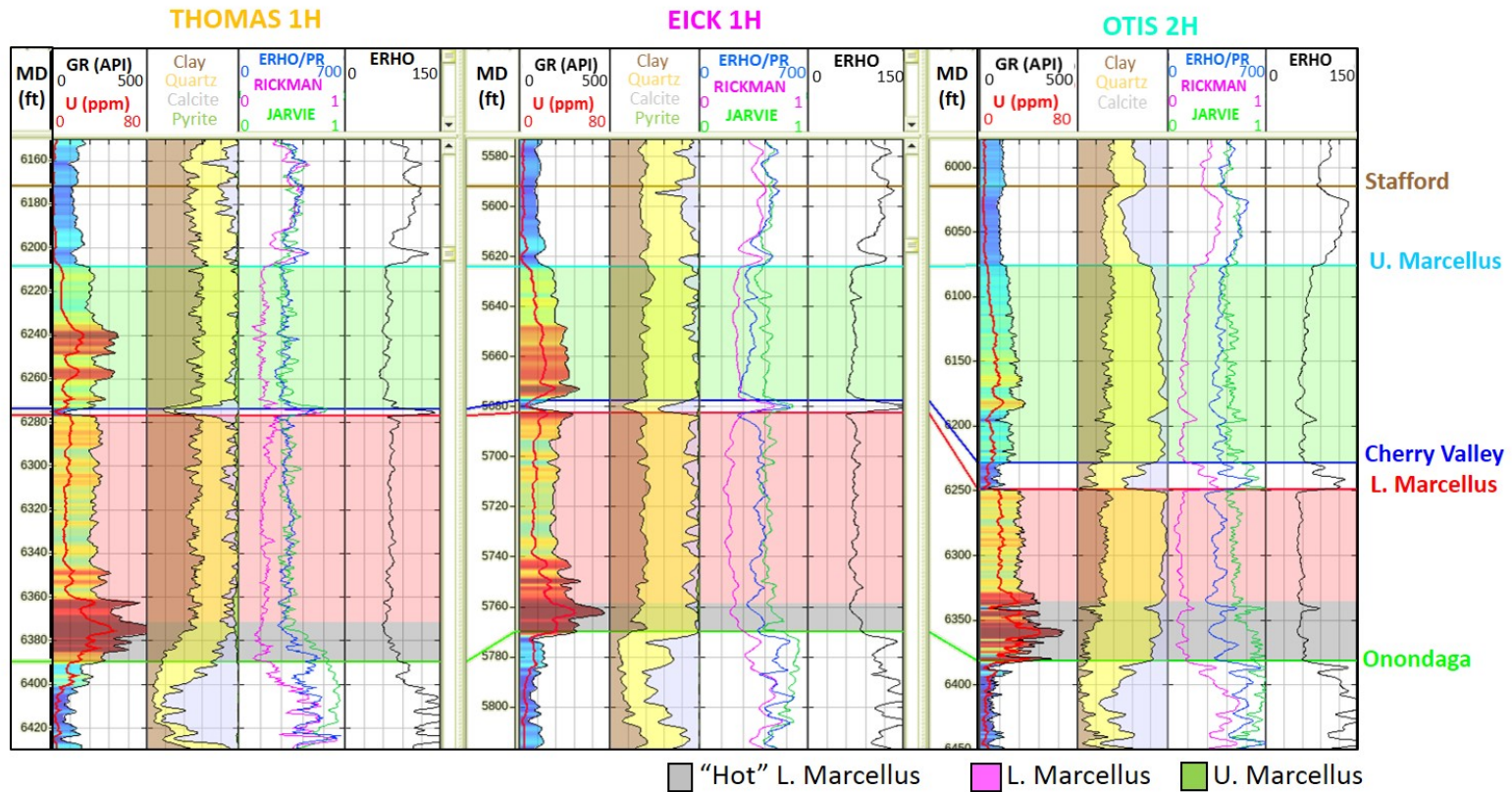


Figure 2.18: Well section through the THOMAS 1H, EICK 1H, and OTIS 2H wells, showing a comparison between the mineral volumes (third track) and the brittleness indexes (fourth track) derived using  $E\rho/\nu$  (blue curve), Rickmans formulation (magenta curve) and the mineral volumes (green curve). The fifth track shows the  $E\rho$  calculation for comparison.

## 2.6 Seismic and rock-physics modeling

### 2.6.1 AVO seismic modeling

As previously shown, the base of the Lower Marcellus ("Hot" Lower Marcellus) shows the highest TOC (higher than 6 wt. %) and lowest clay content (lower than 25 %), when combined causes an increase in both P and S-wave velocities, P-impedance and S-impedance, and a decrease in density. Table 2.1 shows the mean velocities, density, and impedance values and the percentage change between the upper part of the Lower Marcellus (TOC lower than 6 wt. %) and the "Hot" Lower Marcellus intervals. Table 1 shows the mean velocities, density and impedance values and the percentage of change between the upper part of the Lower Marcellus and the "Hot" Lower Marcellus intervals. The arrows next to the percentage of change indicate whether the value of the property increased or decreased. One can observe that both P and S-wave velocities increased about 7 %, while density decreases 3 %. The acoustic impedance (AI) shows a slightly higher increase (3.9 %) than the shear impedance (SI), which increases 3 %.

Seismic modeling is used to understand the effect of the "Hot" Lower Marcellus in the seismic response at the OTIS 2H well. The original P and S-wave sonic and density logs are edited by removing the "Hot" Lower Marcellus interval and replacing it with the Lower Marcellus log values to mimic a low TOC interval (less than 6 wt. %). Figure 2.19 shows a comparison between the original logs (black) and the edited logs (red). The gray polygon highlights the high TOC interval and the red polygon highlights the low TOC upper part of the Lower Marcellus. Note

Property	Low TOC L. Marcellus	"Hot" L. Marcellus	Change (%)
$V_p$ ( $ft/s$ )	10,052	10,776	7 ↑
$V_s$ ( $ft/s$ )	6,385	6,814	7 ↑
Density ( $g/cc$ )	2.51	2.43	3 ↓
AI ( $ft/s \times g/cc$ )	25,262	26,252	4 ↑
SI ( $ft/s \times g/cc$ )	16,045	16,601	3 ↑

Table 2.1: Mean  $V_p$ ,  $V_s$ , density, P-impedance (AI), and S-impedance (SI) values for the upper part of the Lower Marcellus (low TOC) and the "Hot" Lower Marcellus. These values are calculated from the OTIS 2H well logs. The fourth column indicates the percentage of change of each property and the arrows indicate whether the value increased or decreased.

that only the "Hot" Lower Marcellus interval is modified. Finally, PP and PS AVO synthetic seismograms are generated using Kennett's (1983) elastic-wave equations for the two cases: original logs (black) and edited logs (red) where no high TOC interval is present. The wavelets extracted from the stacked PP and PS volumes shown in Chapter 3 are used for the synthetic modeling.

Figure 2.20 shows the comparison between the original (left) and modified (right) PP AVO synthetic seismograms and the AVA response picked at the Lower Marcellus trough (most negative amplitude). The red and blue AVA curves correspond to the amplitudes picked in the synthetic generated using the original and the edited logs, respectively. The picked amplitudes were fitted using the three-term Aki-Richards approximation of the Zoeppritz equations and coefficients values are shown in Table 2.2. Note that both synthetics show negative intercept and positive gradient, that is, the amplitude becomes less negative with offset. Such anomaly is classified as an AVO Class IV by Castagna and Swan (1997) and is caused by a low-impedance rock

below a hard cap rock, which in this case is the Cherry Valley limestone. Vernik and Khadeeva (2013) and Yenugu and Han (2013) computed half-space AVA models for the top of the Eagle Ford and the top of the Barnett Shale, respectively, and also obtained a class IV AVO in both cases. The intercept, gradient, and curvature of the original AVO synthetic show higher values than the edited AVO synthetic, however, the biggest difference corresponds to the gradient and curvature.

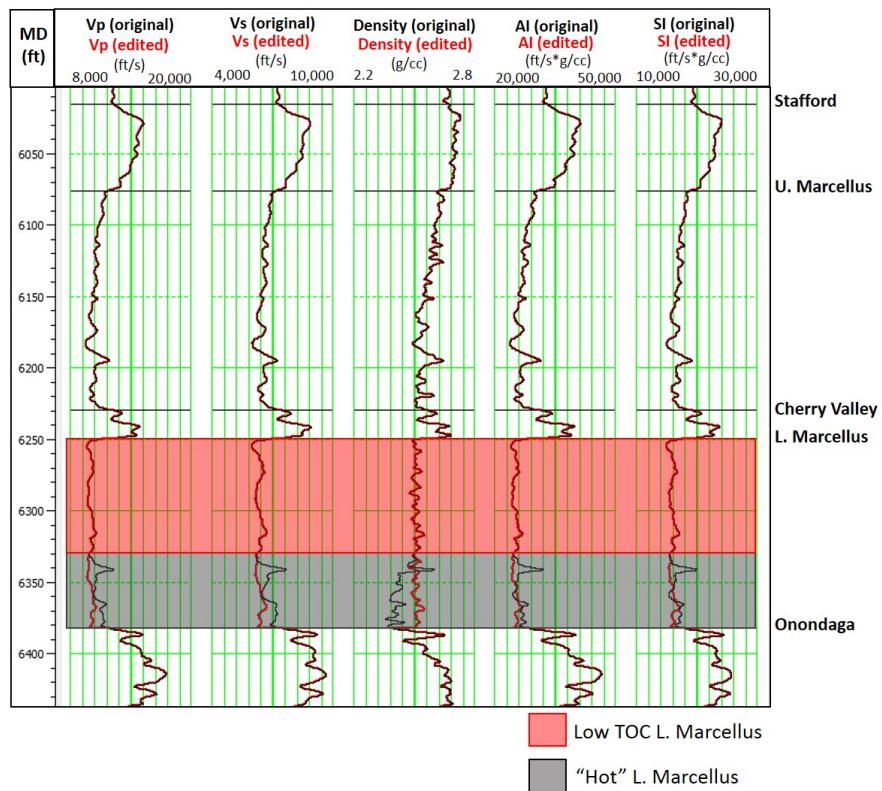


Figure 2.19: Comparison between the original Vp, Vs, density, P-impedance (AI) and S-impedance (SI) logs from the OTIS 2H well (black) and the edited logs (red). The red polygon encloses the low TOC upper part of the Lower Marcellus and the grey polygon the high TOC "Hot" Lower Marcellus.

Figure 2.21 illustrates the comparison between the original (left) and modified (right) PS AVO synthetic seismograms and the AVA response picked at the Lower Marcellus trough. The red and blue AVA curves correspond to the amplitudes picked in the synthetic generated using the original and the edited logs, respectively. It is evident that the difference in amplitude between the AVA curves is greater for the PP than for the PS AVO synthetics. This difference can be easily observed in Figure 2.22, where the percentage difference between the PP (cyan) and PS (magenta) AVA curves are cross-plotted against incidence angle. For both PP and PS cases, the difference in amplitude increases with offset, reaching maximum values ( $\sim 13\%$  for PP and  $10\%$  for PS) at incidence angles around  $35\text{-}40^\circ$ . For the PS case, there is an average amplitude difference of  $2\%$  for near-angles and starts to increase at approximately  $25^\circ$ . For the PP case, the percentage difference is around  $8\%$  for near-angles and starts to increase at approximately  $20^\circ$ . This modeling does not consider the effect of noise. However, in the presence of noise, a difference of  $10\text{ - }34\%$  in amplitude could still be noticeable. The difference between the amplitude variations for the PP and PS cases indicates that the high TOC interval might affect the compressibility more than the rigidity since the P-wave sensitivity seems to be higher than the converted-wave.

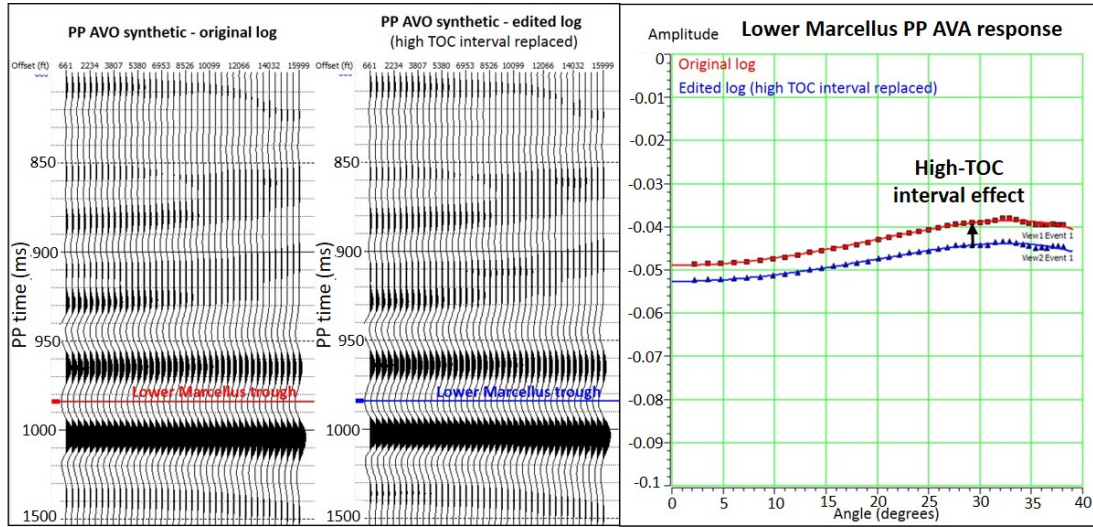


Figure 2.20: Comparison between the PP AVO synthetic gathers generated with the original logs (left) and the edited logs (right). The amplitudes picked at the Lower Marcellus trough are seen in the AVA plot. The red and blue AVA curves correspond to the amplitudes picked in the synthetic generated using the original and the edited logs, respectively. Both synthetics show negative intercept and positive gradient, that is, the amplitude becomes less negative with offset (AVO Class IV).

Coefficient	A	B	C
Original AVO synthetic	-0.049	0.061	-0.059
Edited AVO synthetic	-0.053	0.052	-0.052

Table 2.2: Coefficients for the fitting of the Aki-Richards AVO approximation of the Zoeppritz equation for the AVA curves seen in Figure 2.20. Coefficients A, B and, C correspond to the intercept, gradient and curvature, respectively.

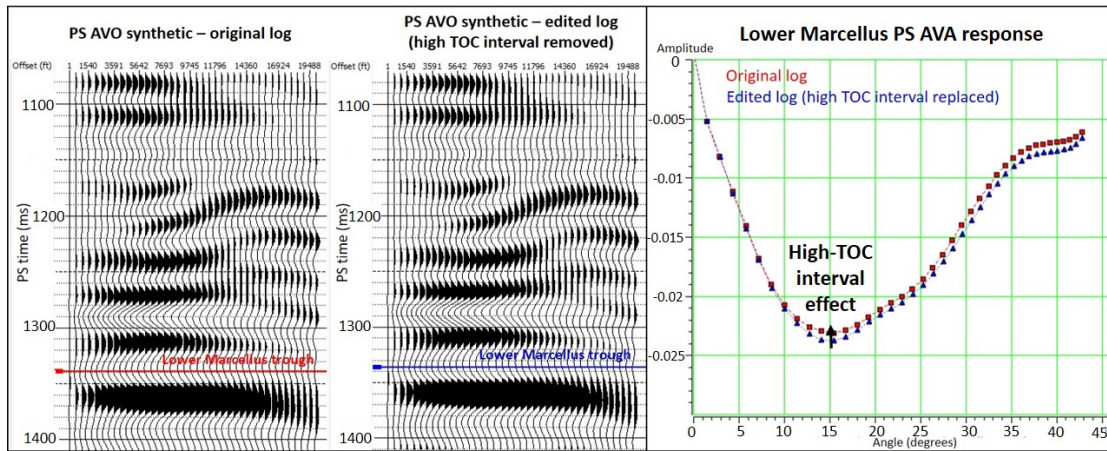


Figure 2.21: Comparison between the PS AVO synthetic gathers generated with the original logs (left) and the edited logs (right). The amplitudes picked at the Lower Marcellus trough are seen in the AVA plot. The red and blue AVA curves correspond to the amplitudes picked in the synthetic generated using the original and the edited logs, respectively.

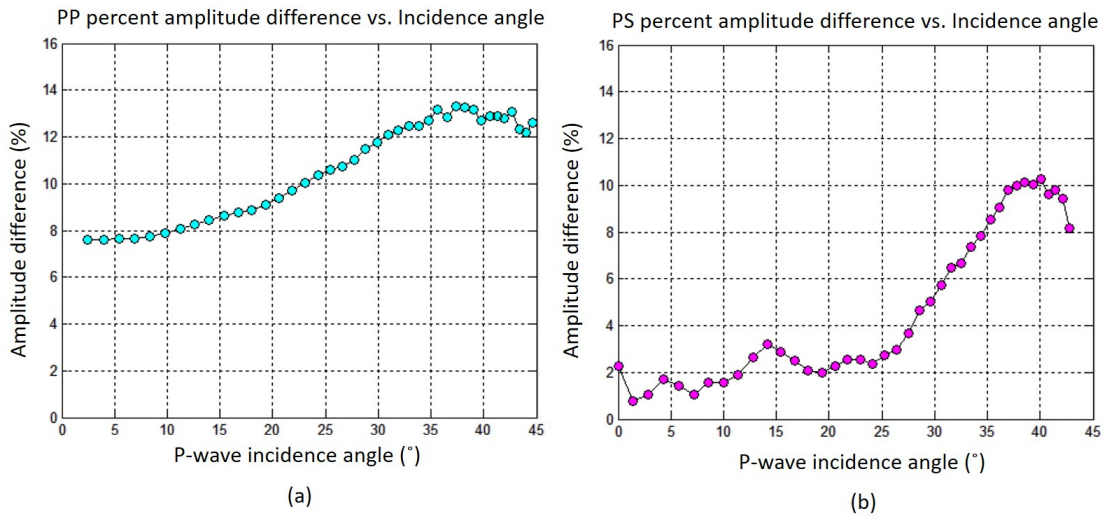


Figure 2.22: Incidence angle vs. amplitude percentage difference. The percentage corresponds to the difference between the AVA curves seen in Figures 2.20 and 2.21 for the PP (a) and PS (b) synthetic seismograms.

## 2.6.2 Rock-physics model

As shown earlier in the chapter, kerogen and clay content play a significant role in the elastic properties of the Marcellus Shale in our study area. A rock-physics model is now used to understand the individual effect of variations in mineralogy, kerogen, and porosity in the rock's elastic response.

Effective medium models are commonly used to characterize organic-rich shales because they are not limited to specific compositions and can model multiple mineralogical phases (Jiang and Spikes, 2012). These models describe a complex medium as a single homogenous medium, assuming that the wavelengths are much larger

than the size of the inclusions (Qin, 2013). In this study, the Differential Effective Medium (DEM) model is used for our analysis.

The DEM theory models the effective moduli of a rock as a two-phase composite by incrementally adding inclusions of phase 2 to the matrix (phase 1) (Mavko et al., 2008). The matrix starts as the background material, and its concentration changes at each step as a new increment of phase 2 material is added. The process continues until the desired concentration of constituents is reached. The DEM model is pathway-dependent, that is, the resulting effective moduli depends on the order in which the inclusions are added. To overcome this issue, the different type of inclusions are added incrementally in a number of steps so the process can be randomized. An example of the variation in the effective bulk moduli resulting from adding quartz to a clay matrix using a different number of steps and the percentage difference between the results is seen in Figure 2.23. As the number of steps increase, the difference between the resulting effective moduli decreases, reaching a 0.002 % difference between the results of adding the inclusions in 90 versus 100 steps.

The difference between incrementally adding 20 % quartz and 20 % kerogen (with aspect ratios of 0.1 and 0.01) to a clay matrix in 100 steps starting with quartz first (black line) and then with kerogen first (magenta line) are seen in Figure 2.24. A zoom-in is seen in Figure 2.24b. The difference between the two is about 0.028 %, which is negligible.

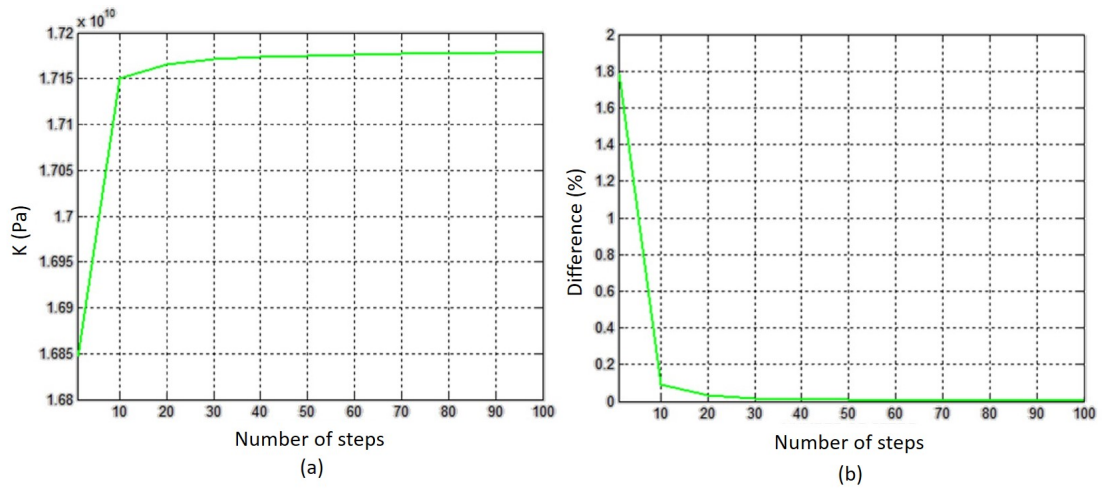


Figure 2.23: Example of the variations in the effective bulk moduli resulting from adding quartz to a clay matrix using different number of steps (1 to 100) (a) and the percentage difference between the results (b).

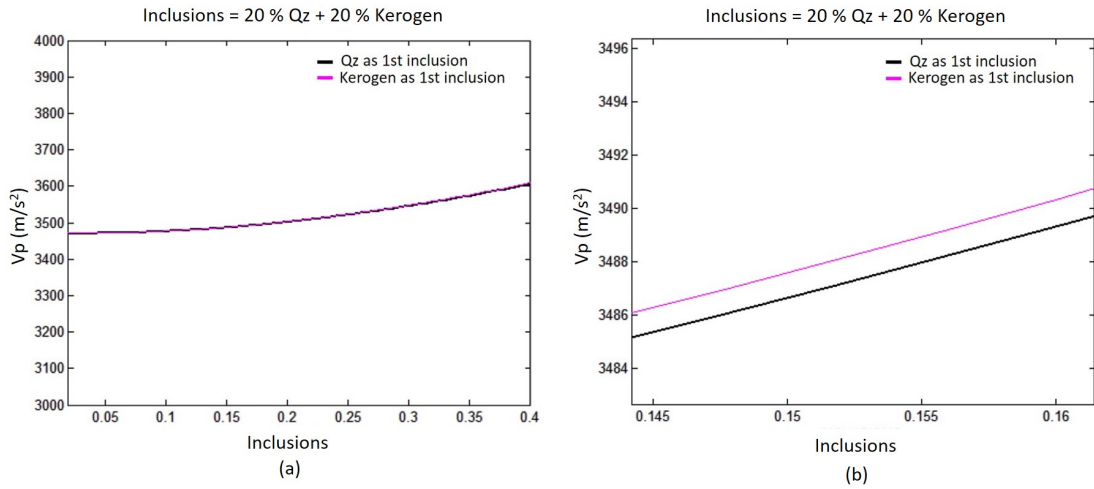


Figure 2.24: Difference between incrementally adding 20 % quartz (aspect ratio = 0.1) and 20 % kerogen (aspect ratio = 0.01) to a clay matrix in 100 steps starting with quartz first (black line) and then with kerogen first (magenta line). A zoom-in is seen in (b), where the difference between the two lines can be better depicted.

The inputs for the DEM model are the mineral volumes and their elastic moduli and the aspect ratio of the inclusions. The model workflow consists of the following steps:

(1) The elastic constants of the host matrix (mix of clay, quartz, and calcite) are calculated using the Voight-Reuss-Hill average.

(2) The inclusions (randomly oriented) are incrementally added in 100 steps using the DEM model. Two types of inclusions are considered: kerogen and porosity. The kerogen aspect ratio is considered as 0.1 (from Qin et al., 2014). The porosity in shales is a complex matter. As mentioned earlier in this chapter, it can be divided

into porosity related to the matrix (inter-particle and inter-granular porosity) and porosity related to the kerogen (Loucks et al., 2012). The matrix porosity tends to be more compliant and has lower aspect ratios than the kerogen porosity (Moyano et al., 2012; Curtis et al., 2012; Coyle and Spikes, 2014). The difference in aspect ratio between both types of porosities can be observed in a backscattered electron image of Marcellus Shale in Figure 2.25. In this study, the total porosity of the system is divided in two: a stiff porosity related to the kerogen with an aspect ratio of 0.2 (Qin et al., 2014) and a soft porosity associated with the matrix porosity which aspect ratio is used as a fitting parameter in the model and varies from 0.01 to 0.05. A similar approach is used by Ruiz and Azizov (2011). The kerogen porosity is assumed to be 30 % (Yenugu and Vernik, 2015), which corresponds to approximately 50 % of the total porosity.

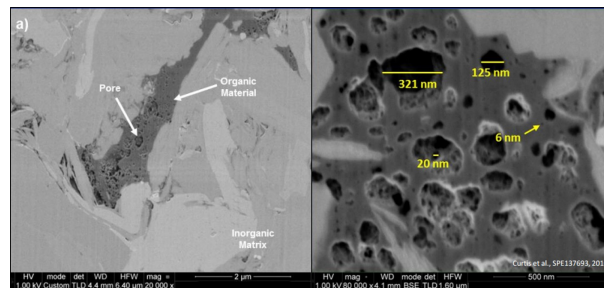


Figure 2.25: Backscattered electron image of Marcellus Shale showing the difference in aspect ratio between the compliant matrix-related pores and the rounded (stiffer) kerogen-related pores. (From Curtis et al., 2012)

The DEM model assumes the inclusions are isolated (and do not become connected even at high concentrations) and pore pressures are unequilibrated (Mavko et

al., 2008). These assumptions are valid for shales due to their low porosity and low permeability, thus pores saturated with gas (kerogen pores) and with a gas-water mix (matrix pores) can be directly added as inclusions (Guo et al., 2014).

The elastic moduli and densities of the minerals included in the model are specified in Table 2.3. The kerogen moduli are taken from Qin et al., (2014). The reservoir fluid properties are calculated using the Batzle-Wang relations.

Material	$\rho$ (g/cc)	$K$ (GPa)	$G$ (GPa)
Quartz	2.65	45	36.6
Clay	2.71	22	8
Calcite	2.71	76	32
Kerogen	1.42	5	2.5
Gas	0.22	0.054	0
Brine	1.008	2.65	0

Table 2.3: Elastic moduli and densities used in the model.

To calibrate the model, five facies are defined in the OTIS 2H well based on clay volume, total porosity, and TOC content (Figure 2.26 ), where the green facies represent the high-TOC/high-porosity "Hot" Lower Marcellus, the black facies represents the low-TOC/high-clay/low-porosity top of the Upper Marcellus, the blue facies represents the interbedded limestones, including the Cherry Valley limestone, and the red and cyan facies represent middle clay content with porosities lower and higher than 5 %, respectively. Since the blue facies is practically a limestone and not a shale, it will not be included in the modeling. The aspect ratio of the matrix-related porosity is used as a fitting parameter for each facies. An example of the calibrated model in the P-wave velocity vs. total porosity space for the green facies ("Hot"

Lower Marcellus) is shown in Figure 2.27. The mineralogical composition of the line corresponds to 15 % clay, 60 % quartz, 10 % calcite and 15 % kerogen.

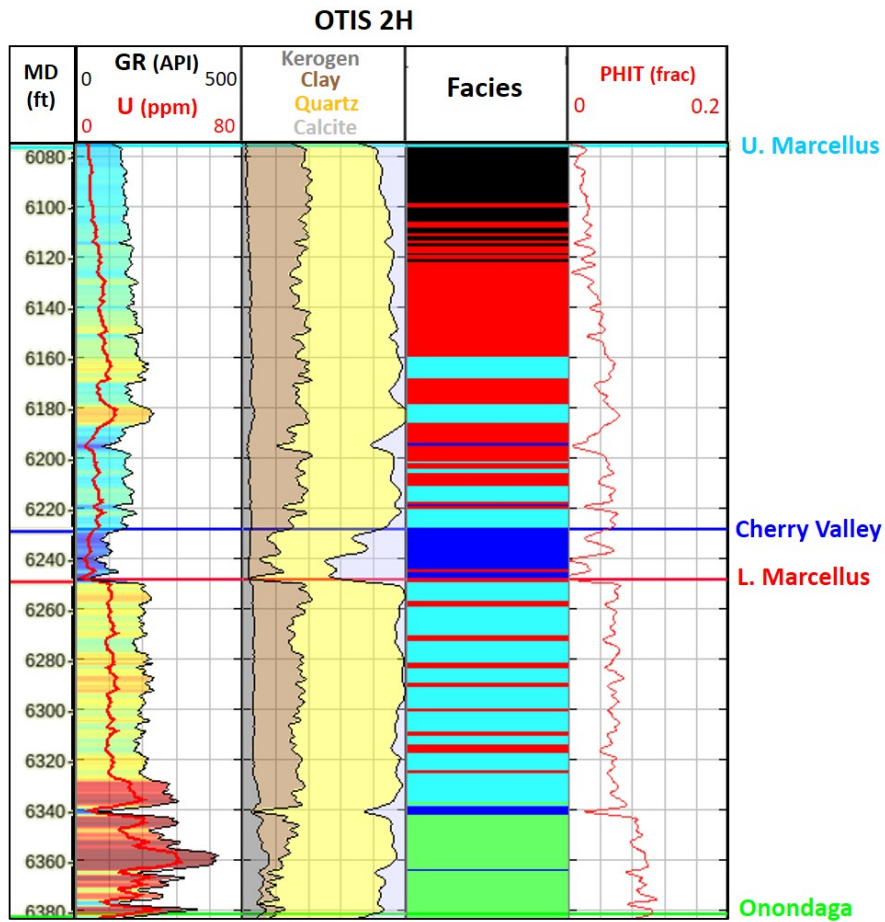


Figure 2.26: OTIS 2H well showing the gamma-ray and uranium logs, the mineral volumes (including the kerogen volume), the facies classification and the total porosity log. Facies are defined in terms of porosity, clay volume, and TOC content. The black facies represents porosities lower than 3 % and clay volumes higher than 35 %, red and cyan facies indicate clay content lower than 35 % and porosities lower and higher than 5 %, respectively, the blue facies are the interbedded limestones (including the Cherry Valley limestone), and the green facies represents TOC content higher than 10 % (in volume), porosities higher than 8 % and clay content lower than 25 %.

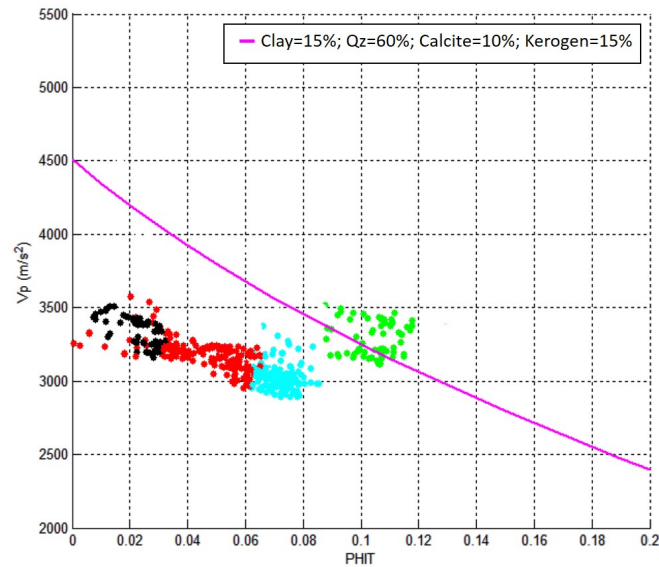
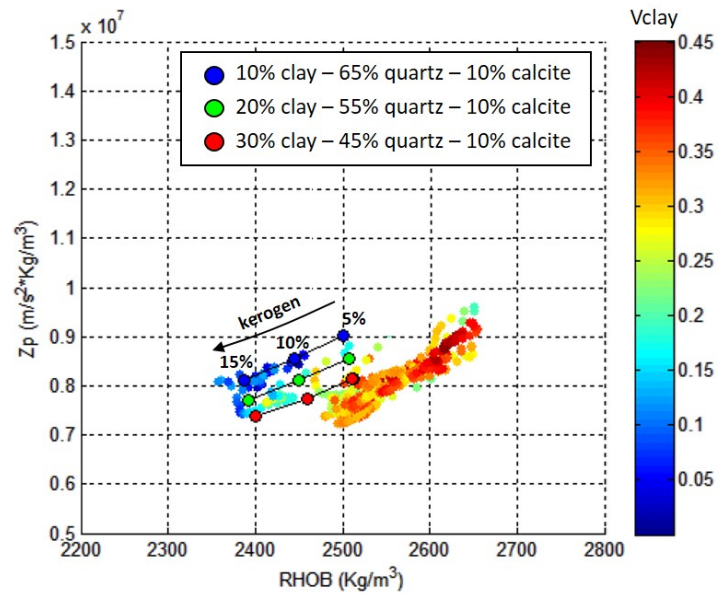


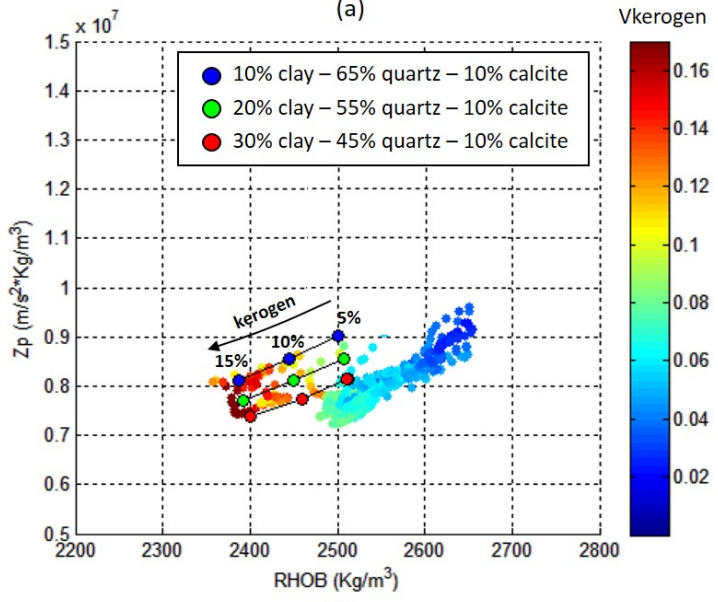
Figure 2.27: P-wave velocity vs. porosity for the Marcellus Shale interval at the OTIS 2H well color-coded by the previously defined facies. The magenta model line is calculated to fit the green "Hot" Lower Marcellus facies and is composed by 15 % clay, 60 % quartz, 10 % calcite, and 15 % kerogen.

To study and compare the effect of kerogen and clay content on P-impedance and density, three models with constant mineralogy are built, and the kerogen content is varied from 5 to 15 % (Figure 2.28). Model lines are composed by constant 10 % calcite, varying the clay/quartz proportions as following: 10 %/65 % (blue) , 20 %/55 % (green), and 30 %/45 % (red). These models suggest that density is more sensitive to kerogen content than P-impedance while P-impedance is more sensitive to clay content variations than density. Additionally, P-impedance decrease as clay content increases. However, clay content variations might also be associated with porosity variations, which also affect the elastic properties of the rock. The effect of porosity

and clay content is seen in Figure 2.29 for two models with 30 % clay (red line) and 40 % clay (black line). A small change in porosity has big effects on both density and P-impedance which implies a large effect on P-wave velocity. As porosity decreases, the density appears to increase its sensitivity to changes in clay content. Note that if clay increases from 30 to 40 % while decreasing 2 % porosity, the P-impedance now increases instead of decreasing, which suggests that the effect of porosity on P-wave velocity might be larger than the effect of increasing clay content, and would help explain the previously observed decrease in P-impedance while reducing clay content (Figure 2.15).



(a)



(b)

Figure 2.28: Rock-physics modeling results showing the separate effects of kerogen and clay content variation on density and P-impedance. The OTIS 2H Marcellus Shale well-log data is plotted in the background colored by clay (a) and kerogen (b).

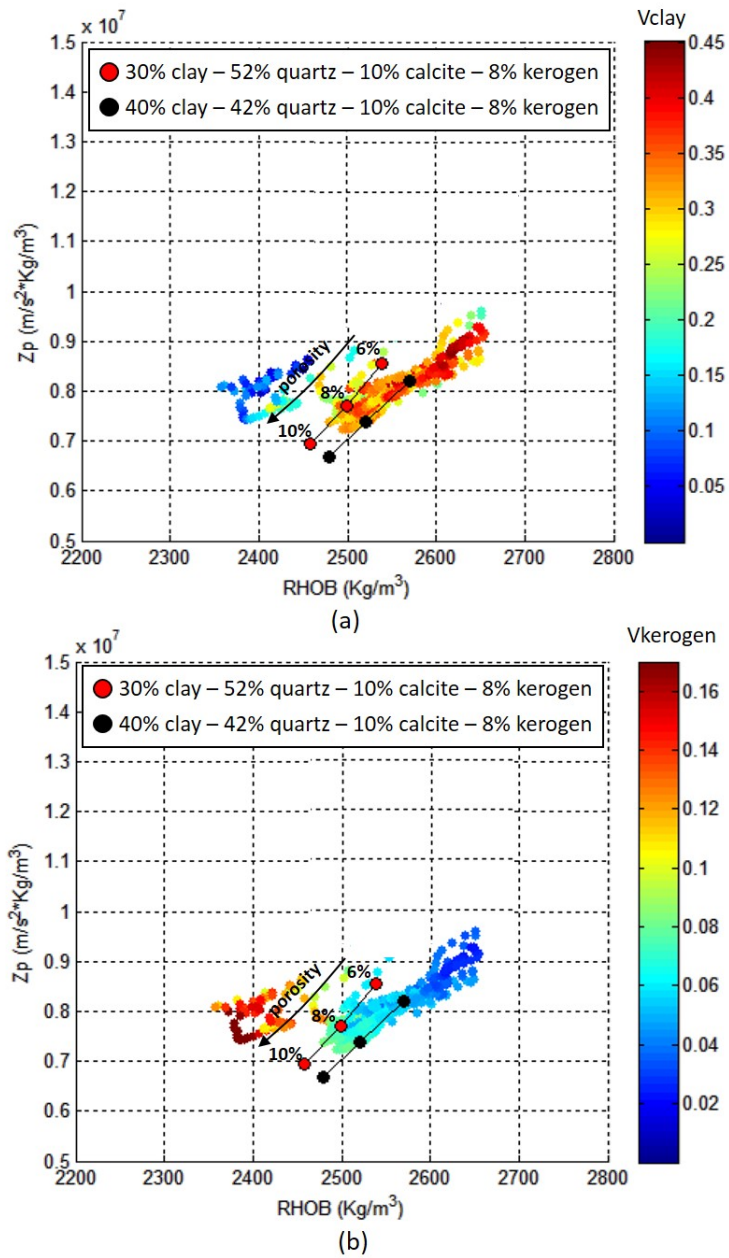


Figure 2.29: Rock-physics modeling results showing the separate effects of porosity and clay content variation on density and P-impedance. The OTIS 2H Marcellus Shale well-log data is plotted in the background colored by clay (a) and kerogen (b).

# Chapter 3

## Seismic interpretation

A general seismic interpretation is undertaken using the stacked PP and PS volumes in their native times. The well-to-seismic tie is performed, and six main events are picked in both volumes. Structural maps and a suite of geometrical-seismic attributes are generated.

### 3.1 PP seismic interpretation

#### 3.1.1 Well-to-seismic tie and seismic resolution

A good well-to-seismic tie is fundamental to achieve reliable inversion results. Hence, the wavelet estimation is a critical step. First, a statistical wavelet is estimated in an interval that includes the reservoir. It calculates the frequency spectrum but not the phase spectrum, so a constant zero phase is selected. Second, a preliminary

tie is done, trying to achieve a high correlation between the synthetic and the real seismic without stretching and squeezing the well-logs more than necessary, because small perturbations in the time-depth relationship will cause large variations in the  $V_p/V_s$  function that will be used to register the PS seismic data to PP time (further details on the PP-PS registration process are discussed in Chapter 4). After a good correlation has been achieved with the first tie, a full wavelet is extracted in a window that includes the reservoir (see Table 3.1 for wavelet extraction parameters), using the sonic and density logs from the well. This method calculates both the frequency and phase spectra. The final PP wavelet and its corresponding frequency spectrum are seen in Figure 3.1.

The time-depth curve from the VSP (the true time-depth relation) acquired at the well is applied before tying the well. VSP data usually has higher frequency content than surface seismic (Chopra et al., 2003). To correlate and compare them is generally useful to filter the VSP to match the seismic-frequency bandwidth. Hence, a 5-10-40-60 Hz bandpass filter is applied to the zero-offset VSP corridor stack. Figure 3.2 shows the P-wave sonic, density, and P-impedance logs, a zero-offset synthetic seismogram computed with an 80 Hz Ricker wavelet (to correlate the high-frequency VSP to the well-log data), the original P-wave corridor stack, the corridor stack filtered (5-10-40-60 Hz), a zero-offset synthetic seismogram computed using the previously extracted wavelet (see Figure 5.1), the real trace extracted from the well location (red) and an inline of the real PP seismic going through the well, with the synthetic inserted at the well location. There is an excellent agreement between the synthetics, the zero-offset VSP corridor stack and the seismic data. The correlation

coefficient between the synthetic computed with the extracted wavelet and the real seismic is 0.83.

Extraction parameters	PP wavelet
Window length	435 ms
Wavelet length	200 ms
Taper length	25 ms
Sample rate	2 ms

Table 3.1: Parameters for the PP full-wavelet extraction at the OTIS 2H well.

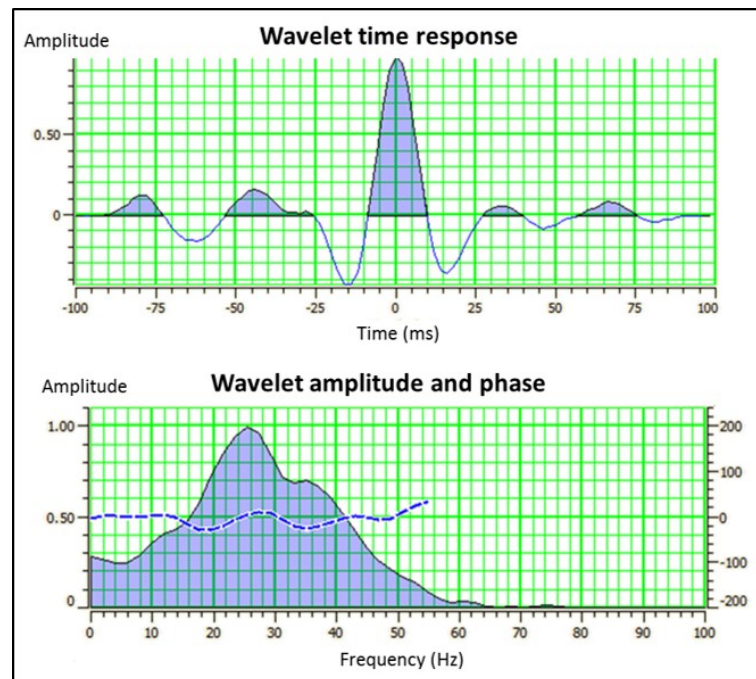


Figure 3.1: PP full wavelet and its corresponding frequency spectrum. The full wavelet extraction is performed in a window from 600 to 1035 ms (a 435 ms window length).

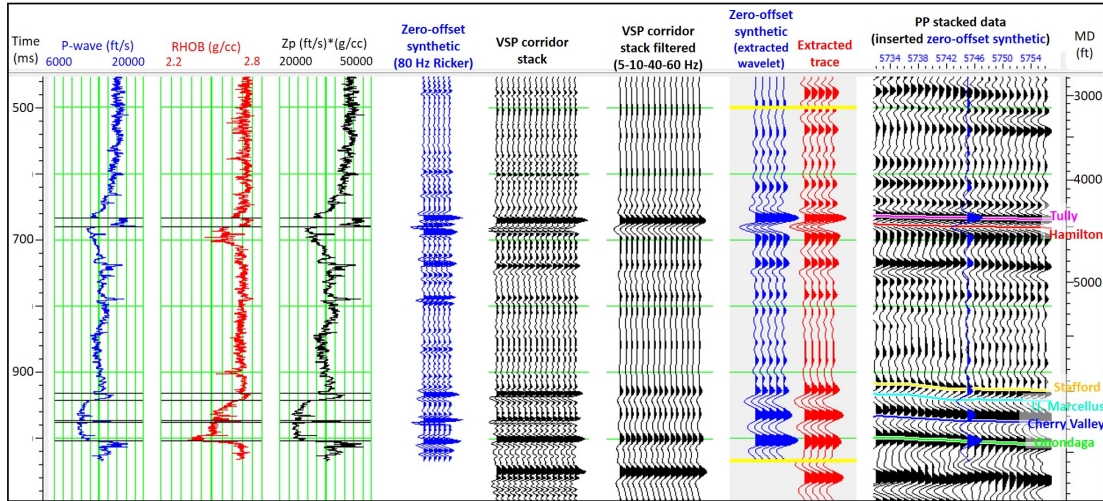


Figure 3.2: OTIS 2H well-to-seismic tie and VSP comparison. From left to right, tracks show the P-wave, density, and P-impedance logs ( $Z_p$ ), a zero-offset synthetic computed using an 80 Hz Ricker wavelet, the P-wave VSP corridor stack, the P-wave VSP corridor stack filtered (5-10-40-60 Hz bandpass filter), the zero-offset synthetic computed with the wavelet extracted from the seismic, the trace extracted from the real seismic at the well location and the real PP seismic going through the well location. There is an excellent agreement between the synthetics, the corridor stack and the seismic data.

Seismic resolution analysis is fundamental in any interpretation project, as one needs to know if the reflection amplitudes are affected by tuning effects, which causes constructive or destructive interference between interfaces that are closely spaced. As previously shown, the Marcellus interval is comprised of an Upper and a Lower member, separated by the thin Cherry Valley limestone. At the well location, the Upper and Lower Marcellus intervals are 150 ft and 130 ft thick, respectively. The

Cherry Valley limestone is only 20 ft thick while the Stafford limestone that overlies the Upper Marcellus is 62 ft thick.

According to Widess (1973), the resolution limit is about one-quarter of the wavelength, which corresponds to around 102 ft for the PP seismic. These values were estimated using the P-wave average RMS velocities calculated from the dipole sonic interval velocities at the reservoir level (P-wave velocity = 13,500 ft/s). The dominant frequency for the vertical-resolution estimation is calculated as the reciprocal of the dominant period of the extracted PP wavelet (see Figure 3.1), where the peak-to-trough time of the wavelet is equal to one-half of the dominant period. The dominant frequency corresponds to 33 Hz for the PP data.

This calculation indicates that it should be possible to resolve both Upper and Lower Marcellus units in the seismic data. A wedge model was generated for the PP data to understand how the thin limestones that overlay both units could be affecting the resulting waveform and vertical-resolution. This model is generated using Zoeppritz equations, therefore taking into account only primaries, and adopt the Widess method of thickness estimation (Widess, 1973). The wavelet used for the modeling is the one previously extracted from the seismic (see Figure 3.1), and used for the well-to-seismic tie. The wedge model is generated varying the Lower Marcellus thickness from 0 to 500 ft (Figure 3.3). The P-wave seismic log is inserted at the real thickness of the unit (130 ft). The Stafford limestone (thin) is causing a 90° phase-shift that results in an interesting interference pattern, where the Cherry Valley limestone corresponds to a zero crossing, and the base of the Lower Marcellus (Onondaga top) corresponds to the center of a peak. Despite the phase-shift in the

resulting waveform, at 130 ft thick, we are above one-half of the dominant period of the wavelet (peak-to-through time), which corresponds to Widess vertical-resolution limit. This indicates that the seismic is, in fact, resolving the Lower Marcellus unit, and therefore resolving the Upper Marcellus interval, which it is 30 ft thicker than the Lower Marcellus.

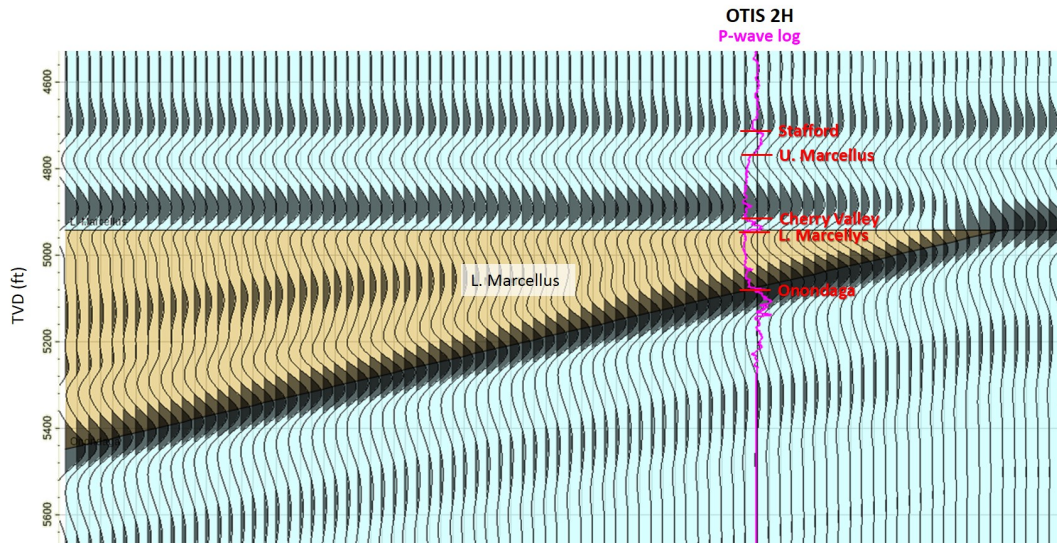


Figure 3.3: Wedge model generated using the PP extracted wavelet. The Lower Marcellus (golden color wedge) thickness is varied from 0 (right) to 500 ft (left). The OTIS 2H P-wave log is inserted at the real Lower Marcellus thickness (130 ft). The thin Stafford limestone (62 ft thick) causes a  $90^\circ$  phase-shift in the resulting waveform. At 130 ft thick we are above one-half of the dominant period of the wavelet (peak-to-through time), which corresponds to Widess vertical-resolution limit.

### 3.1.2 Geometric attributes

The Marcellus Shale interval is affected by a series of thrust faults trending from east to west. These are easily recognized in an arbitrary line running north-south, from A to A' (Figure 3.4). These faults seem to be limited to the Marcellus and Lower Hamilton Group.

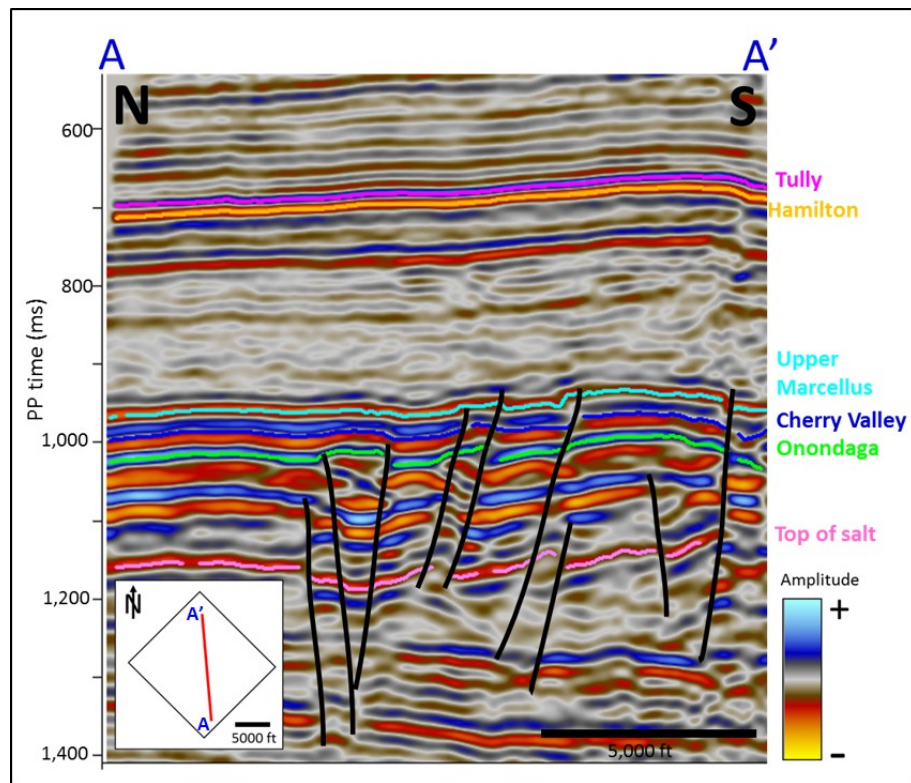


Figure 3.4: Arbitrary line running from north to south, showing a series of inverse faults that affect the Marcellus interval.

Similarity and curvature are used to highlight the faults and try to identify natural fractures. These geometric attributes are widely used in structural interpretation to visualize and delineate faults and fracture zones. The curvature is a 2D second-order derivative of time or depth structure, which measures subtle lateral and vertical

changes in dip that could be overpowered by stronger, regional deformation (Chopra and Marfurt, 2011). In 3D, any surface is defined by two orthogonal principle curvatures:  $k_1$  and  $k_2$ , where  $k_1$  is the most positive curvature and  $k_2$  the most negative curvature. The most positive curvature ( $k_1$ ) highlights the upthrow side of faults while the most negative curvature ( $k_2$ ) highlights the downthrown side of faults. The similarity is indicative of how much two or more trace segments look alike. A similarity of one means that the trace segments are identical in waveform and amplitude while a similarity of zero means that they are completely dissimilar.

Figure 3.5 shows a vertical slice through the PP seismic amplitude co-rendered with the most negative curvature. Note how strong negative values of the most negative curvature highlight the footwalls or downthrown side of the faults and subtle changes in the continuity of the horizons. The extracted similarity co-rendered with the most negative curvature at the Cherry Valley horizon, along with the PP time-structure map are seen in Figure 3.6. The line shown on the maps correspond to the N-S section in Figure 3.4. Both similarity and the most negative curvature highlight faults trending approximately E-W. These faults have been previously identified by Rebec and Zhao (2013), and are referred by Engelder et al., (2009) as the Valley and Ridge features. These are a series of tight parallel folds caused by a compressional stress regime. Rebec and Zhao (2013) mentioned that the elongated tight folds are similar to small thrust-like pushup structures with relaxation resulting in numerous approximately parallel E-W faults and folds seen on the geometric attributes.

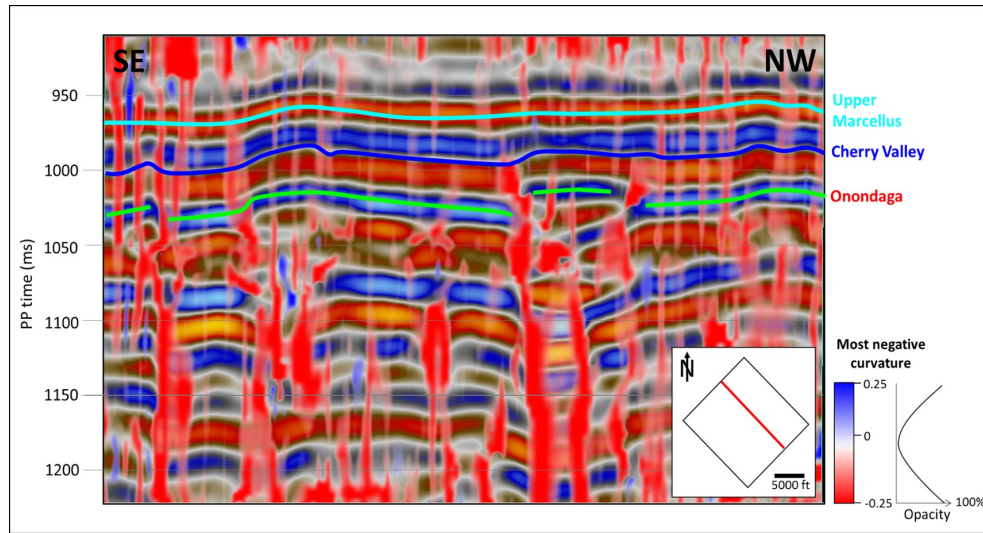


Figure 3.5: Vertical slice through the PP seismic amplitude co-rendered with the most negative curvature. Note how the most negative curvature values are associated with the footwall blocks of the faults.

Engelder et al., (2009) also identified two joint sets, J1 and J2. The J1 set trends approximately in this same direction, however, these are at sub-seismic resolution. He states that, at depth in basins where stress is compressional, tension is an effective stress and joints are natural hydraulic fractures. The proximity to these joint sets is believed to be one of the factors that control the production in the Marcellus shale. Unfortunately, the acquisition footprint does not allow to identify small-scale fractures in the curvature maps.

Dip and Azimuth attributes show trace-to-trace variations in reflection character (Mondt, 1993). Dip azimuth gives the azimuth of the dip direction in degrees, measured from 0 to 360 degrees, and it used to illuminate subtle faults that have

a displacement significantly less than the size of a seismic wavelet (Godfrey and Bachrach, 2008). Figure 3.7 shows the comparison between the maximum negative curvature and the dip azimuth at a time slice at 1000 ms, which corresponds to approximately the middle of the Marcellus interval. The local azimuth attribute helps highlight small-scale discontinuities in the east-west and southeast-northwest directions, which are evidence of north-south compression stress (Wang, 2012). Once again, the acquisition footprint is precluding the accurate identification of fractures in the area.

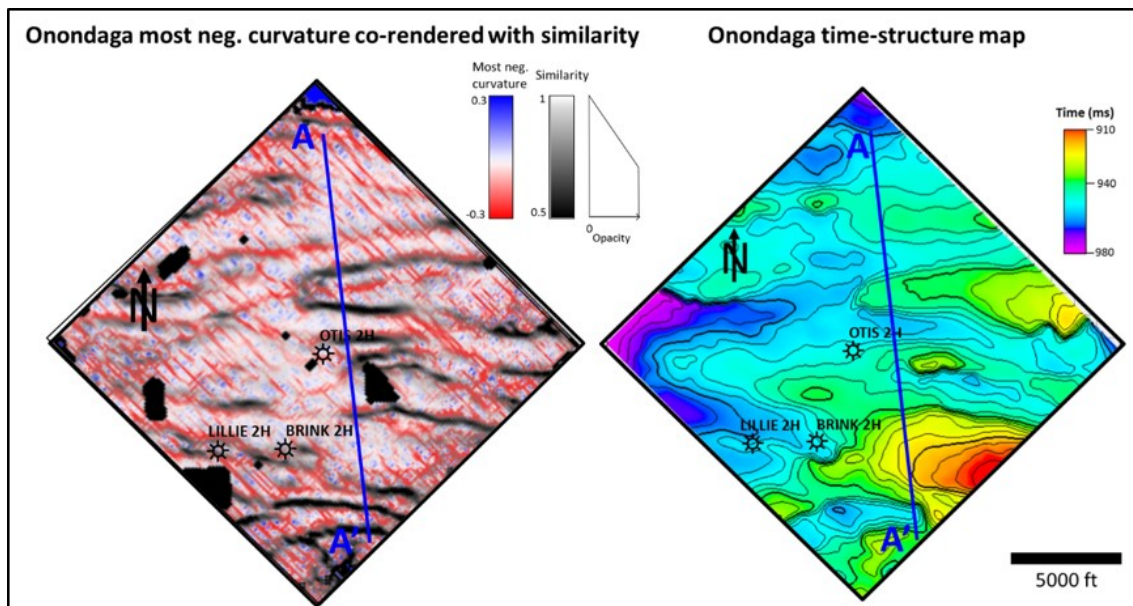


Figure 3.6: Comparison between the most negative curvature co-rendered with similarity extracted at the Onondaga top, and the Onondaga time-structure map. E-W trending faults are easily depicted in the curvature and similarity extractions. The most negative curvature highlights the downthrown side of the faults. The NW-SE lines (parallel to the crossline direction) showing in the curvature are acquisition footprint.

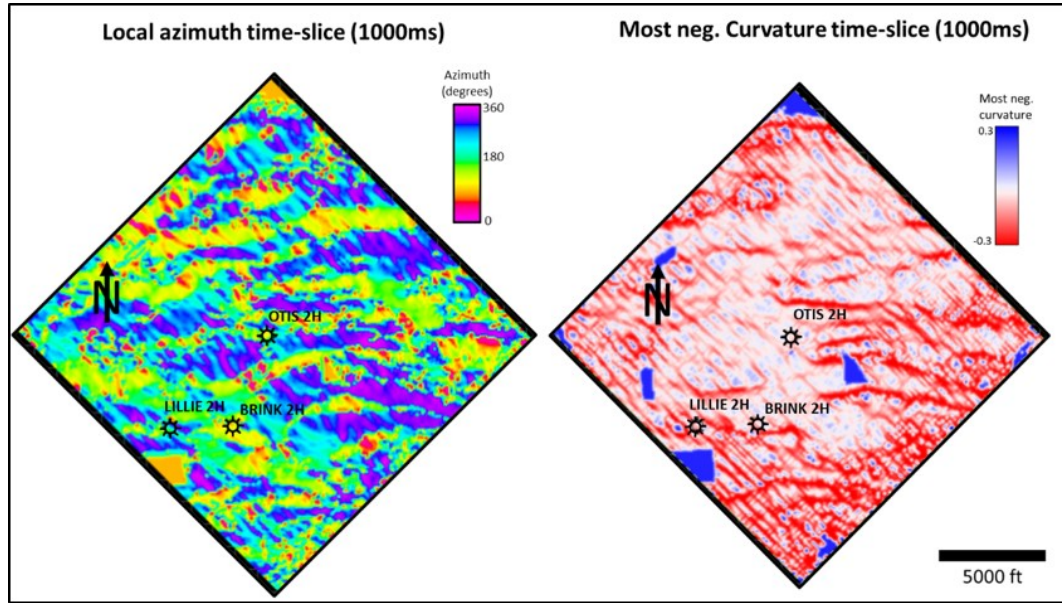


Figure 3.7: Comparison between the local azimuth and most negative curvature time-slices at 1000ms, which corresponds to approximately the middle of the Marcellus interval. The local azimuth attribute highlights small east-west and southeast-northwest directions. Both attributes are affected by acquisition footprint.

## 3.2 PP and PS joint interpretation

The PS seismic interpretation is conducted in a similar way as the PP effort. For the well tie, the wavelet was statistically extracted from the seismic, since the software does not allow the extraction of a wavelet using the reflectivity estimated from the well-logs for PS data because there is no mode-conversion at zero-offset. The statistical wavelet was extracted in a 600 ms window that includes the reservoir (see Table 3.2 to check the wavelet-extraction parameters), and a constant zero-phase

was assigned. The comparison between the final PP and PS wavelets and their corresponding frequency spectra are seen in Figure 3.8. The PP and PS data show a relatively similar frequency spectrum, with dominant frequencies around 30 Hz and 25 Hz, respectively. The PS volume has higher peak frequency than the PP volume.

Extraction parameters	PS wavelet
Window length	600 ms
Wavelet length	200 ms
Taper length	25 ms
Sample rate	2 ms

Table 3.2: Parameters for the PS statistical wavelet extraction at the OTIS 2H well.

Figure 3.9 shows the PS well-to-seismic tie for the OTIS 2H well. From left to right, shear-wave sonic, density, and shear-wave impedance logs are shown. Since there is no mode-conversion at zero-offset, the PS synthetics (blue traces) are generated at an incident angle of  $20^\circ$  to approximate zero-offset. An inline going through the well is also shown on the right, with the  $20^\circ$  incidence-angle synthetic seismogram inserted at the well location to compare the match between the synthetic and the real seismic data. As for the PP data, there is an excellent correlation between the converted-wave seismic data and the synthetic seismogram, with a higher correlation coefficient (0.85) than the PP well tie (0.83). After the PS seismic well-tie, the horizons already defined in the PP seismic were picked in the PS volume.

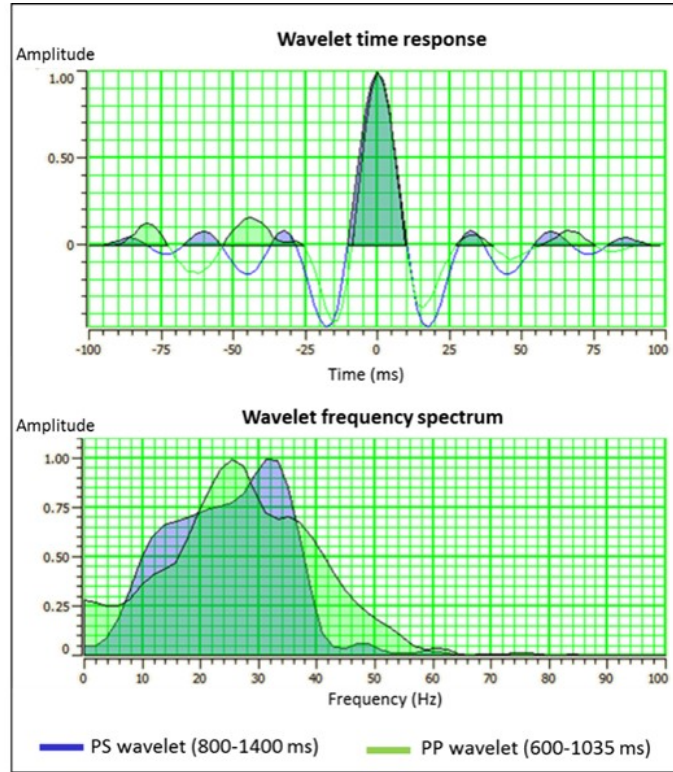


Figure 3.8: PP (green) and PS (blue) full wavelets and their corresponding frequency spectrum. The extractions were performed in a window from 800 to 1400 ms for the PS volume and from 600 to 1035 ms for the PP volume. The PS frequency spectrum shows a higher peak frequency than the PP spectrum.

The PS seismic resolution ( $\lambda/4$ ) is estimated in the same way as the PP data, using the S-wave average RMS velocity calculated from the dipole sonic interval velocities at the reservoir level (7,500 ft/s) and a dominant frequency of 28 Hz. The vertical-resolution for the PS data corresponds to approximately 66 ft, and is higher than the PP seismic resolution (102 ft). This can be observed in the PS wedge model for 20° incidence-angle in Figure 3.10. As the PP case, the Lower Marcellus thickness

is varied from 0 to 500 ft. As expected, the same phase-shift is observed in the PS wedge model.

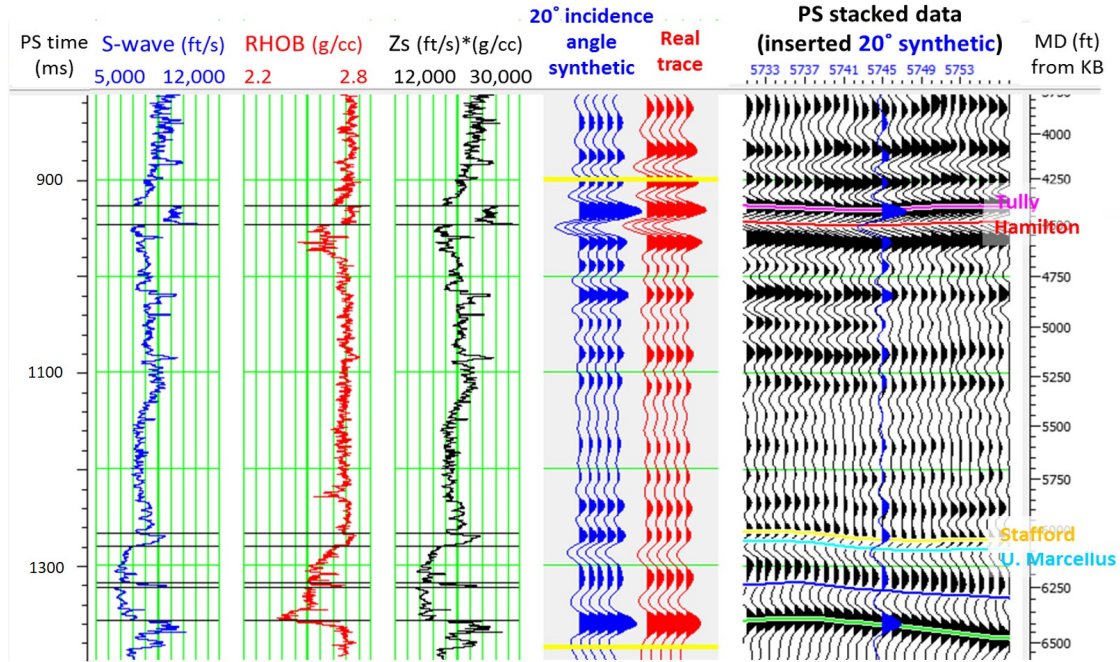


Figure 3.9: PS data well tie for the Otis 2H well. From left to right, S-wave sonic, density (RHOB) and S-impedance (Zs) logs, the 20° incidence-angle synthetic seismogram (blue traces), the real trace extracted from the well location (red traces), and an inline going through the well with the synthetic inserted at the well location. The yellow lines indicate the correlation window.

When comparing the PP and PS1 vertical sections (Figure 3.11), one can note that the major faults are more evident in the PS section, since their throw is more pronounced than in the PP data perhaps because of the longer travel-times of the

converted-wave data. The occurrence of these folds could be significant for well placing, taking into account that anticline or monocline folds might be more fractured than synclines due to the stress that a bed undergoes while folding, hence the importance of a joint interpretation of both PP and PS data. Some smaller faults that are visible in the PP section are not observable in the PS data. The PS1 section converted to PP time is also seen in Figure 3.12. The details on the registration process between PP and PS seismic to convert the PS seismic to PP time is detailed in Chapter 4. The dotted horizons in the PS1 seismic are the ones previously interpreted in the PP seismic. Note the excellent match between the location of the horizons and the actual events in the PS seismic.

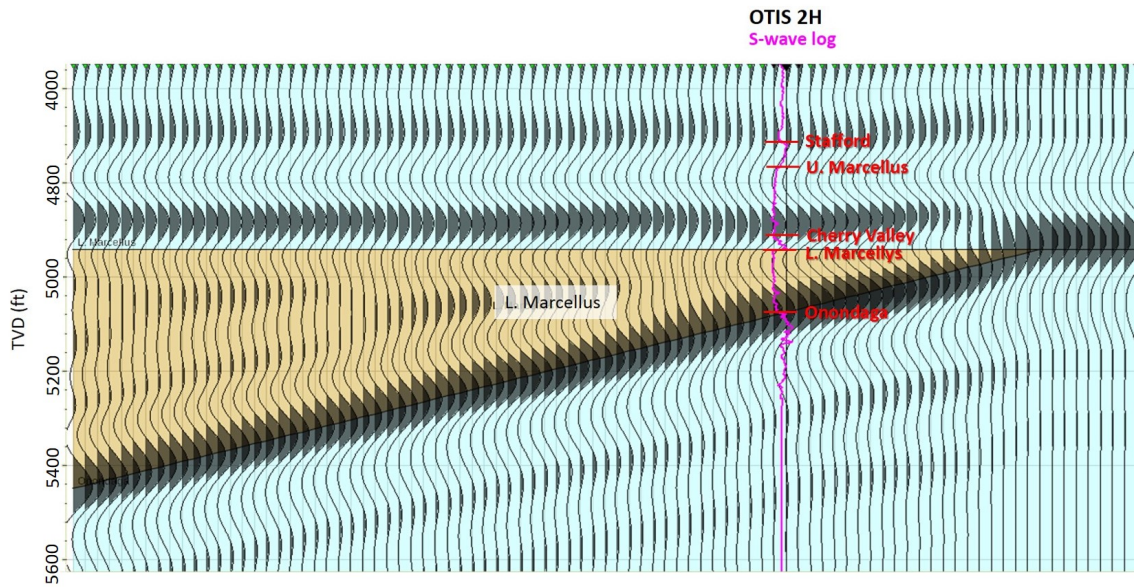


Figure 3.10: 20° PS wedge model generated using the PS extracted wavelet. The Lower Marcellus (golden color wedge) thickness is varied from 0 (right) to 500 ft (left). The OTIS 2H S-wave log is inserted at the real Lower Marcellus thickness (130 ft). The thin Stafford limestone (62 ft thick) causes a 90° phase-shift in the resulting waveform. At 130 ft thick, we are above one-half of the dominant period of the wavelet (peak-to-through time), which corresponds to Widess vertical-resolution limit.

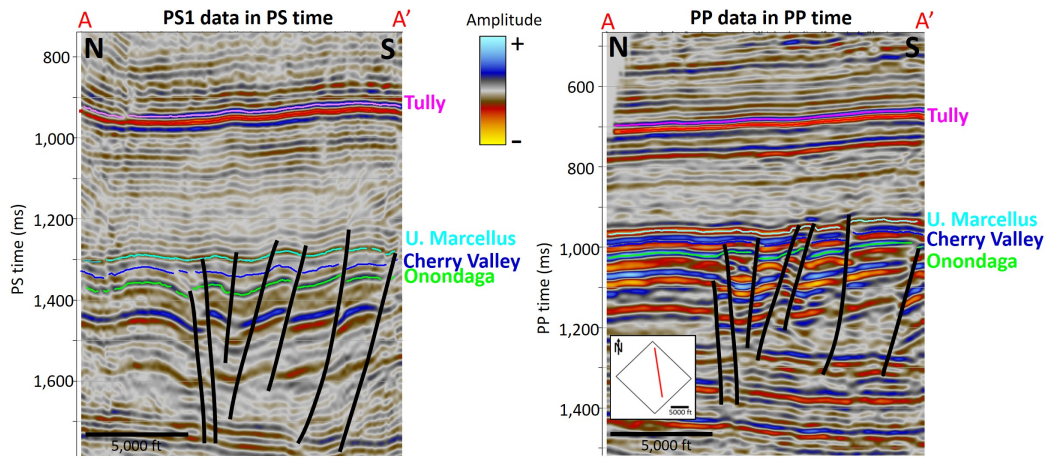


Figure 3.11: Comparison between the PS1 data in PS time and the PP data in PP time. Major faults are more evident in the PS section, however, some smaller faults that are visible in the PP section are not observable on the PS data.

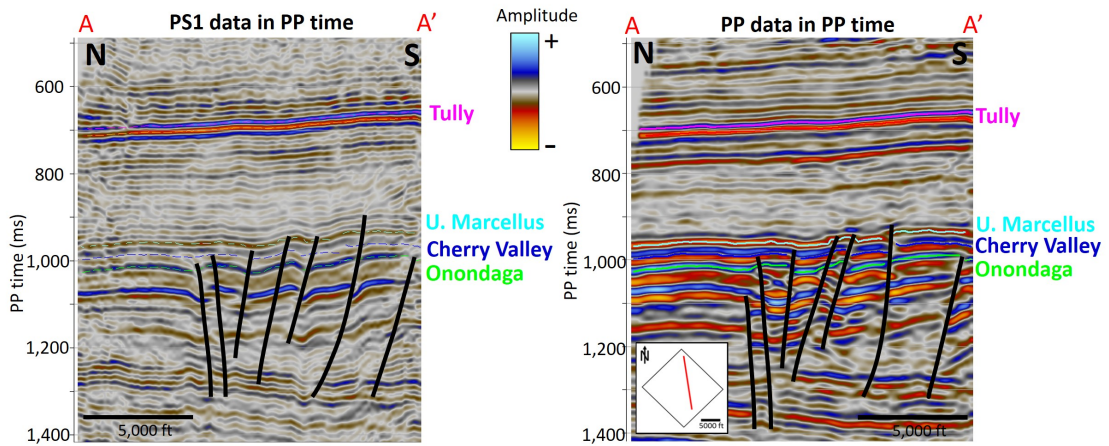


Figure 3.12: Comparison between the PS1 data in PP time and the PP data in PP time. Dotted horizons in the PS1 data correspond to the horizons interpreted in the PP volume.

The main east-west structural trends interpreted in the PP data tend to agree with the converted-wave interpretation. Figure 3.13 shows the comparison between the time-structure maps of the Upper Marcellus top and the Onondaga top (base of the Marcellus interval) interpreted in the PP and PS1 seismic. The Onondaga PS time-structure map shows more detail than the PP.

Using the PP and PS volumes in their native times, isochrons were generated for the Upper and Lower Marcellus (Figure 3.14). Both PP and PS maps have the same time-thickness color scale, and the contour interval is 4 ms. The Upper Marcellus interval shows an average time-thickness of around 35 ms in the PP volume (3.14a) and 45 ms in the PS volume (3.14b). Both maps show that the east-west Valley features (downthrow side of the faults) show a slight increase in time thickness. The difference in time thickness is more evident in the Upper Marcellus PS isochron. The Lower Marcellus interval shows a relatively constant time thickness of around 32 ms for the PP volume (Figure 3.14c) and 35 ms for the PS volume (Figure 3.14d). However, the east-west Valley features also show a slight increase in time thickness.

Interval  $V_p/V_s$  maps were generated for both units using the previously calculated isochrons by taking their ratio from the same interpreted horizons to generate  $V_p/V_s$  values. In this case,  $V_p/V_s = 2(T_{PS}/T_{PP}) - 1$ , where  $T_{PS}$  and  $T_{PP}$  are the corresponding PS and PP isochrons (Stewart et al., 2002). In both Upper and Lower Marcellus interval  $V_p/V_s$  maps (Figures 3.15a and 3.15b) the thicker east-west Valley features also exhibit high interval  $V_p/V_s$  values.

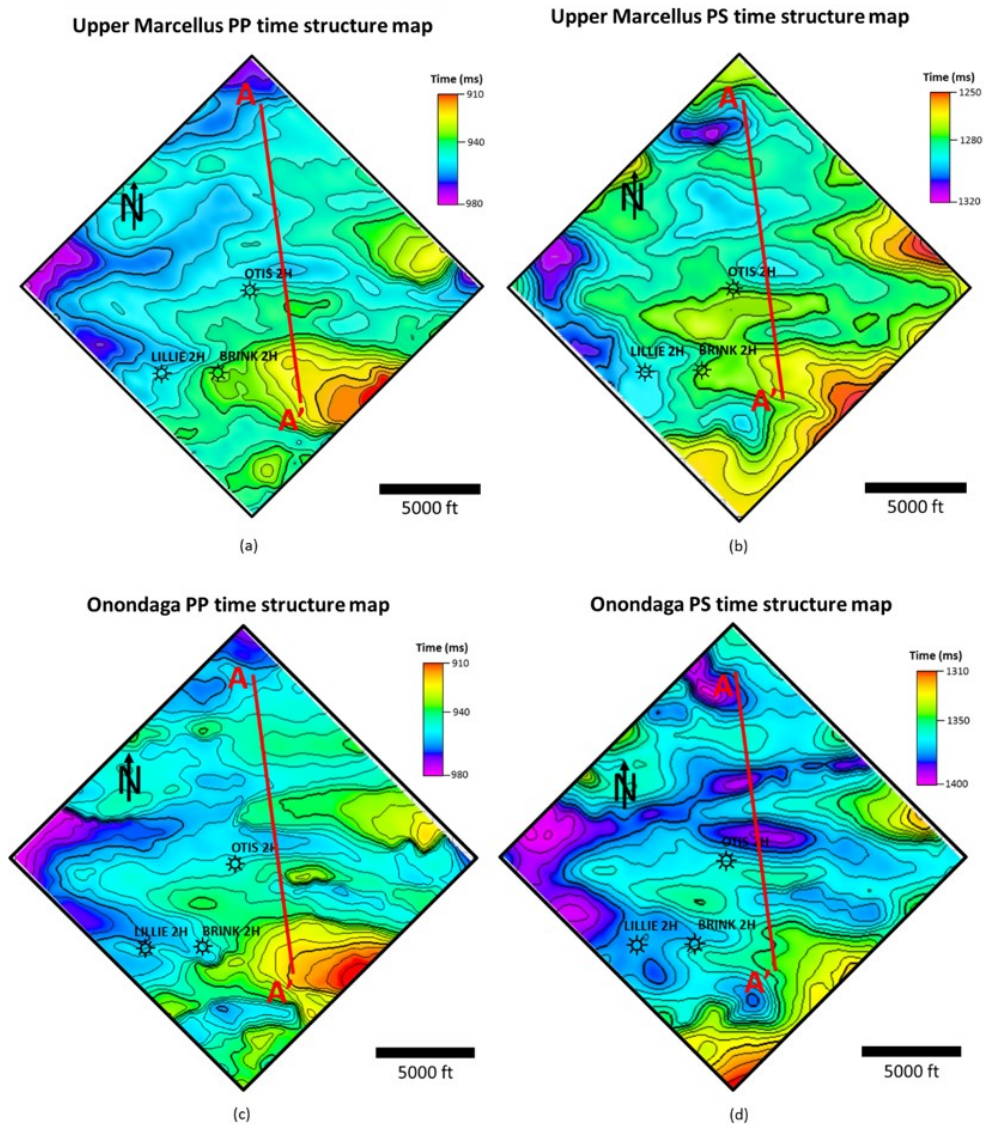


Figure 3.13: Comparison between the Upper Marcellus PP (a) and PS (b) time-structure maps and the Onondaga PP (c) and PS (d) time-structure maps. The main east-west structural trends interpreted in the PP data tend to agree with the converted-wave interpretation. The PS time-structure maps show higher detail than the PP time-structure maps.

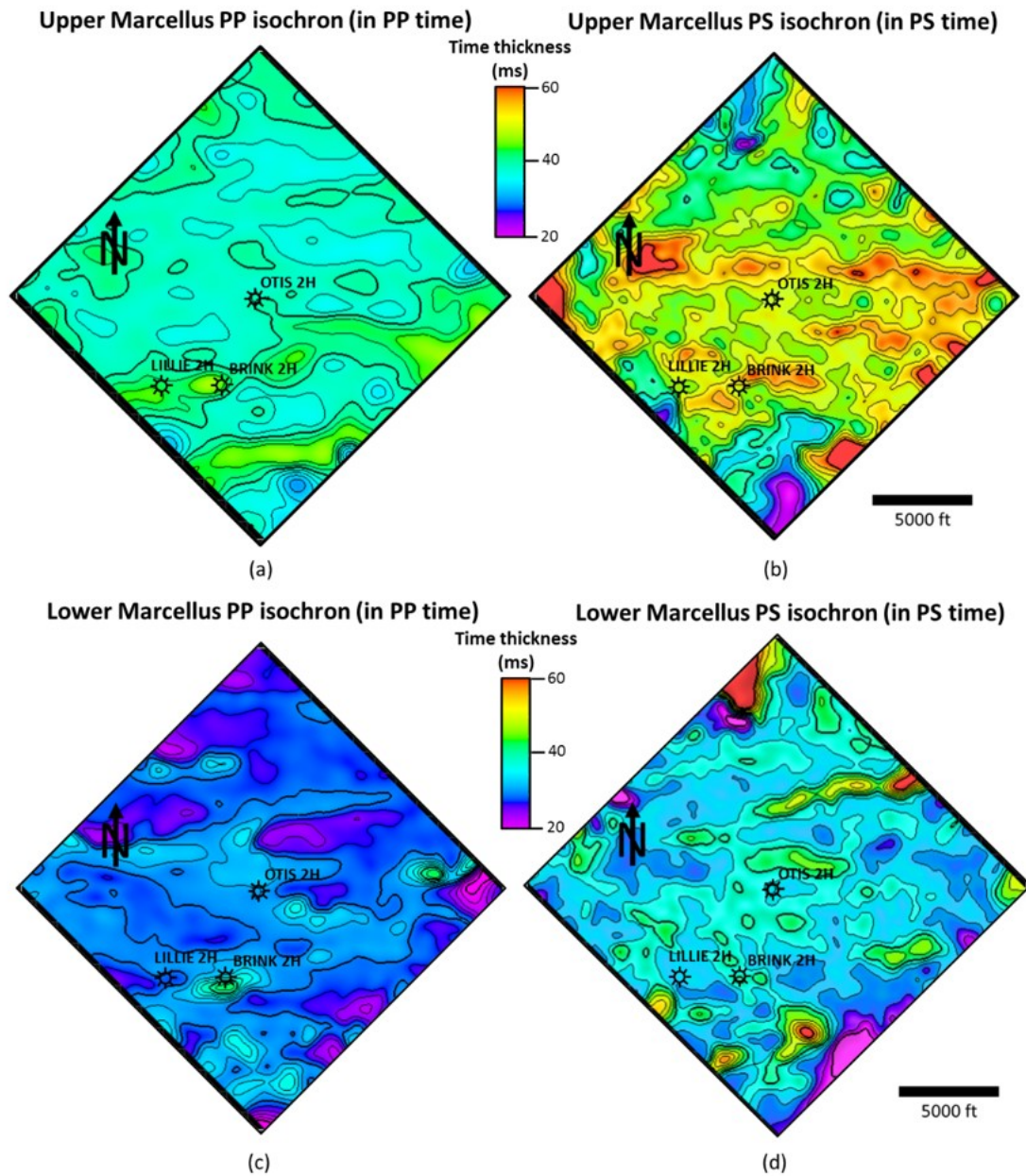


Figure 3.14: Comparison between the Upper Marcellus PP (a) and PS (b) isochrons and the Lower Marcellus PP (c) and PS (d) isochrons. The east-west valley features (downthrown side of the faults) show the highest time-thickness.

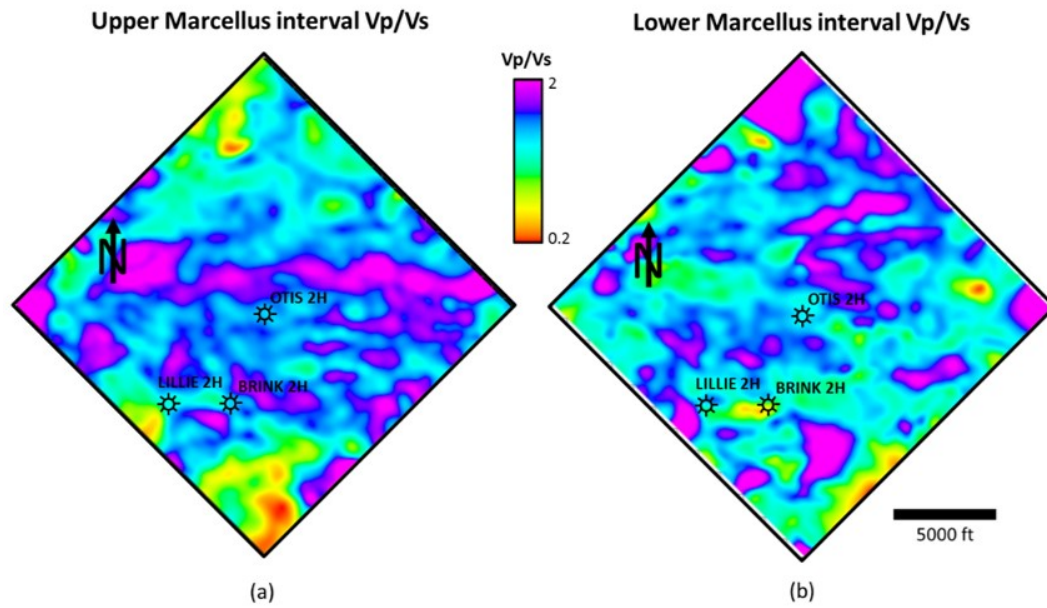


Figure 3.15: Interval  $V_p/V_s$  maps for the Upper (a) and Lower Marcellus (b). These maps were generated for both units using the previously calculated isochrons by taking their ratio from the same interpreted horizons. The thicker east-west Valley features also exhibit the highest interval  $V_p/V_s$  values.

# Chapter 4

## Seismic Inversion

As shown in Chapter 2, density is the rock property that best discriminates high TOC areas. Hence, a joint PP-PS inversion will be conducted to estimate P-impedance, S-impedance, density, and  $V_p/V_s$ .

Compressional and shear wave impedances can be estimated with P-wave data through simultaneous inversion of P-wave pre-stack gathers. This is the most common procedure used in the industry. However, its main disadvantage is that it is based on AVO approximations since no shear-wave information is directly measured in P-wave data. Additionally, density estimations through simultaneous P-wave inversions are often very sensitive to noise and the limited angle range found in many surveys (Russell, 2014). When multicomponent data are available, both P-wave and PS-wave modes can be inverted together, either in the pre-stack or post-stack domain, to obtain P-impedance, S-impedance, and density. Converted waves have

the advantage that their response only depends on contrasts of shear velocity and density. Gray (2003) showed that P-S data contains information about the shear impedance contrast up to incident angles of 25 degrees. Hence, the density information dominates at larger angles. Therefore, the addition of PS information can make the density inversion more stable.

The inversion scheme to be used in this work is a model-based linearized inversion. It has three main assumptions (Russell, 2014):

1. The linearized approximation for reflectivity holds.
2. PP and PS reflectivity as a function of angle can be given by the Aki-Richards linearized equations.
3. The background trend can be described by a linear relationship between the logarithm of P-impedance and both S-impedance and density. The algorithm tries to solve for deviations away from a linear fit in logarithmic space (Hampson and Russell, 2013).

The inversion method estimates the P, S and density reflectivities ( $R_P$ ,  $R_S$  and  $R_D$ ) through a linearized inversion of the modified Aki-Richards linear approximations for the angle dependent PP and PS reflection coefficients  $R_{PP(\vartheta)}$  and  $R_{PS(\vartheta)}$  (Russell et al., 2005; Russell, 2014):

$$R_{PP(\vartheta)} = c_1 R_P + c_2 R_S + c_3 R_D \quad (4.1)$$

$$R_{PS(\vartheta)} = c_4 R_S + c_5 R_D \quad (4.2)$$

$$R_P = \frac{1}{2} \left( \frac{\Delta V_p}{V_p} + \frac{\Delta \rho}{\rho} \right) \quad (4.3)$$

$$R_S = \frac{1}{2} \left( \frac{\Delta V_s}{V_s} + \frac{\Delta \rho}{\rho} \right) \quad (4.4)$$

$$R_D = \frac{\Delta \rho}{\rho} \quad (4.5)$$

Coefficients  $c_1$  to  $c_5$  are functions of the angle of incidence, angle of reflection, and the  $V_p/V_s$  ratio. The reader is referred to Hampson et al., (2005) for a complete review of this inversion method.

Due to the band-limited characteristics of the seismic data, a low-frequency impedance model is needed to avoid instability issues. This low-frequency model is used to initialize the inversion process and then iterate towards a solution (Hampson and Russell, 2013).

The multicomponent joint inversion workflow is seen schematically in Figure 4.1.

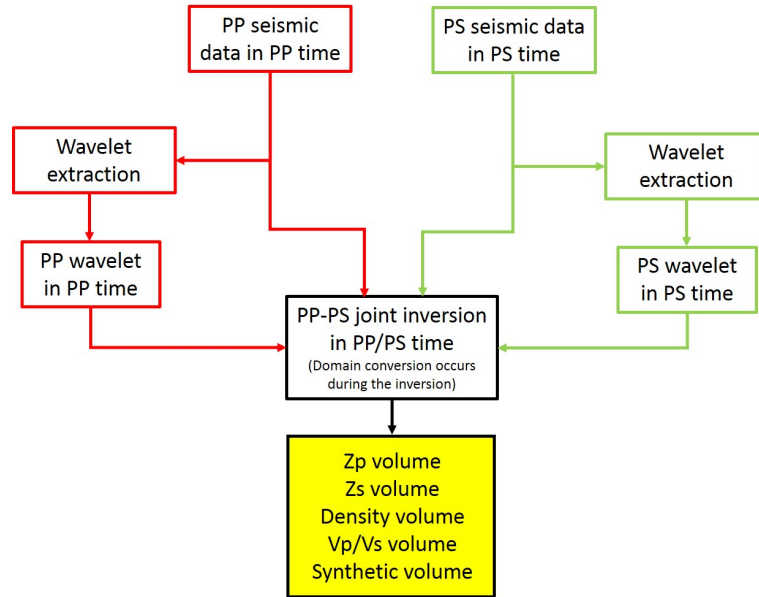


Figure 4.1: PP-PS joint inversion workflow. Modified from the Hampson-Russel PROMC manual.

As mentioned in Chapter 1, from the three available wells located inside the seismic survey, the OTIS 2H is the only one that is logged through the reservoir interval. LILLIE 2H and BRINK 2H are two gas wells that also produce from the Lower Marcellus interval and are located inside the survey. However, their logs reach a total depth of 5610 ft and 5540 ft, respectively, while the Upper Marcellus formation top is at 6075 ft. These two wells only have gamma-ray and density logs, hence the density logs are used as blind wells to validate the density inversion.

The first and one of the most important steps before attempting to do any qualitative analysis is to achieve a good well-to-seismic tie. The extracted wavelets and PP and PS well-ties for the OTIS 2H well are shown in Chapter 3.

## 4.1 PP-PS registration

Reflections from different wave modes originate from a common depth, but the differences in propagation velocity for the different modes cause the reflections to occur at different times. Since the joint inversion process requires the alignment of the events in both PP and PS volumes, the PS volume needs to be accurately registered to PP time. This domain conversion is achieved at the well location using a  $V_p/V_s$  value generated from the P and S-sonic logs after both logs are tied to the PP and PS volumes that will be used in the inversion, giving the correct time-depth curves for both logs. Figure 4.2 shows the comparison between the  $V_p/V_s$  values obtained from the P and S-wave sonic logs (blue), from the well-to-seismic tie (red), and from the multicomponent zero-offset VSP (black) acquired at the OTIS 2H well. The  $V_p/V_s$  from the well-to-seismic tie shows slightly lower values than the  $V_p/V_s$  calculated from the well-logs (8.5 % for the Hamilton shale and 6.45 % for the Marcellus interval). This difference is related to velocity dispersion and seismic wave attenuation.

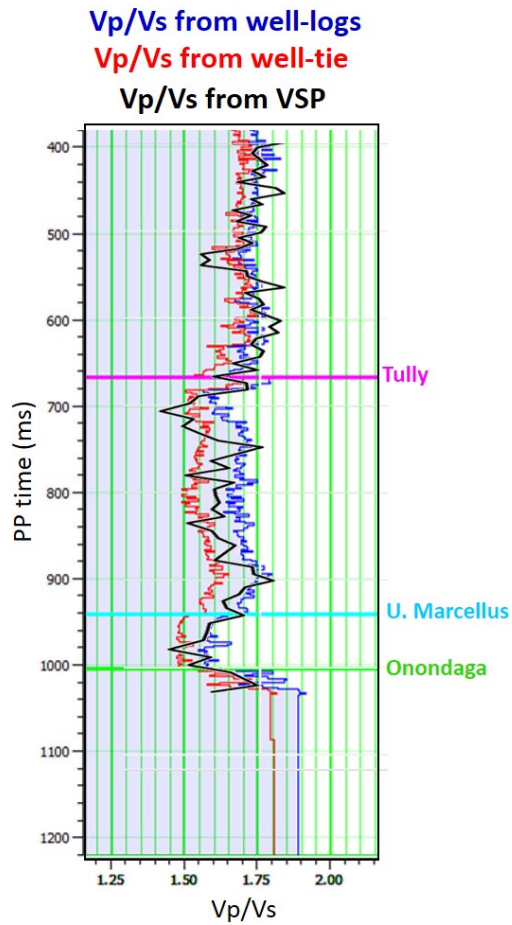


Figure 4.2: Comparison between the  $V_p/V_s$  calculated from the dipole sonic log (blue), from the well-to-seismic tie (red) and the zero-offset VSP (black) at the OTIS 2H well. The  $V_p/V_s$  from the well-to-seismic tie is in agreement with the  $V_p/V_s$  from the VSP and shows slightly lower values than the  $V_p/V_s$  calculated from the well-logs (8.5% for the Hamilton shale and 6.45% for the Marcellus interval).

PP and PS horizon-matching is used to extrapolate the  $V_p/V_s$  relation through the entire seismic survey. This is, picked horizons that correspond to the same event

are matched and the  $V_p/V_s$  relation is calculated at each location using interval travel-times as:

$$\frac{V_p}{V_s} = \frac{2\Delta T_{PS}}{2\Delta T_{PP}} - 1 \quad (4.6)$$

Where  $\Delta T_{PP}$  and  $\Delta T_{PS}$  are the time-thicknesses between the interpreted horizons on the PP and PS stacked volumes, respectively. Varga (2009) states that a limitation of this method is that it uses an average over the time-thickness interval to express the thickness of a depth interval in terms of P and S-wave travel-times.

Commonly, the PP data is filtered to the frequency of the PS data to reduce the uncertainty on horizon picking. However, correlative events were easily picked in both volumes without the need of applying any filter because their bandwidth is very similar (Figure 4.3).

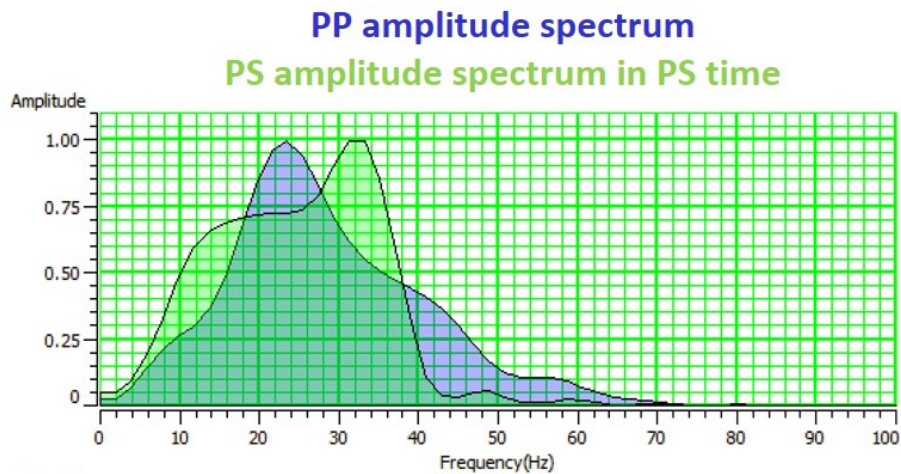


Figure 4.3: Comparison between the PP (green) and PS (blue) frequency spectra. Note that both PP and PS bandwidths are very similar.

The Tully, Upper Marcellus, and Onondaga horizons picked in both volumes were used for the horizon-matching process (see Figure 4.2). The rest of the picked horizons (Cherry Valley, Stafford, and Hamilton) were not used because small picking errors in horizons that are very close together translate to large errors in the estimated  $V_p/V_s$ . Figure 4.4 shows a 3D view of two intersecting sections of PP and PS data both in PP time, after the registration process. Red arrows indicate the location of the Tully, Upper Marcellus, and Onondaga events. Note the good correlation between the two volumes.

The apparent frequency content of the PS data increases even more when converted to PP time (see Figure 4.5). This indicates that the PS volume will not only incorporate measured shear-wave information into the analysis but might also help increase resolution in the joint-inversion results.

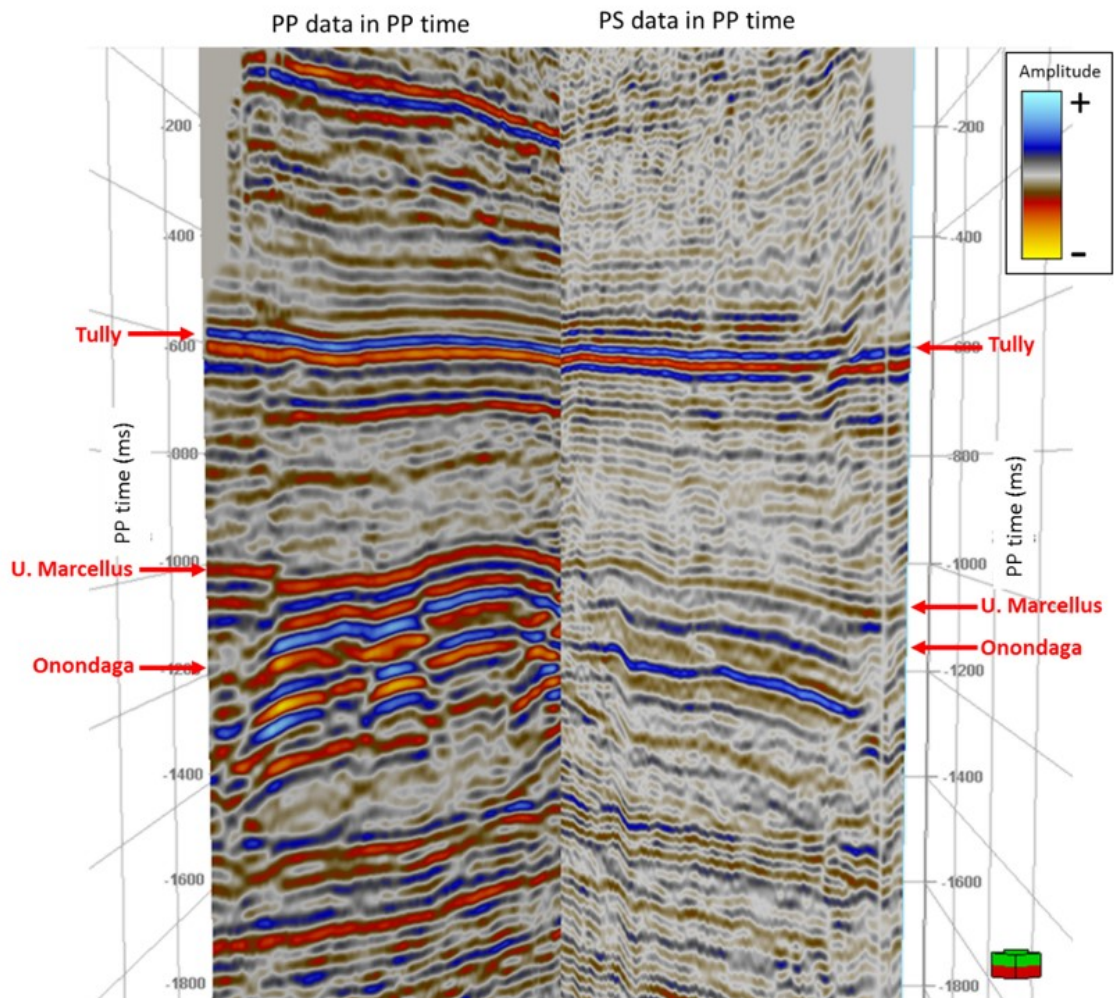


Figure 4.4: 3D view showing the comparison between the PP (left) and PS (right) volumes after the registration. Both volumes are in PP time domain. Red arrows indicate the location of the Tully, Upper Marcellus, and Onondaga events. Note the good correlation between the two volumes, which is indicative of a correct registration.

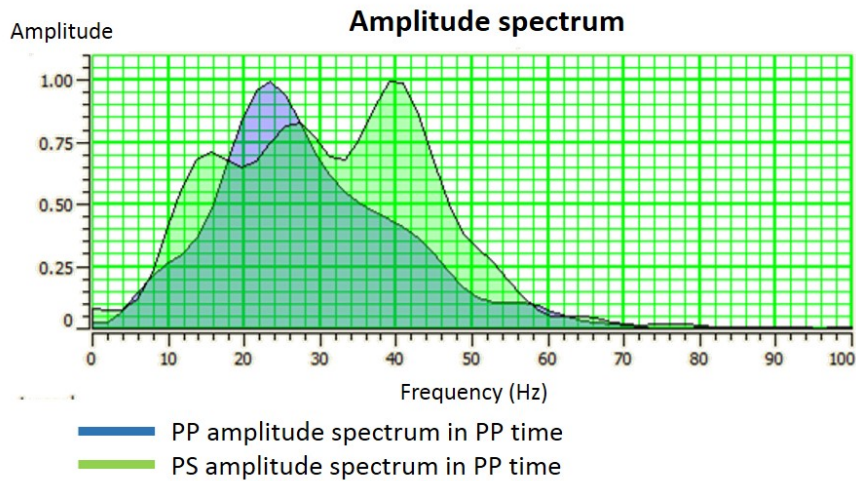


Figure 4.5: Comparison between frequency spectra from the PP seismic data in PP time (blue) and the PS seismic data converted to PP time (green). Note the increase in both bandwidth and peak frequency of the PS data when converted to PP time.

## 4.2 PP-PS post-stack joint inversion

To constraint the inversion and overcome instability issues in the inversion process, low-frequency models are used to initiate the inversion process. The P-wave velocity and density low-frequency models are obtained by extrapolating the well-logs using the Tully, Upper Marcellus, and Onondaga horizons as a guide. Since only one well can be used in the inversion, the post-migration seismic velocities were co-Kriged with the P-wave velocity to generate the P-wave initial model. However, since the seismic velocities are very low-frequency, and there are not big structural variations in the seismic data, there was no difference in the velocity models or in the inversion

results derived using only the P-wave log and using both the P-wave log and the seismic velocities.

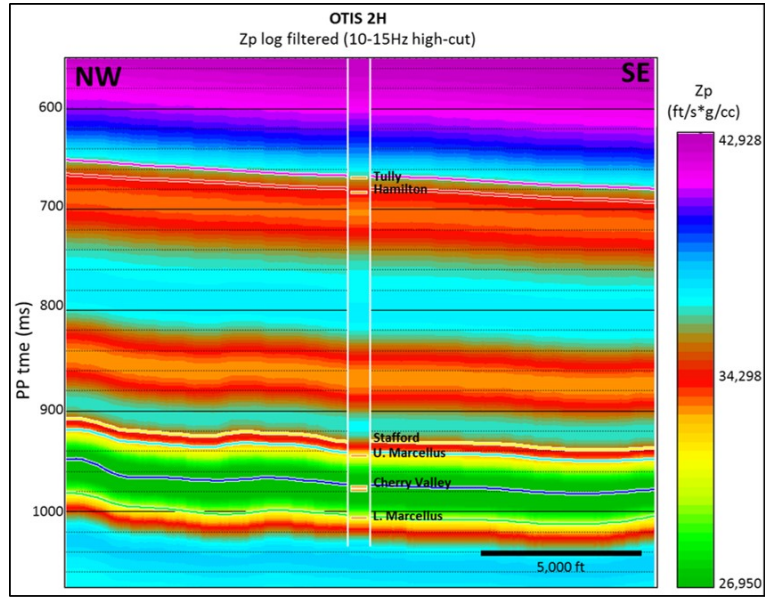
The S-impedance model is calculated using the  $V_p/V_s$  from the registration ( $V_p/V_s$  from the tied P and S-wave logs extrapolated by matching the horizons picked in both PP and PS volumes), the P-wave data to calculate the shear velocity and the density to finally calculate the impedance. The models were filtered using a 10-15 Hz high-cut filter since we only want to add the low-frequencies that are not present in the seismic data. Figures 4.6 and 4.7 show the P-impedance, S-impedance,  $V_p/V_s$  ratio and density low-frequency models used as input in the inversion. The inserted log at each profile corresponds to the matching well-log filtered to the frequency of the model. Note that the  $V_p/V_s$  model was not filtered.

An additional constraint was used to try to overcome the non-uniqueness of the inversion problem by using a background trend described by a linear relationship between the logarithm of P-impedance and both S-impedance and density (Russell, 2014):

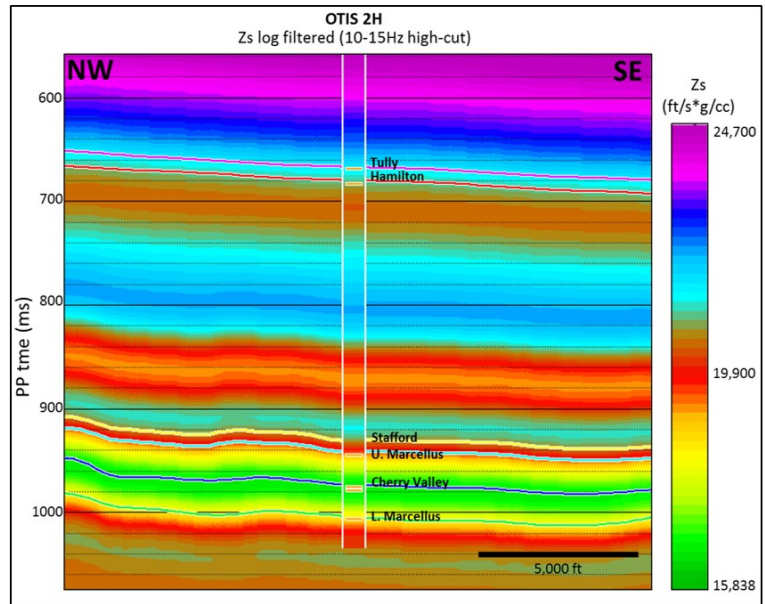
$$\ln(Z_s) = k \ln(Z_p) + k_c + \Delta \ln(Z_s) \quad (4.7)$$

and

$$\ln(Z_p) = m(Z_p) + m_c + \Delta \ln(\rho) \quad (4.8)$$

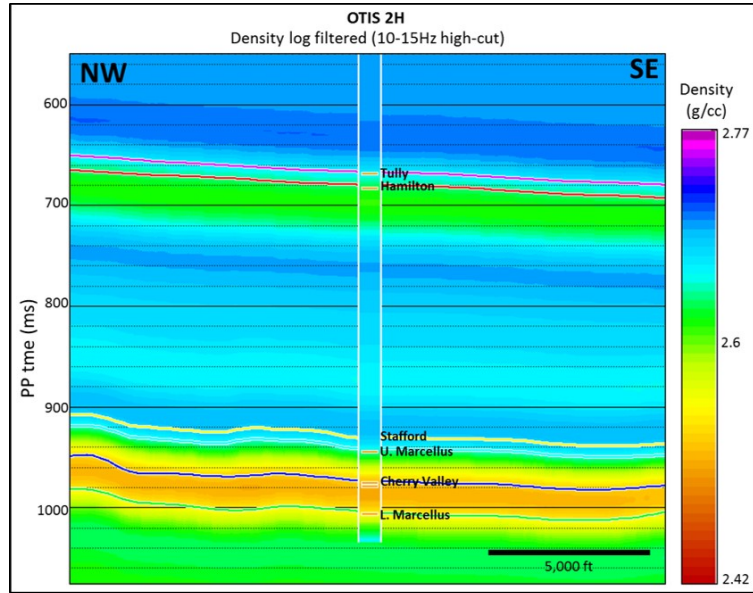


(a)

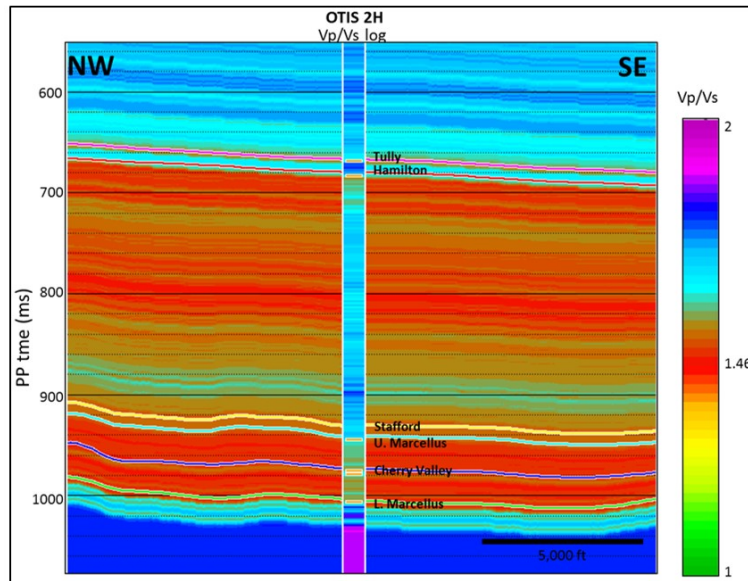


(b)

Figure 4.6: NW-SE sections of (a) P-impedance ( $Z_p$ ) and (b) S-impedance ( $Z_s$ ) low-frequency models going through the OTIS 2H well location.



(a)



(b)

Figure 4.7: NW-SE sections of (a) density and (b)  $V_p/V_s$  low-frequency models going through the OTIS 2H well location.

Where coefficients  $k$ ,  $k_c$ ,  $m$ , and  $m_c$  are linear-fitting parameters corresponding to the background trend calculated by cross-plotting the logarithms of the  $Z_p$ ,  $Z_s$ , and density log values.  $\Delta \ln(Z_s)$  and  $\Delta \ln(\rho)$  correspond to the deviations from the linear fit that the inversion tries to solve for, which are related to the non-water saturated rocks. Since only one well is used in the inversion, a more representative background trend is calculated using the four wells with measured dipole sonic. The coefficient values are seen in Table 4.1 and the cross-plots between the logarithms of (a) P-impedance and S-impedance and (b) P-impedance and density for the four wells are seen in Figure 4.8.

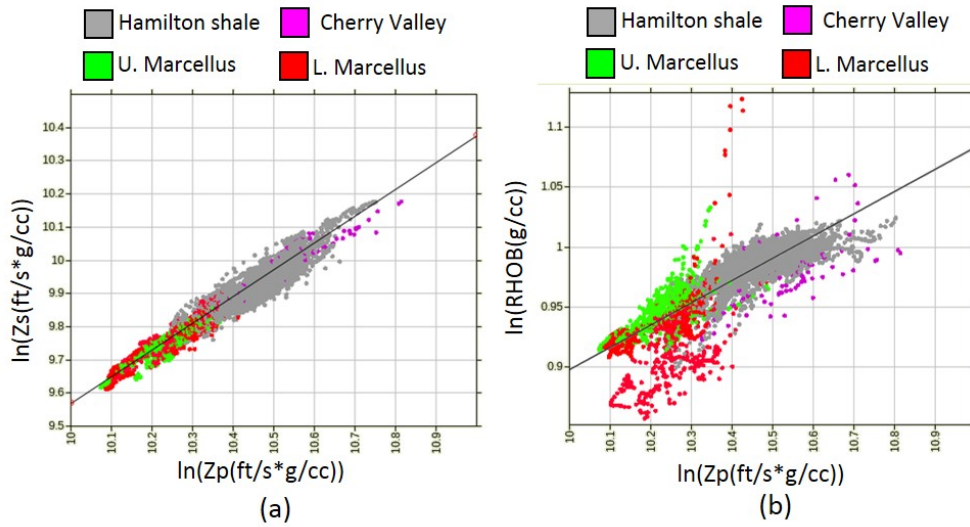


Figure 4.8: Cross-plots between the natural logarithm of P-impedance ( $\ln(Z_p)$ ) and S-impedance ( $\ln(Z_s)$ ) (a) and between the natural logarithm of P-impedance ( $\ln(Z_p)$ ) and density ( $\ln(\rho)$ ), colored by interval. The linear-regressions for both plots are the background models for the inversion. The coefficients for each regression are seen in Table 4.1

$m$	$k$	$k_c$	$m_c$
0.189866	0.910905	0.434333	-1.0132

Table 4.1: Background linear trend coefficients used in the PP-PS post stack joint inversion:  $\ln(Z_s) = 0.910905 \ln(Z_p) + 0.434333 + \Delta \ln(Z_s)$  and  $\ln(Z_p) = 0.189866(Z_p) + -1.0132 + \Delta \ln(\rho)$ .

The PP-PS post-stack joint inversion has as inputs the full-stacked volumes, assuming that the PP stack is equivalent to a PP angle-gather at zero degrees and that the PS stack is equivalent to a PS angle stack at 20 degrees. The value of 20 degrees was selected after correlating the PS stack traces near the well with synthetic traces generated at various angles.

The inversion results at the OTIS 2H well location is seen in Figure 4.9. The inversion window corresponds to 500 ms. The yellow horizontal lines indicate the top and base of the inversion

(from 700 to 1200 ms in PP time). The RMS error for each inverted property is calculated in the entire window. The initial model corresponds to the black curve, the well-logs filtered to the approximate seismic frequency plus low-frequency model band (0-0-40-50 Hz) are seen in blue, and the inverted logs are seen in red. There is an excellent agreement between the well-logs and the inversion results. Note that the RMS error between the S-impedance log and the inverted result is much lower than the RMS error of the P-impedance (821.4 and 1,670.48 ft/s\*g/cc, respectively). The density and V/Vs inverted results, which are usually noisy when using only P-wave data, show excellent correlations with the original logs. Even though the 50 ft thick low-density Hot Lower Marcellus is below seismic resolution, the density inversion is

picking up the low-density interval. Hence, it is feasible to use the inverted-density volume to map the high TOC interval at the Lower Marcellus.

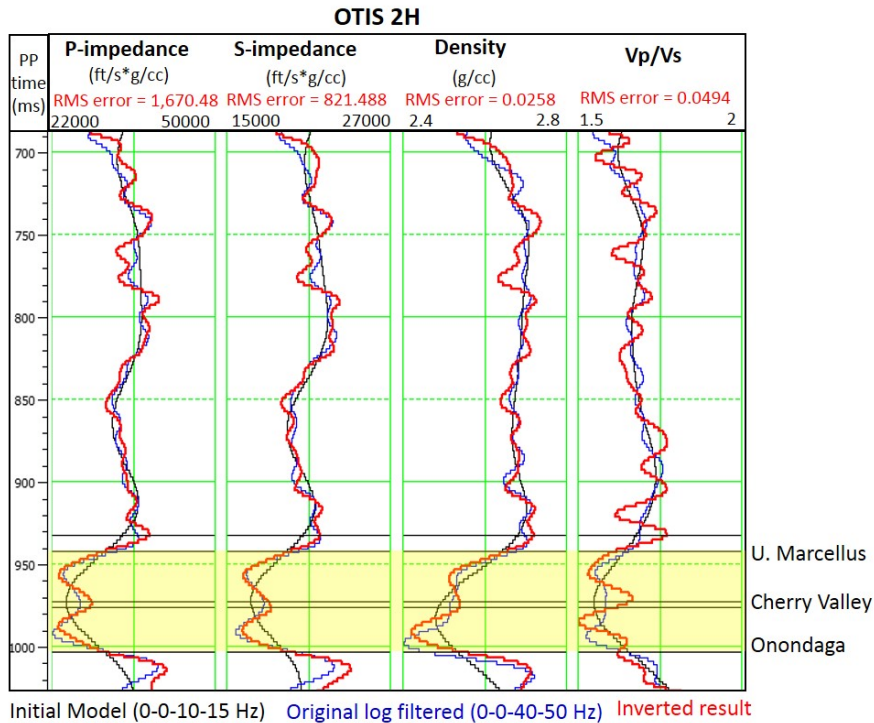


Figure 4.9: PP-PS post-stack joint-inversion results at the OTIS 2H well location. Black, blue, and red logs correspond to the initial models, the filtered logs (0-0-40-50 Hz), and the inverted result, respectively. The yellow polygon denotes the Marcellus interval. There is a very good correlation between the inversion results and the original logs.

The comparison between the PP and PS synthetic traces generated in the inversion and the original traces at the OTIS 2H well is seen in Figure 4.10, along with their corresponding error, that is, the difference between the synthetic and the

original trace. Figure 4.11 shows the difference between the PP seismic and the PP synthetic at an inline going through the well location. Note that the amplitude of the traces is almost zero, which means that the real seismic and the synthetic seismogram are almost identical.

A line going through the OTIS 2H well in Figures 4.12 and 4.13 shows the inverted  $Z_p$ ,  $Z_s$ , density, and  $V_p/V_s$  volumes.

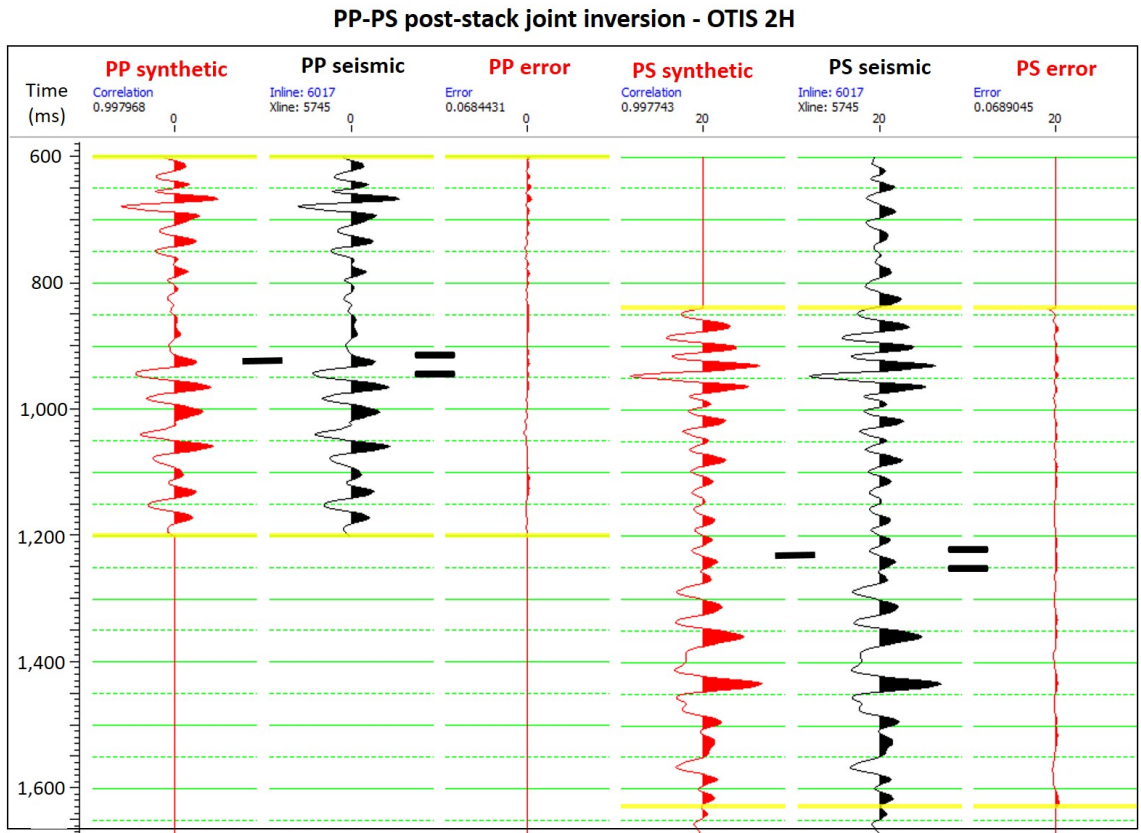


Figure 4.10: Comparison between the PP (left) and PS (right) synthetic traces generated in the inversion and the original traces at the OTIS 2H. The difference between the synthetics and the original traces corresponds to the error.

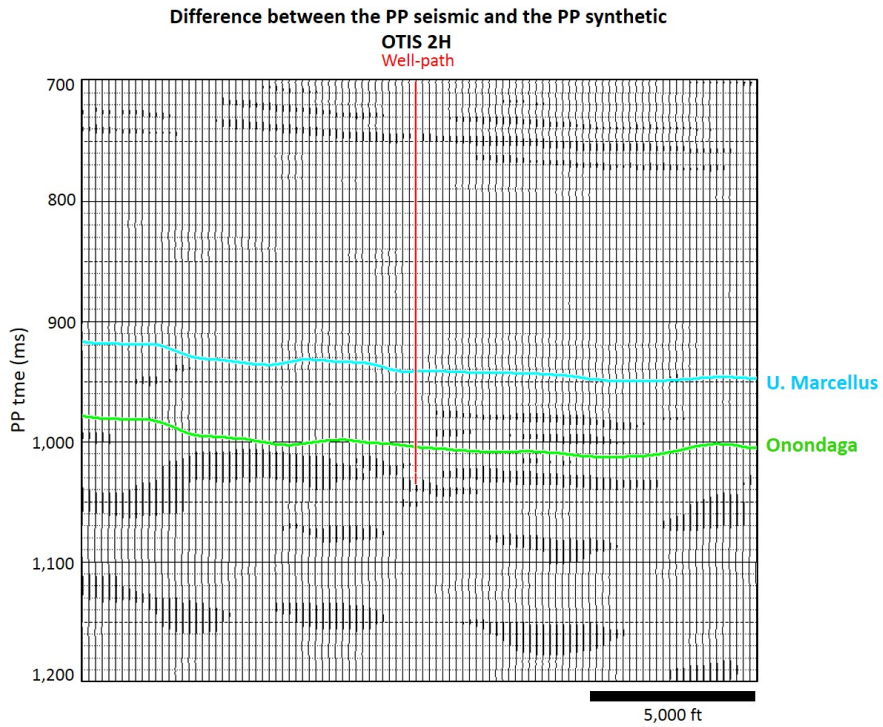


Figure 4.11: Difference between the PP seismic and the PP synthetic at an inline going through the well location. Note that the amplitude of the traces is almost zero, which means that the real seismic and the synthetic seismogram are almost identical.

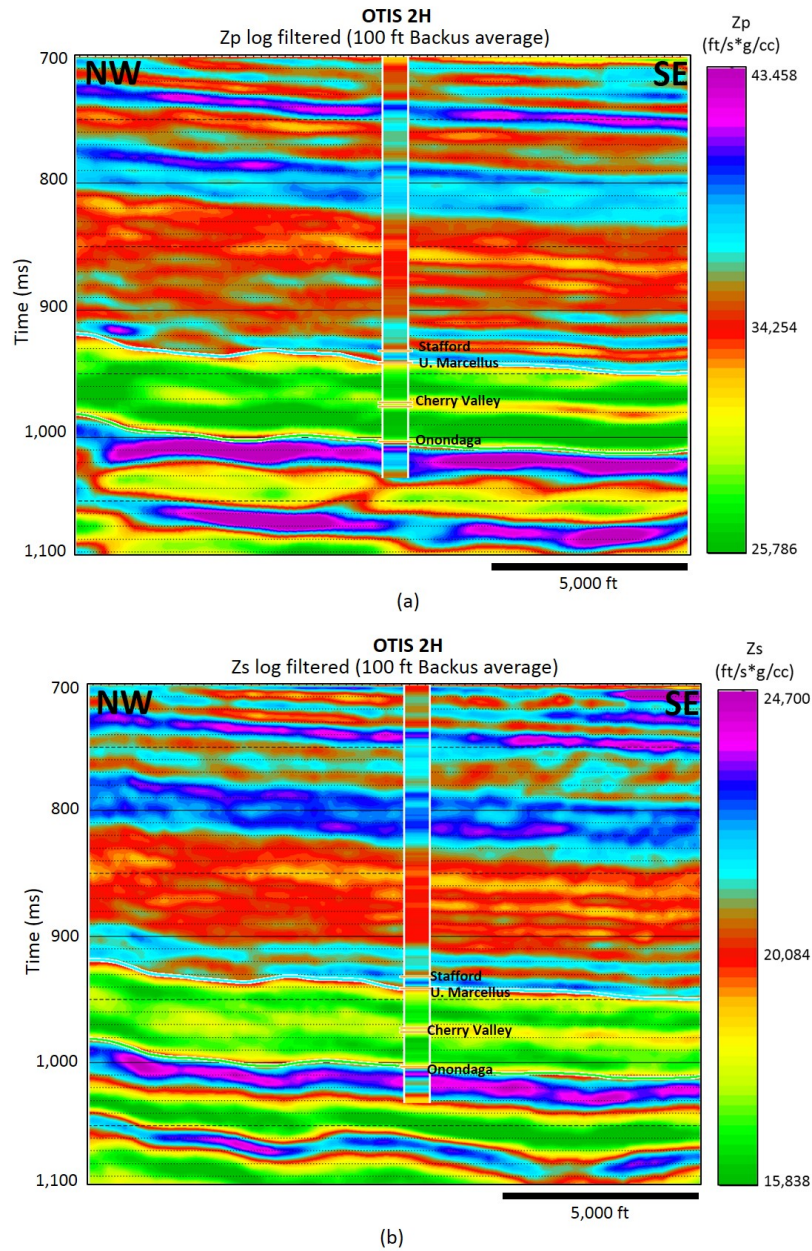


Figure 4.12: NE-SW line going through the OTIS 2H well and showing the P-impedance (a) and S-impedance (b) inverted results. The displayed logs are the P-impedance (a) and S-impedance (b) logs upscaled to the seismic frequency.

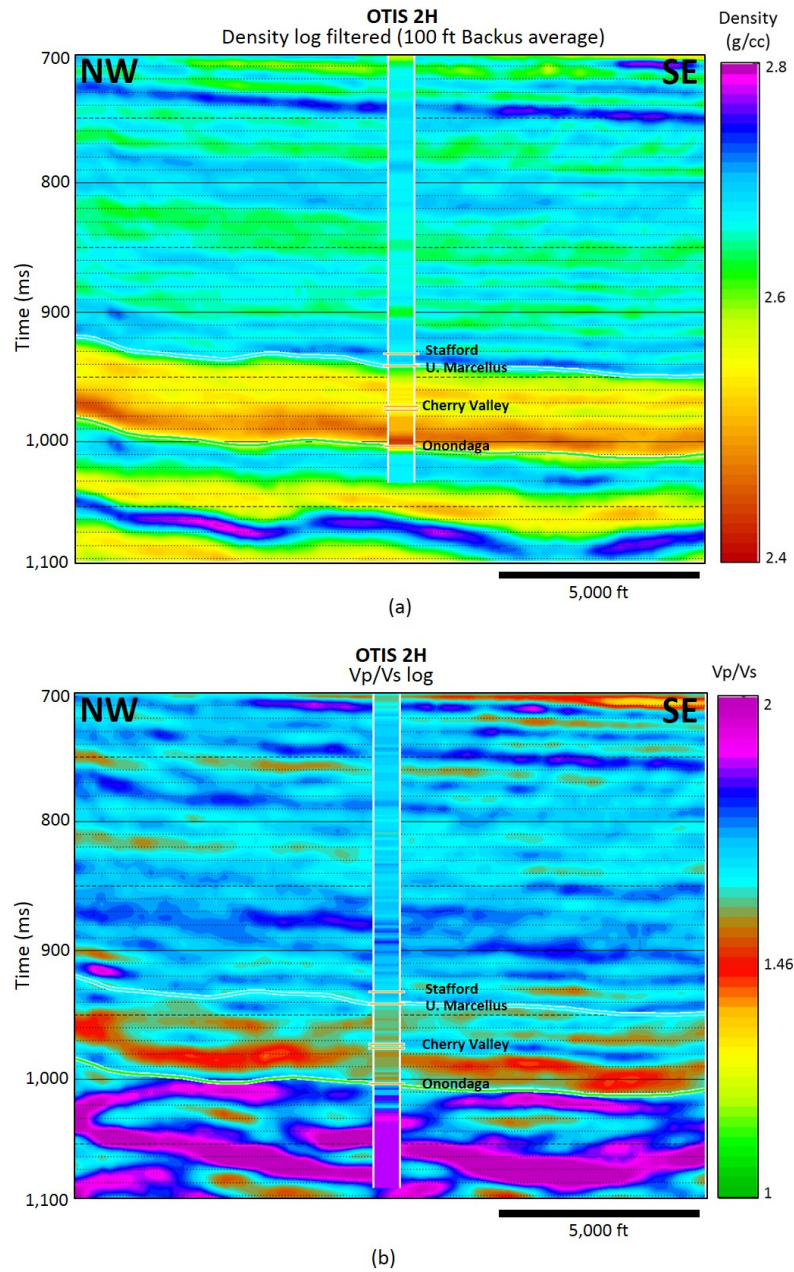


Figure 4.13: NE-SW line going through the OTIS 2H well and showing the density (a) and Vp/Vs (b) inverted results. The displayed logs are the density (a) and Vp/Vs (b) logs upscaled to the seismic frequency.

As previously mentioned, the LILLIE 2H and BRINK 2H wells are used to validate and QC the density-inverted volume. Figure 4.14 shows an arbitrary line of the inverted-density volume that goes through the three gas-producing wells that are located inside the seismic survey: LILLIE 2H, BRINK 2H, and OTIS 2H. The upscaled-density logs are displayed at each well location. Warm colors represent low-density values and cold colors high-density values. The inverted-density volume shows the same general trend and exhibits a good correlation with the LILLIE 2H density log (see Figure 4.15a). The BRINK 2H density log seems to show higher density values than the OTIS 2H and LILLIE 2H density logs for the whole section. The BRINK 2H density readings appear to be noisy and not very trustable. However, the general trend matches the inverted volume. Moreover, the Lower Marcellus shows low-density values that correlate to high TOC producing intervals at the location of the three gas-producing wells.

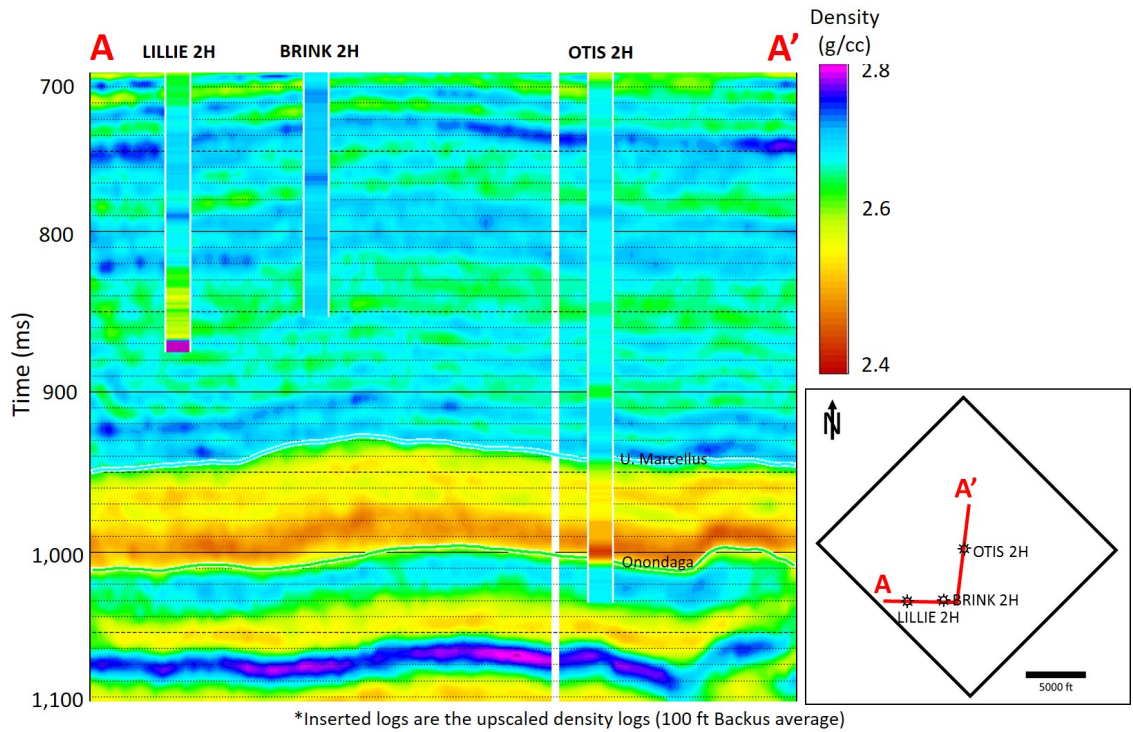
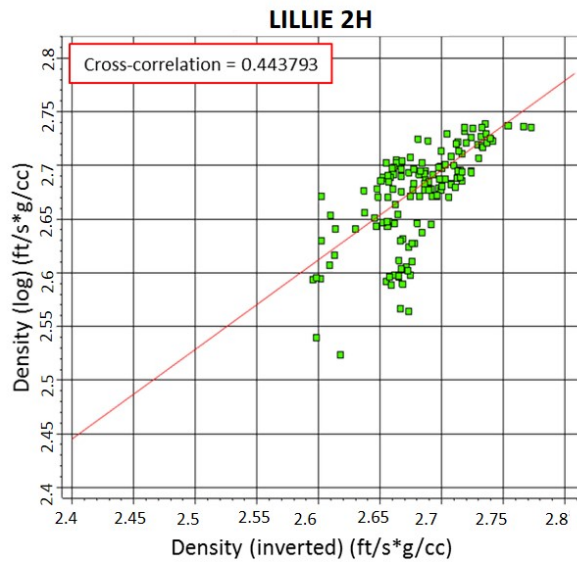
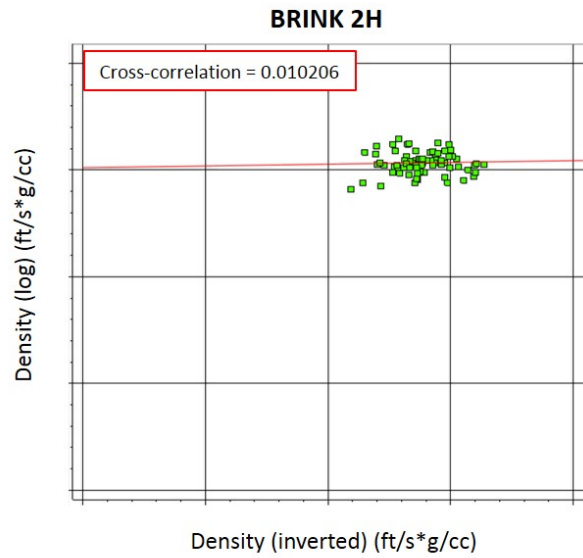


Figure 4.14: Arbitrary inverted-density volume line going through the three wells located inside the seismic survey: LILLIE 2H, BRINK 2H, and OTIS 2H. The density logs upscaled to the frequency of the seismic are displayed at each well location. The inverted-density volume shows the same general trend as the LILLIE 2H and BRINK 2H density logs, which were not included in the inversion.



(a)



(b)

Figure 4.15: Cross-plots showing the cross-correlation coefficients between the original density logs and inverted-density values at the LILLIE 2H and BRINK 2H wells.

### 4.3 Comparison between PP pre-stack inversion and PP-PS pre-stack joint inversion

In addition to the stacked PP and PS volumes, pre-stack PP and PS gathers are also available for this study. As shown in Chapter 1, both P-wave and converted-wave pre-stack gathers exhibit random high-frequency noise, low-frequency, low-velocity, and large-amplitude noise that seems to be un-suppressed ground roll and also multiples. These factors affect the seismic-reflection amplitudes, and consequently the AVO, so they should be taken care before the inversion process. In this sense, both PP and PS pre-stack gathers are conditioned according to workflows shown in Appendix A and B, respectively.

It is important to mention that the provided pre-stack gathers are part of an early and preliminary processing effort, and the migration velocities are not the same as the ones used for the PP and PS stacked volumes. Despite this, simultaneous PP pre-stack inversion and PP-PS pre-stack joint inversion are performed at the well location to compare their results, especially the density estimation.

Four angle-stacks are generated between P-wave incidence angles of 5 and 37° and one statistical zero-phase wavelet is extracted for each angle-stack (Figure 4.16). The PP and PS angle-dependent wavelets are extracted in a window from 600 to 1100 ms (500 ms window length) and from 700 to 1400 ms (700 ms), respectively. Note that the bandwidth of the near, middle, and far angle-stacks is very similar. Additionally, the PS data has higher frequency content than the PP.

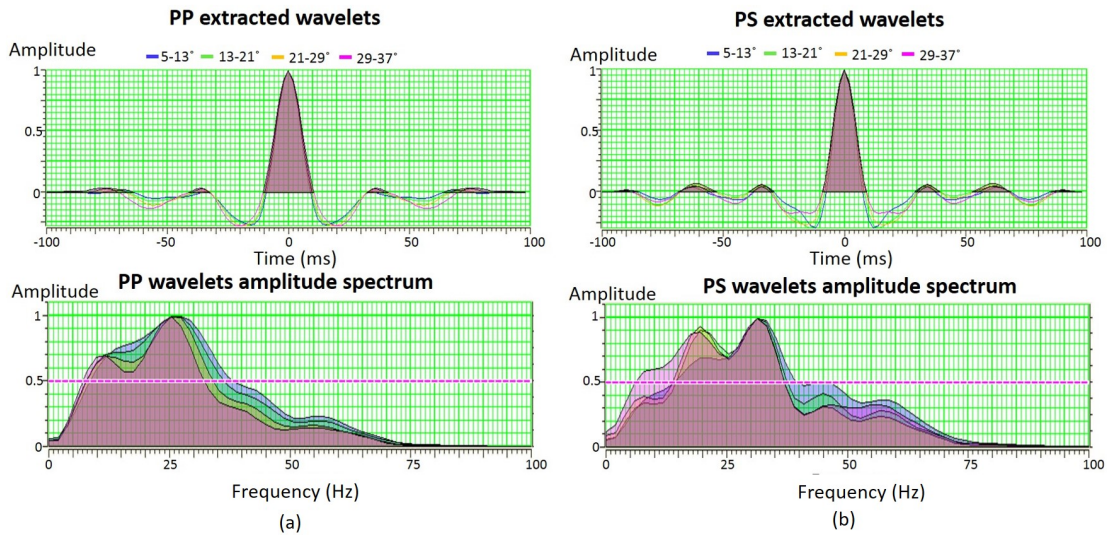


Figure 4.16: PP (a) and PS (b) statistical zero-phase extracted wavelets for 5-13° (blue), 13-21° (green), 21-29° (yellow), and 29-27° (magenta) and their corresponding amplitude spectra. Note that the PS angle-gathers have higher bandwidth and peak-frequency than the PP angle-gathers.

The PP and PS well-to-seismic ties are seen in Figure 4.17. There is a very good correlation between the angle-stacks and the synthetic seismograms (0.74 for the PP and 0.86 for the PS).

Low-frequency models are obtained in the same way as for the PP-PS post-stack joint inversion (using a 10-15 Hz high-cut filter).

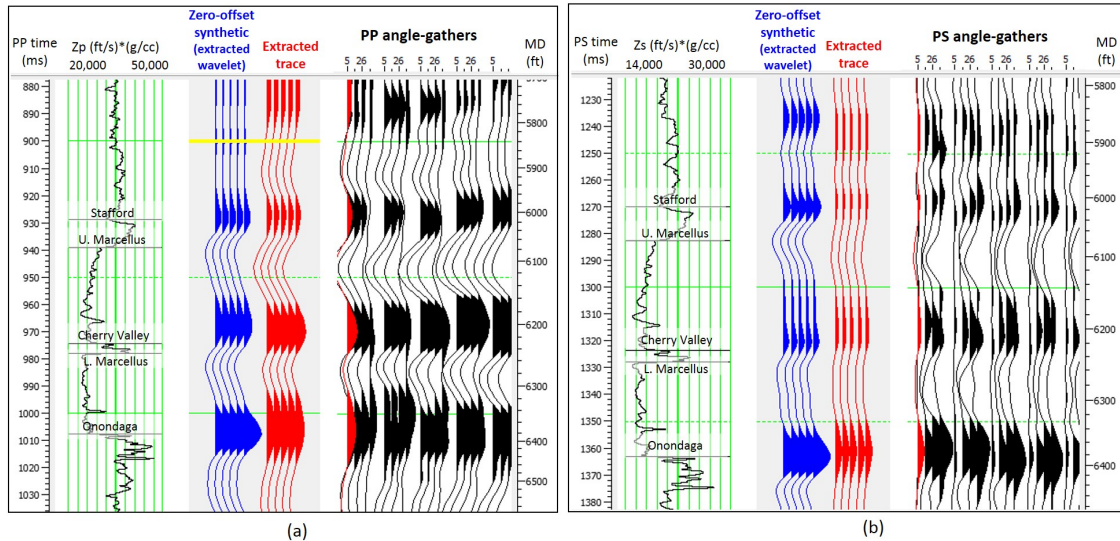


Figure 4.17: PP (a) and PS (b) angle-gathers well-to-seismic ties in their native times. Figures show the impedance logs, the zero-offset ( $20^\circ$  in the case of the PS data) synthetic seismicograms (blue), the extracted traces from the  $5\text{-}13^\circ$  angle-stack, and the real angle-stacks. There is a very good correlation for both PP and PS well-to-seismic ties (0.74 for the PP and 0.86 for the PS)

The same background trend generated for the PP-PS post-stack joint inversion (see Figure 4.8 and Table 4.1) is used in the pre-stack inversions.

Figure 4.18 shows the comparison between the PP pre-stack simultaneous inversion and the PP-PS pre-stack joint inversion at the OTIS 2H well location. Note that by incorporating the shear-wave information the inversion error decreases substantially for all the inversion products. Additionally, the inverted curves from the PP-PS joint inversion are less noisy, especially at the reservoir level. The S-impedance inversion error is less than the error of the P-impedance inversion. This has also been

observed in the post-stack joint inversion results. It is worth mentioning that, even though the PP gathers are not the best quality, both inversions are capturing the low-density present at the Lower Marcellus interval.

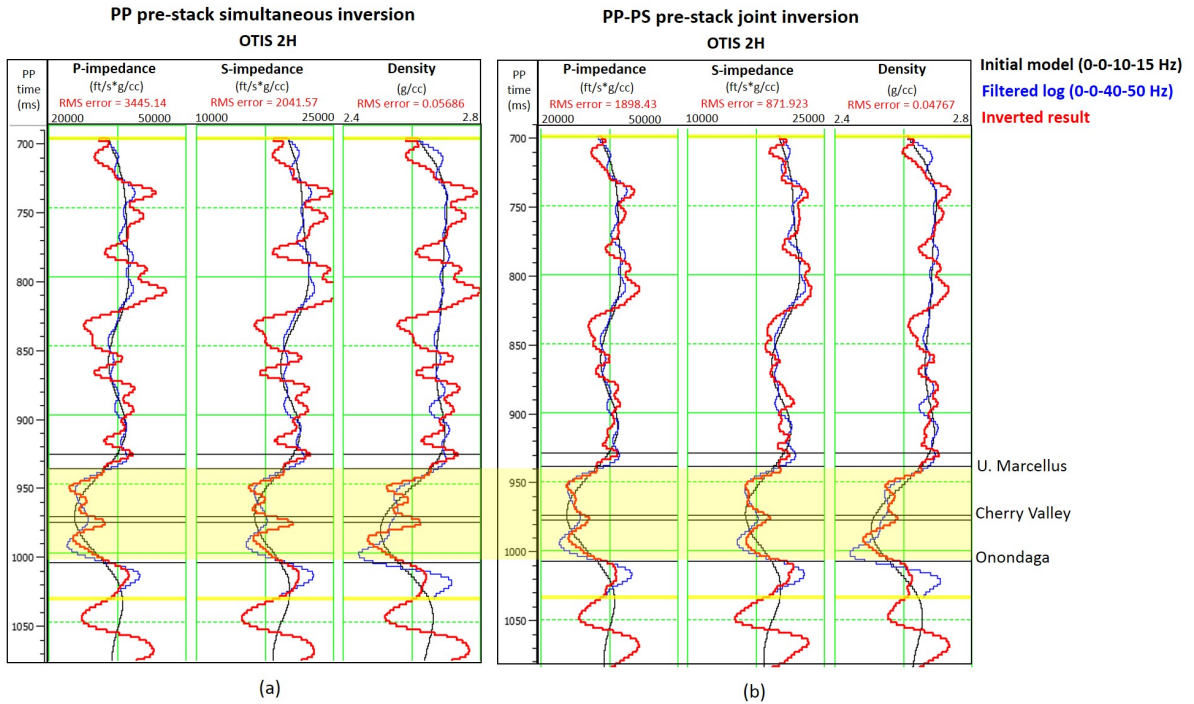


Figure 4.18: Comparison between the PP pre-stack simultaneous inversion (a) and the PP-PS pre-stack joint inversion (b) results at the OTIS 2H well location. Note that by incorporating the shear-wave information the inversion error decreases substantially for all the inversion products.

Table 4.2 shows the percent difference between the RMS errors from the inversion results at the OTIS 2H well location. By comparing the inversion errors for each parameter, it should be noted that the addition of converted-wave data to the inversion decreases the error by 58 % for P-impedance, 80 % for S-impedance and

18 % for density.

Inversion type	Z <sub>p</sub> (ft/s*g/cc)	Z <sub>s</sub> (ft/s*g/cc)	Density (g/cc)
PP only	3445.14	2041.57	0.05686
PP-PS joint	1898.43	871.923	0.04767
Difference (%)	57.89	80.29	17.58

Table 4.2: Comparison between the PP simultaneous inversion (PP only) and the PP-PS joint inversion (PP-PS joint) RMS errors for P-impedance, S-impedance, and density estimations at the OTIS 2H well location. The last row shows the percent difference between the errors of both inversion methods for each parameter.

Since the PP-PS post-stack joint inversion shows better results than the pre-stack inversions, the analysis is performed using those inverted volumes.

## 4.4 Identification of high-TOC and brittle facies

Based on the well-log and petrophysical interpretation presented in Chapter 2, the inverted volumes are now used to map the areal distribution of the high-TOC "Hot" Lower Marcellus interval.

Figure 4.19 shows the mean-density extracted over the Upper Marcellus (from Upper Marcellus to Onondaga) and Lower Marcellus (from Cherry Valley to Onondaga horizons). The Upper Marcellus shows higher-density values than the Lower Marcellus, mainly due to the difference in kerogen content and possibly porosity between the two intervals. In the Lower Marcellus density map, the three known gas-producing wells fall within density values lower than, approximately, 2.5 g/cc (red). Slightly higher-density values (cyan) may correspond to lithology changes (lower TOC or

higher clay volume), lower porosities or a thinner "Hot" Lower Marcellus interval.

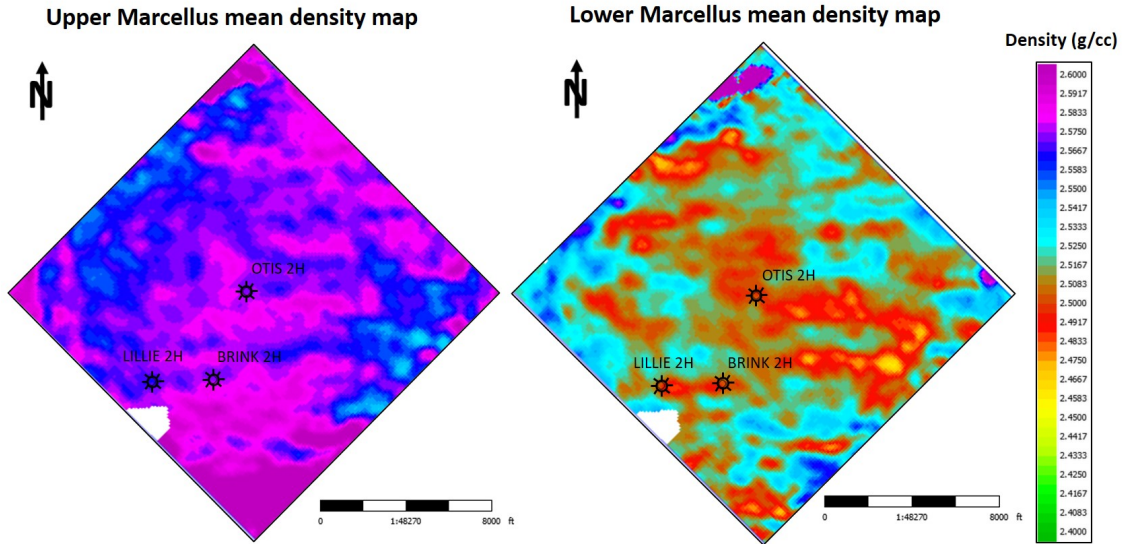


Figure 4.19: Upper Marcellus (a) and Lower Marcellus (b) density maps showing the mean-density values over both intervals. The Upper Marcellus shows higher-density values than the Lower Marcellus, mainly due to the difference in kerogen content and possibly porosity between the two intervals. The three known gas-producing wells fall within density values lower than, approximately, 2.51 g/cc in the Lower Marcellus interval.

Since the "Hot" Lower Marcellus interval is below seismic resolution, with a thickness of 50 ft at the OTIS 2H well, well-logs are upscaled using Backus average to integrate them in the analysis of the inverted data. For upscaling, a 100 ft window is used (approximate seismic resolution). The comparison between the P-impedance, density, and  $V_p/V_s$  upscaled logs and inverted data is seen in density vs. P-impedance, and density vs.  $V_p/V_s$  cross-plots in Figure 4.20. The squares

represent the upscaled well-log data colored by interval: black represents the "Hot" Lower Marcellus, red represents the low-TOC upper part of the Lower Marcellus and green represents the Upper Marcellus. The underlying data corresponds to the inverted-seismic data, also colored by interval but since the "Hot" Lower Marcellus top cannot be picked in the seismic, the red dots represent the whole Lower Marcellus formation (from Cherry Valley to Onondaga), while the green dots represent the Upper Marcellus formation (from Upper Marcellus to Cherry Valley). Samples in gray correspond to the rest of the inverted data (above and below the Marcellus Formation). Note that after upscaling the logs, the "Hot" Lower Marcellus cannot be discriminated from the rest of the Lower Marcellus interval in the density vs.  $V_p/V_s$  space (4.20b). However, it can still be discriminated in the density vs. P-impedance domain (4.20a).

Figure 4.21 shows the highlight of density values lower than 2.5 g/cc, which corresponds to the high-TOC "Hot" Lower Marcellus interval, and the OTIS 2H log-plot, where the highlighted interval is seen in red. The inverted data seen in the cross-plot corresponds only to the inline that goes through the OTIS 2H well (seen in Figure 4.22a), not to the entire seismic volume. Note that both density and P-impedance logs show an increase towards the base of the Lower Marcellus in the upscaled logs because of the effect of the high-density and high-impedance Onondaga limestone that sits below.

The vertical and areal distribution (extracted at 8 ms above the reservoir base) of the highlighted interval is shown in Figure 4.22. The upscaled density log is plotted at the OTIS 2H well location (4.22a). Even though the "Hot" Lower Marcellus

is below resolution, by cross-plotting the P-impedance and density-inverted data is possible to isolate the interval.

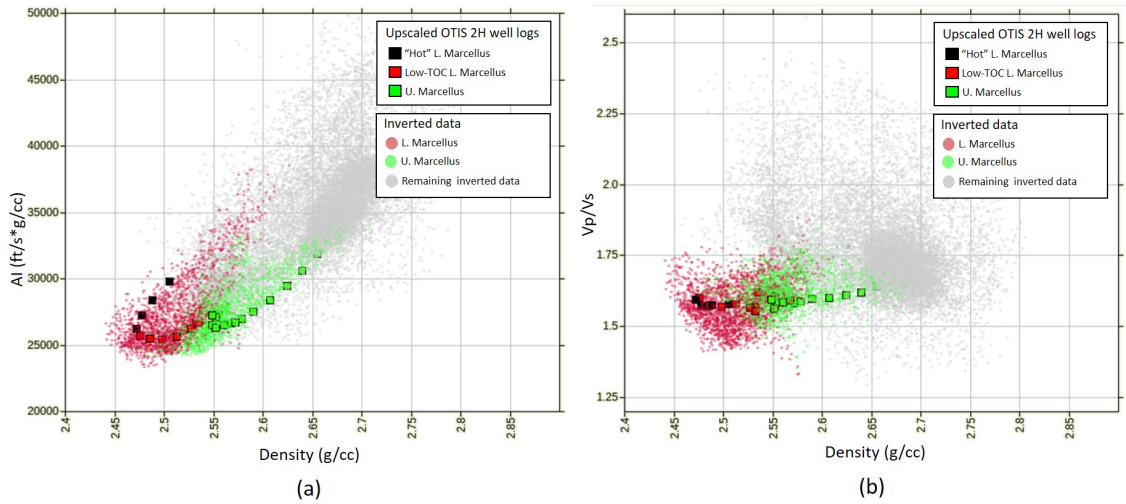
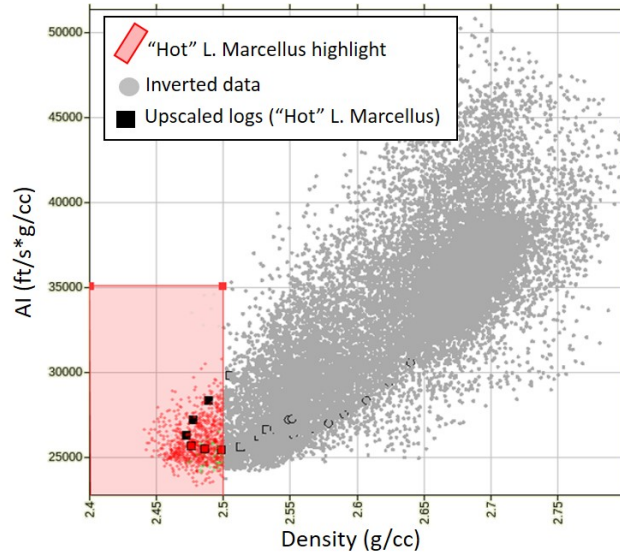


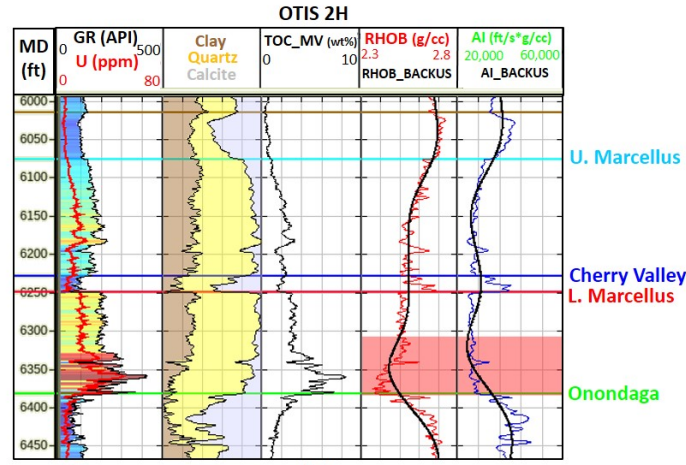
Figure 4.20: Density vs. P-impedance (a) and density vs.  $V_p/V_s$  (b) cross-plots showing the inverted data overlaid by the upscaled logs (squares). Both well-logs and inverted data are colored by interval. Note that after upscaling the logs, the "Hot" Lower Marcellus (black squares) cannot be discriminated from the rest of the Lower Marcellus interval in the density vs.  $V_p/V_s$  space.

It was shown earlier that high brittleness is related to the volume of brittle materials (i.e. quartz, calcite), which is reflected in the elastic constants (Poisson's ratio and  $E$ ). It was also shown that Rickman's (2008) brittleness index was somewhat subjective and could only be used in a relative sense since it depends on the values used for renormalization. Multi-variate analysis is also commonly used to estimate a brittleness volume from brittleness curves calculated using the mineral volumes (e.g. Jarvie, 2007). However, a statistically significant number of wells is needed

for training and validation. The fact that, from the wells located inside the seismic survey, only one well goes through the Marcellus formation hinders the brittleness estimation using this approach. In this sense, the  $E\rho$  volume is used as a proxy for brittleness. Young's modulus is a measure of the stiffness of a material. Stiffer shales frac much better than ductile ones and the permeability is commonly enhanced in these zones (Sharma and Chopra, 2015). Figure 4.23 shows the comparison between the Lower Marcellus mean density,  $E\rho$ , and P-impedance maps. Dotted polygons approximately indicate the main low-density trend. Note that most of the low-density anomalies correlate to medium values of  $E\rho$  and P-impedance, however, blue arrows indicate low-density zones that exhibit higher P-impedance and  $E\rho$  values. This may indicate a change in mineralogy and/or increase in brittleness. Areas with higher densities correlate mostly to high P-impedance and high  $E\rho$  values that could correspond to a decrease in porosity that increases the stiffness of the rock, a decrease in TOC content, or a decrease in the thickness of the high-TOC interval. Low-density anomalies to the southeast of the OTIS 2H well show the lowest P-impedance and  $E\rho$  values, which may indicate a decrease in brittleness.



(a)



(b)

Figure 4.21: Density vs. P-impedance cross-plot highlighting the high-TOC "Hot" Lower Marcellus interval (a) and the OTIS 2H log-plot showing the backtrack of the highlighted interval in red (b).

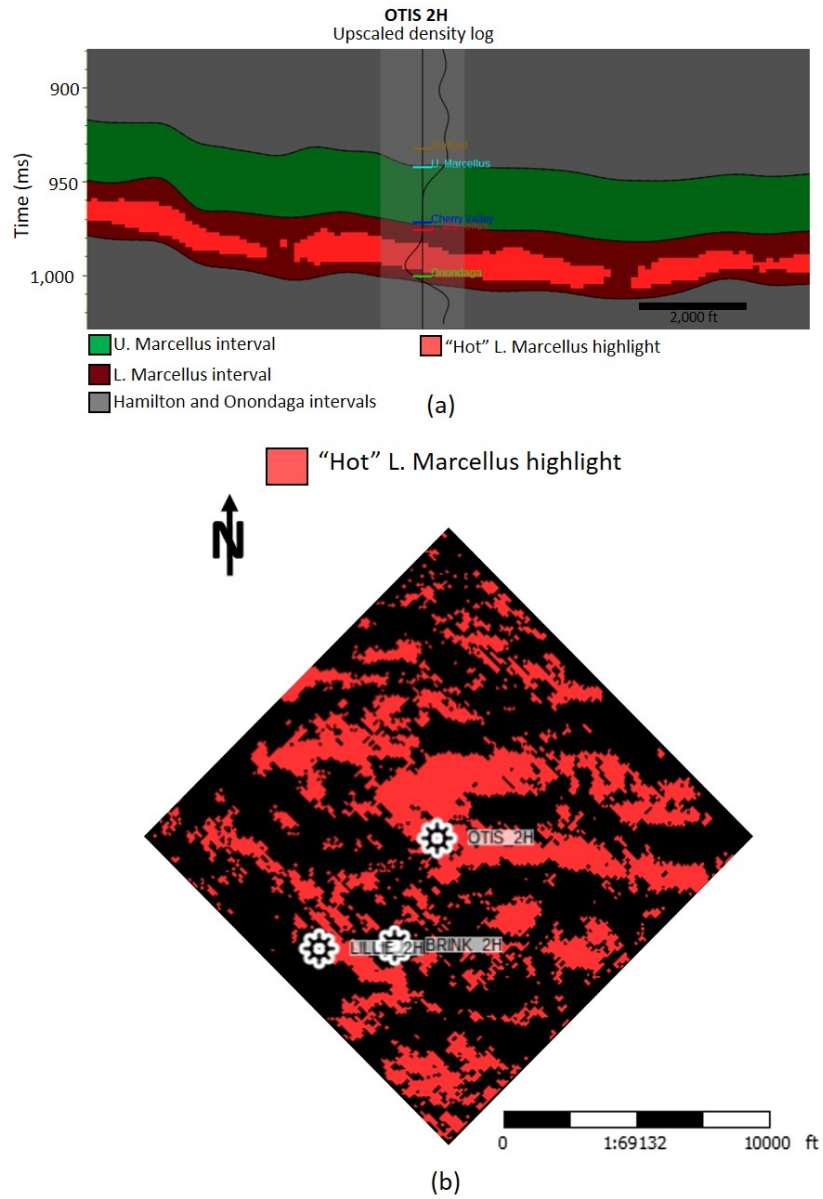


Figure 4.22: Vertical (a) and areal (b) distribution of the high-TOC "Hot" Lower Marcellus interval. The upscaled density log is plotted at the OTIS 2H well location and the map is extracted at 8 ms above the reservoir base.

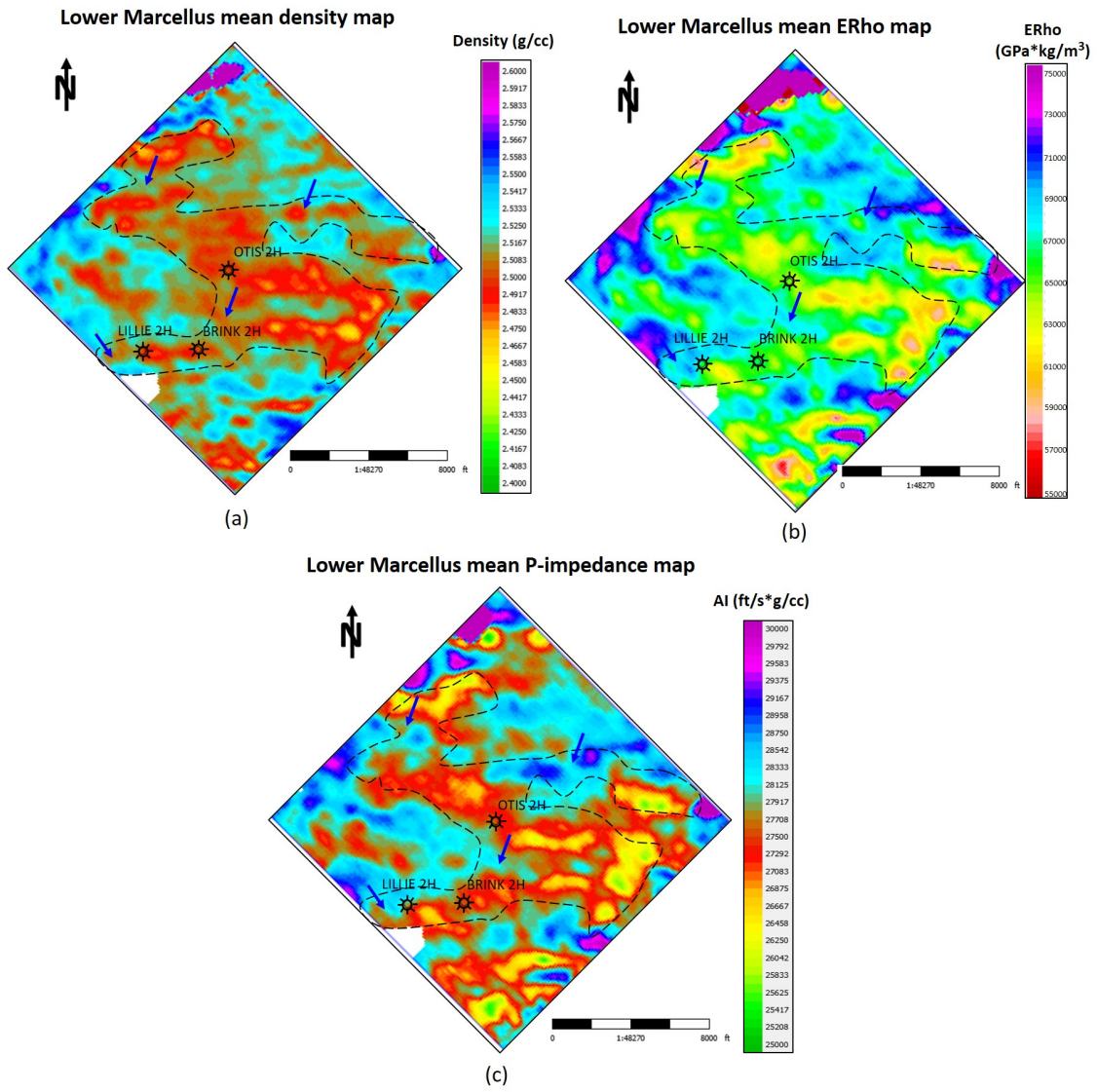


Figure 4.23: Comparison between the mean density (a),  $E\rho$  (b) and P-impedance (c) values over the Lower Marcellus Formation. Dotted polygons indicates the main low-density trend. Blue arrows indicate low-density zones that exhibit high P-impedance and high  $E\rho$  values. This may indicate a change in mineralogy or increase in brittleness.

To further refine the location of low-TOC and high-brittle areas, a cross-plot between density and  $E\rho$  (Figure 4.24) allows mapping different facies based on the maps seen in Figure 4.23:

- Low-density and low- $E\rho$  (densities and  $E\rho$  values lower than 2.5 g/cc 67 GPa  $\times$  g/cc, respectively) the red polygon.

- Slightly higher densities and low  $E\rho$  (densities between 2.5 and 2.52 g/cc and  $E\rho$  values lower than 67 GPa  $\times$  g/cc) the orange polygon.

- Low density and higher  $E\rho$  values (densities lower than 2.5 g/cc and  $E\rho$  values higher than 67 GPa  $\times$  g/cc) the cyan polygon.

- Higher densities and higher  $E\rho$  values (densities between 2.5 and 2.52 g/cc and  $E\rho$  values higher than 67 GPa  $\times$  g/cc) the blue polygon.

Note that the inverted data seen in the cross-plot corresponds only to the line that goes through the OTIS 2H well (seen in Figure 4.25a). The cutoffs used to define the polygons are taken from the previously shown maps of density and  $E\rho$  average values over the Lower Marcellus.

The distribution of these areas extracted at a line going through the OTIS 2H and at 7 ms above the reservoir base is seen in Figure 4.25b. The hot colors (red and orange) correspond to relatively low  $E\rho$  values and the cold colors (cyan and blue) correspond to the highest  $E\rho$  values. The lowest densities (lower than 2.5 g/cc) are seen in the red and cyan polygons, being the cyan samples the ones that exhibit a combination of low TOC and high  $E\rho$ . Mapping the distribution of these facies at different levels, as well as a thorough understanding of the geological and/or

structural factors driving the observed lateral variability, would aid in well-placement and targeting.

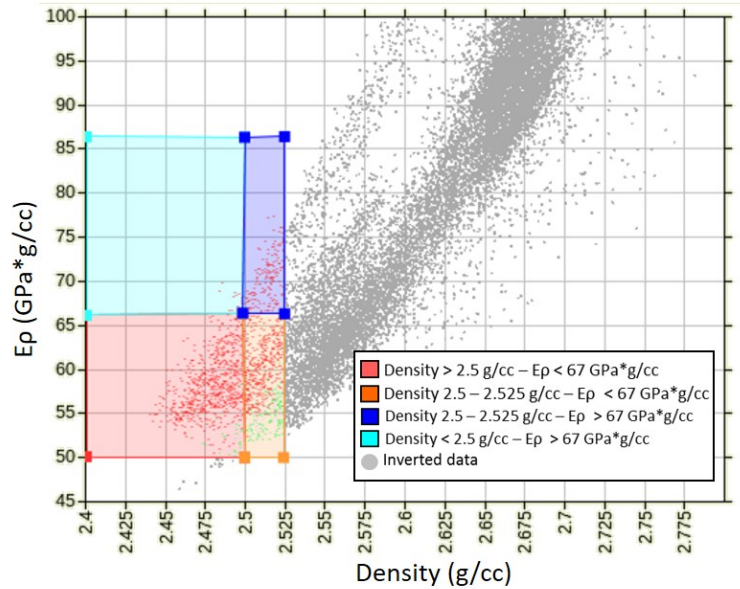


Figure 4.24: Density vs.  $E\rho$  cross-plot highlighting the following: low-density and low- $E\rho$  (densities and  $E\rho$  values lower than 2.5 g/cc 67 GPa  $\times$  g/cc, respectively) the red polygon, slightly higher densities and low  $E\rho$  (densities between 2.5 and 2.52 g/cc, and  $E\rho$  values lower than 67 GPa  $\times$  g/cc) the orange polygon, low-density values and higher  $E\rho$  values (densities lower than 2.5 g/cc and  $E\rho$  values higher than 67 GPa  $\times$  g/cc) the cyan polygon, and higher densities and higher  $E\rho$  values (densities between 2.5 and 2.52 g/cc and  $E\rho$  values higher than 67 GPa  $\times$  g/cc) the blue polygon.

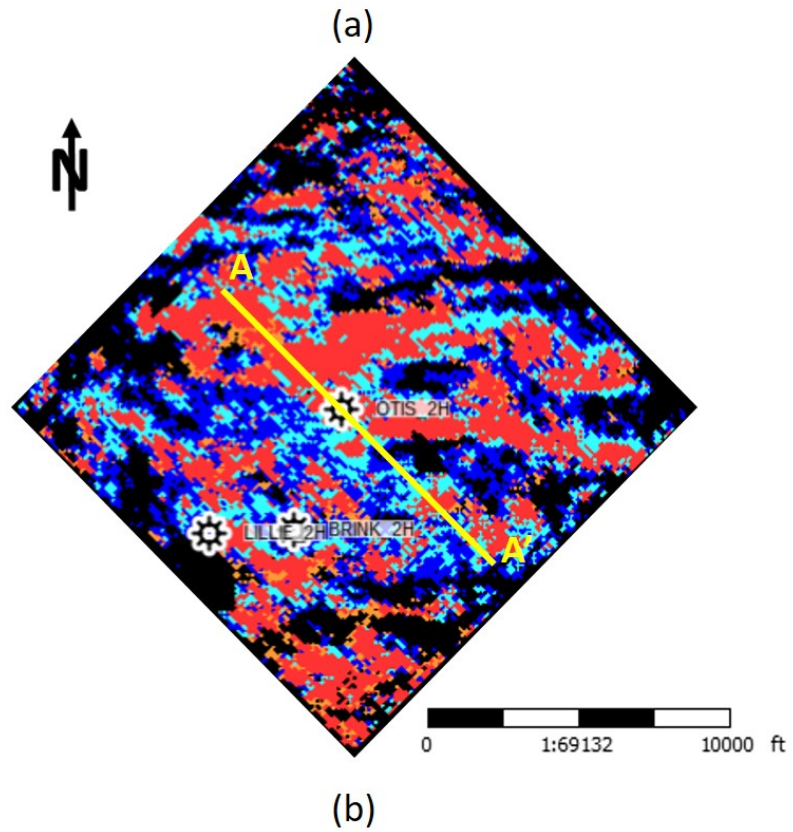
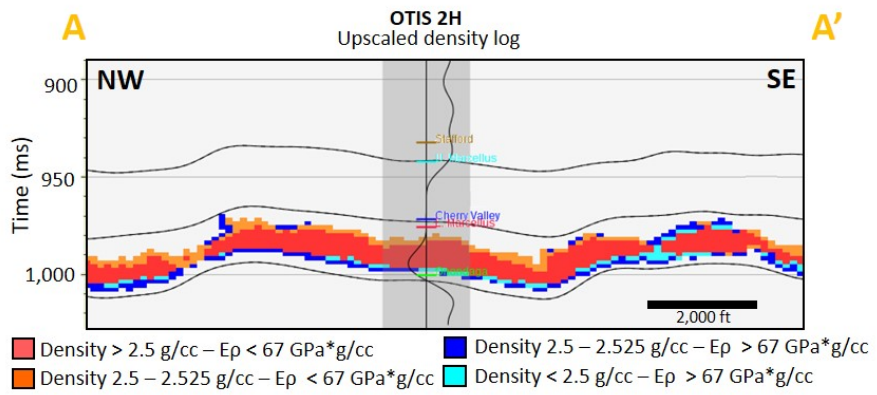


Figure 4.25: Vertical (a) and areal (b) distribution of the polygons highlighted in Figure 4.24. The upscaled density log is plotted at the OTIS 2H well location and the map is extracted at 7 ms above the reservoir base.

# Chapter 5

## Conclusions, recommendations, and future work

This study integrates petrophysical and well log analysis, rock-physics and seismic modeling to understand the relationship between rock properties and the elastic response. Based on this analysis, the inverted results from a PP-PS joint inversion are used to locate areas that exhibit high TOC content and might also be suitable for hydraulic fracturing.

From this work, the following conclusions can be drawn:

- The Marcellus Shale presents a highly variable vertical and lateral mineralogy. The base of the Lower Marcellus exhibits the highest TOC content (from 6 to 9 wt. %) and the lowest clay content (up to less than 20 %) in the study area.
- The TOC estimation in the study area is improved by a multi-variate analysis

that includes the uranium, gamma ray, density, and Poissons ratio logs.

- Cross-plots of the available well logs indicate that kerogen seems to be the main property driving density changes in the study area, where zones with TOC higher than 6 wt. % show density values lower than 2.5 g/cc. P-impedance, S-impedance, and  $V_p/V_s$  seem to be more sensitive to variations in clay content than kerogen content. Within the high-TOC areas,  $V_p/V_s$  and P-impedance decrease as clay content decrease.  $V_p/V_s$  show values lower than 1.5 when the clay volume percentage is less than 25 %.

- In the high-TOC interval, velocities increase by approximately 7 %. This seems to be caused by an interplay between mineralogy and kerogen content, where the kerogen effect appears to be masked by a decrease in clay and increase in quartz and calcite in this interval.

- Brittleness estimations using the mineral volumes, Rickmans (2008) approach,  $E\rho/PR$  and  $E\rho$  show a somewhat consistent trend, increasing at the high-TOC interval.

- Rock-physics modeling using the DEM approximation confirms our observations during cross-plot analysis: density is more sensitive to variations in kerogen content than P-impedance. A small change in porosity has major effects on the elastic properties of the rock. The change on P-impedance is largely driven by both porosity and clay content. Additionally, as porosity decreases, the density seems to increase its sensitivity to changes in clay content.

- AVA modeling shows that PP and PS reflections are both sensitive to the

high-TOC interval. Its sensitivity increases with incidence angles higher than, approximately, 25 degrees. The change in PP amplitudes seems to be bigger than the change in PS amplitudes, which suggest that the compressibility seems to be more sensitive to the high-TOC interval than the rigidity.

- A comparison between PP and PP-PS inversions show that the addition of converted-wave data decreases the P-impedance, S-impedance, and density estimation errors by 58, 80, and 17 %, respectively.

- The PP-PS joint inversion allows a robust density estimation used to indicate promising reservoir quality areas. These predictions suggest good reservoir where two gas wells (not used in the analysis) are producing.

- The integration between petrophysics, rock-physics, and the inversion results assisted in identifying good reservoir quality areas characterized by high TOC and high brittleness.

## **5.1 Recommendations and future work**

There are multiple avenues for future work:

- Include a statistical facies classification (e.g. Bayesian classification) to estimate the probability of the high-TOC facies.

- The rock-physics model assumes randomly distributed inclusions. Anisotropy could be taken into account using the anisotropic Backus averaging method (Vernik and Nur, 1992; Guo et al., 2012). Additionally, the seismic sensitivity to variations

in anisotropic parameters could be explored.

- The applied technique allowed the identification of the high-TOC interval. However, it can only be identified as a package. If more detailed interpretation and higher resolution is needed for targeting, is necessary to apply frequency-enhancement techniques that allow a better discrimination within the high-TOC interval (i.e. to be able to discriminate bodies with high TOC and high clay content from others with high TOC and low clay content).

- The inversion could be updated incorporating data from new wells. This would allow the application of geostatistics and multi-variate analysis for rock-property estimation.

- AVAZ analysis to study the azimuthal variations in P-wave velocities and/or amplitudes would help understand the azimuthal stress anisotropy. Inversion of azimuthal sectors could also be performed.

# Appendices

# Appendix A

## PP seismic gather conditioning

I conditioned the P-wave pre-stack seismic gathers according to the following workflow:

- 1) Mute to remove traces corresponding to angles higher than  $45^\circ$
- 2) Bandpass filter for high-frequency noise attenuation
- 3) Parabolic-Radon filter for random noise attenuation
- 4) Parabolic-Radon filter for multiple attenuation
- 5) Bandpass filter for high-frequency noise attenuation
- 6) Trim statics to align the reflection data and improve the SNR

The PP offset gathers are converted to angle gathers and angles higher than  $45^\circ$  were muted. Figure A.1 shows the PP pre-stack gathers overlaid by the P-wave incident angle. The red polygon encloses the target area, where the maximum offset

corresponds to, approximately, 14,800 ft, which results in an angle higher than  $45^\circ$  for the reservoir depth (approximately 6,000 ft).

An  $f - k$  spectrum plot is computed to determine the range of usable frequencies and estimate the slopes of the bandpass filter (first step in the gather conditioning). Coherent linear noise such as ground roll, guided waves, and side-scattered energy can be separated in the  $f - k$  domain by their dip (Yilmaz, 1987). The  $f - k$  spectrum plot of the P-wave data (Figure A.2) shows dipping coherent noise to the right of the plot (a), with a frequency range between 0 and 15 Hz, while the signal cone is situated around the frequency axes (b). Usable signal seems to be concentrated between 5 and 50 Hz. Based on this observations, a bandpass filter of 3-8-60-80 Hz is applied attempting to remove the high-frequency noise.

Figure A.3 shows the PP gathers before and after the bandpass filter, and the residual (what was removed by the filter). The data looks cleaner after the bandpass filter and the reflections can be better distinguished. There is still some high and low-frequency noise left in the data, but we don't want to remove all the low-frequency signal because it is needed for the inversion, and also don't want to remove all the high frequency because a broad bandwidth is needed to ensure the highest possible resolution. For this reason, I will apply other techniques rather than bandpass filters to try to attenuate the noise left. The incoherent character of the residual indicates that the filter is removing primarily random noise and not signal.

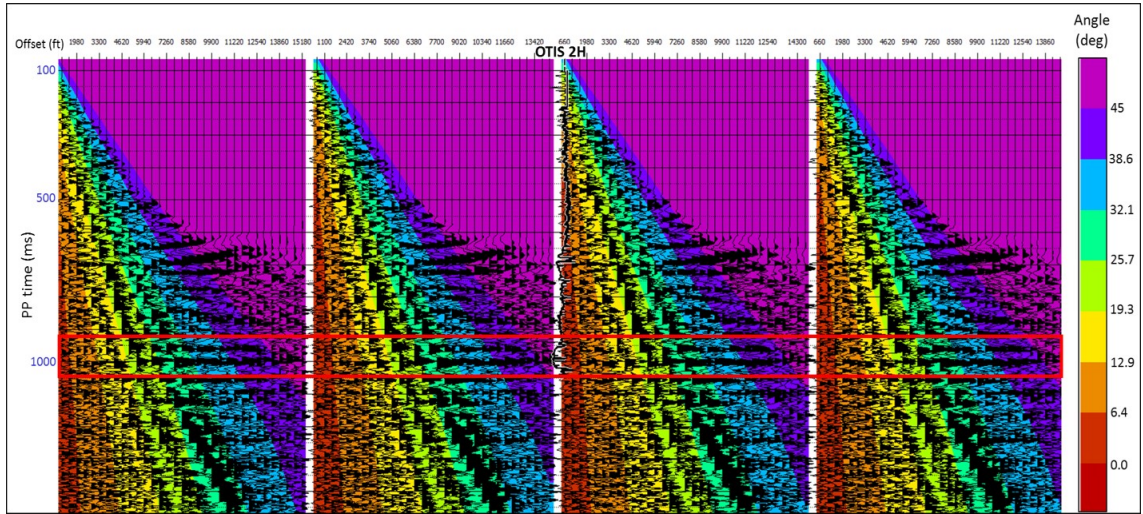


Figure A.1: P-wave pre-stack offset gathers overlaid by the incident angle. The target interval is enclosed in the red polygon. The maximum recovery angle for an offset of 14,700 ft (maximum offset) is higher than  $45^\circ$  for the target depth. Angles higher than  $45^\circ$ .

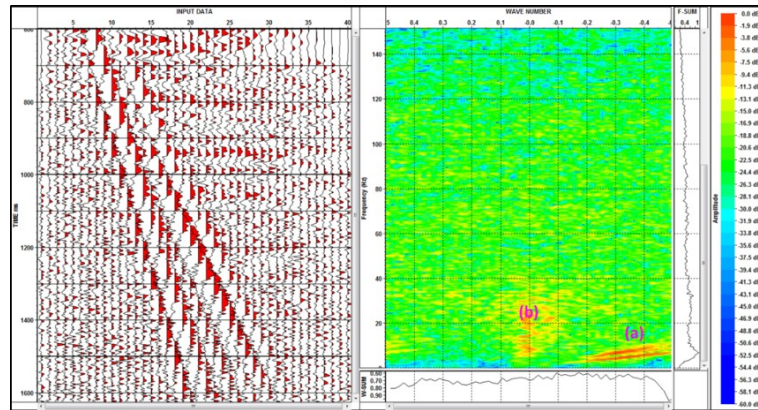


Figure A.2:  $F - k$  spectrum plot of the PP data. Coherent low-frequency linear noise is identified in the dipping event (a), while reflection signal is situated around the frequency axes (b).

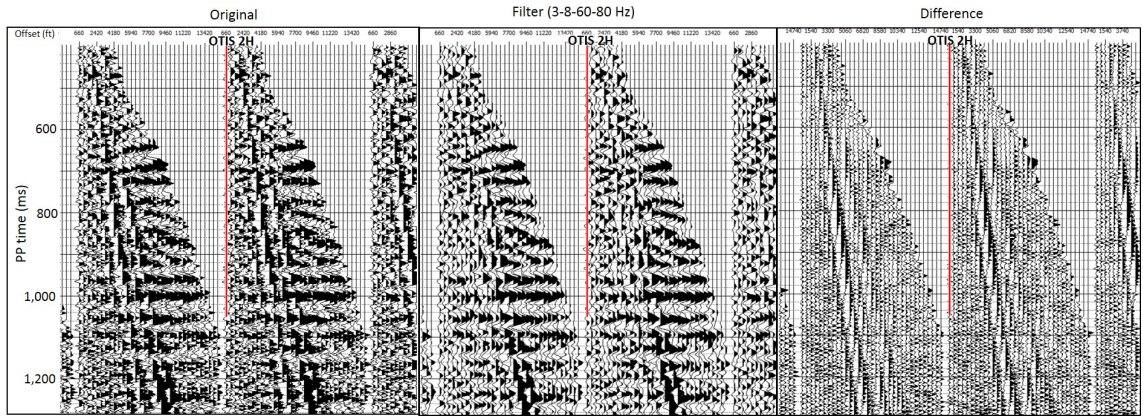


Figure A.3: Comparison between the migrated P-wave pre-stack gathers near the OTIS 2H well location before (left panel) and after the 3-8-50-80 Hz bandpass filter (middle panel), and the residual (right panel), that is, the original P-wave gathers minus the filtered P-wave gathers.

$f - k$  filters are commonly used to suppress noise, however, it has been shown (Ross, 1999) that such filters produce severe distortion of the AVO response at middle and far offsets. Conversely, parabolic-Radon methods have been successfully applied for both noise and multiple attenuation before AVO analysis (Hampson, 1986). A comparison between the amplitude of the primary after filtering with the two methods is shown in Figure A.4. The Radon method maintains a linearly increasing amplitude with offset, with small deviations at near and far offsets, however the  $f - k$  method shows big distortions of the AVO. With this in mind, I decided to use the parabolic-Radon filter for both noise and multiple attenuation.

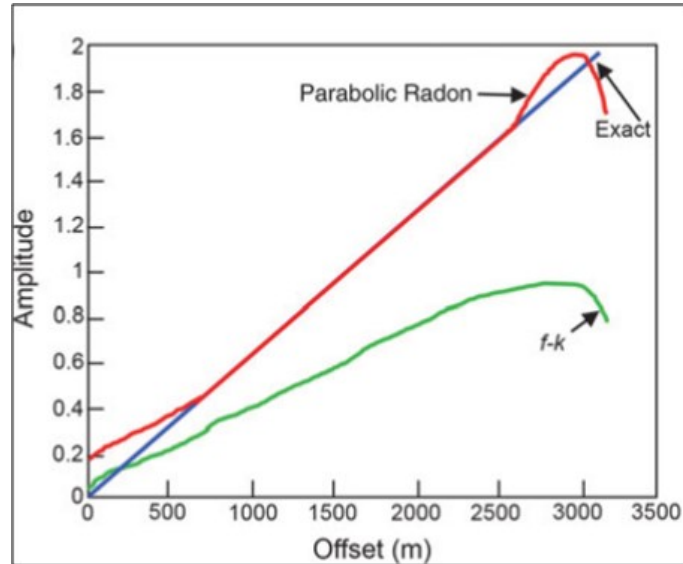


Figure A.4: Comparison between amplitudes of primaries after multiple suppression using the  $f - k$  (green) and the parabolic-Radon (red) methods. The blue line shows the exact AVO of the primaries (From Ross, 1999).

Hampson's (1986) parabolic-Radon transform assumes that, after NMO, all coherent events can be modeled as parabolic shapes. At each time sample the algorithm uses a fan of possible parabolas to model the events actually found in the data, assuming that the seismic gather is a combination of modeled primaries, modeled multiples and random noise. The fan is divided into two components (Figure A.5), and all events with a move-out greater than a specified cutoff are assumed to be multiples. The parabolas do not model the data completely because of the presence of noise, so everything that is not modeled by the parabolas is assumed to be random noise.

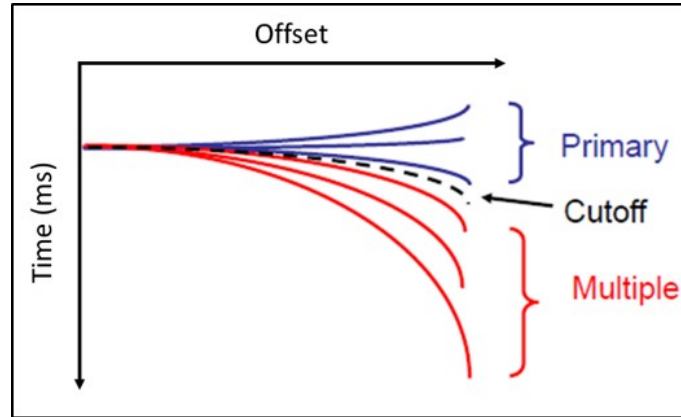


Figure A.5: Graphic explanation of the modeled primaries (blue) and multiples (red) in the parabolic-Radon filter (Modified from Hampson-Russell AVO workshop tutorial, 2015).

The algorithm solves for modeled primaries and modeled multiples. For random noise attenuation, it subtracts both modeled primaries and multiples from the original gathers. This gives the random noise, which is subtracted from the original gathers. For multiple attenuation, it just subtracts the modeled multiples from the original gathers.

Figure A.6 shows the P-wave gathers before and after the random noise attenuation using the parabolic-Radon filter, and the residual. The operator length is set between -20 and 100 ms. The filter removed almost all the ground-roll and a lot of the high-frequency noise that was left after the bandpass filter. The events can now be easily distinguished without the ground-roll interference.

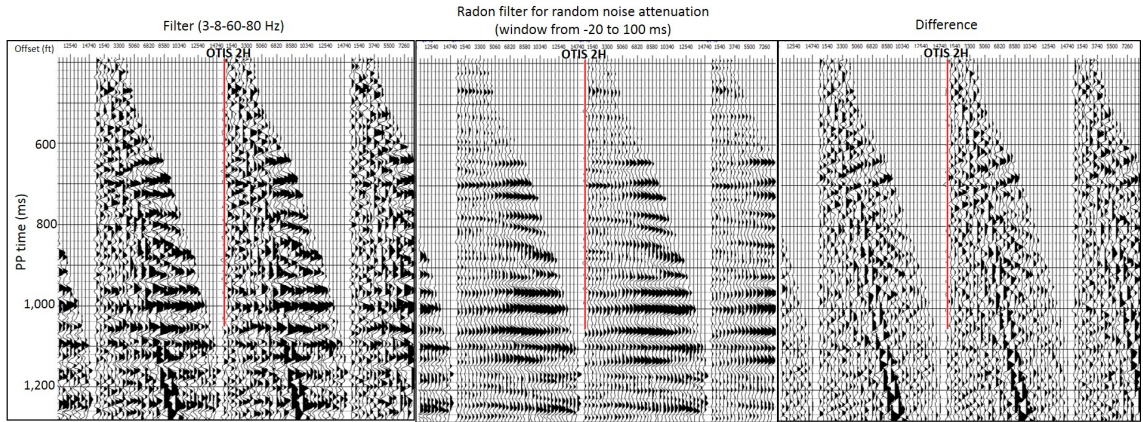


Figure A.6: Comparison between the filtered migrated P-wave pre-stack gathers near the OTIS 2H well (left panel), after the parabolic-Radon transform for random noise attenuation using a window between -20 and 100 ms (middle panel), and the residual (right panel).

After the random noise attenuation, the parabolic-Radon filter is used for multiple removal (Figure A.7). The parabolas are modeled between -100 and 100 ms (maximum move-out seen the difference between the synthetic and real data at the far offset), using a cutoff of 20 ms to separate primaries and multiples.

A 3-8-50-80 Hz bandpass filter is again applied to the data after the multiple suppression to eliminate any frequency artifact that could have been created by the Radon filters (Figure A.8). Note that the residual (left-most panel) is equal to zero almost everywhere but in the far-offset data.

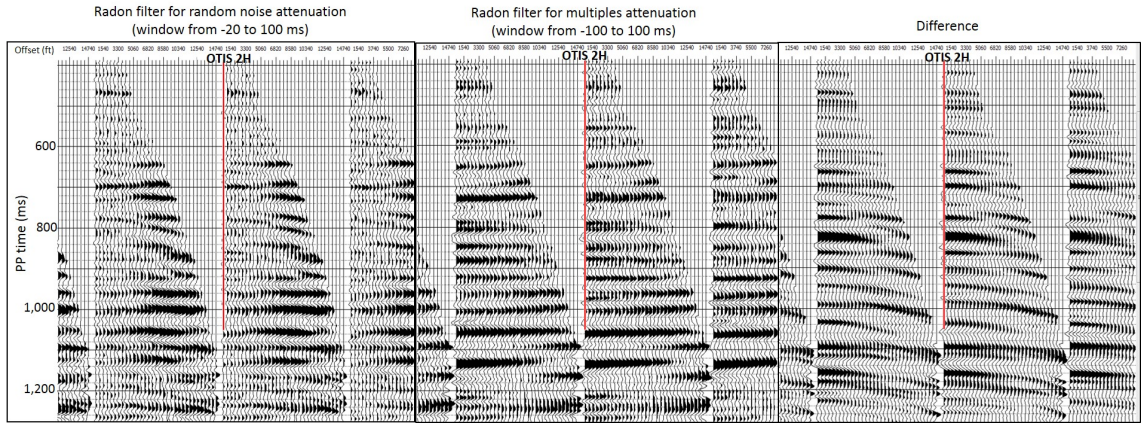


Figure A.7: Comparison between the migrated P-wave pre-stack gathers near the OTIS 2H well before the parabolic-Radon transform for multiple attenuation (left panel), after the application of the transform (middle panel), and the residual (right panel). The parabolas are modeled between -100 and 100 ms.

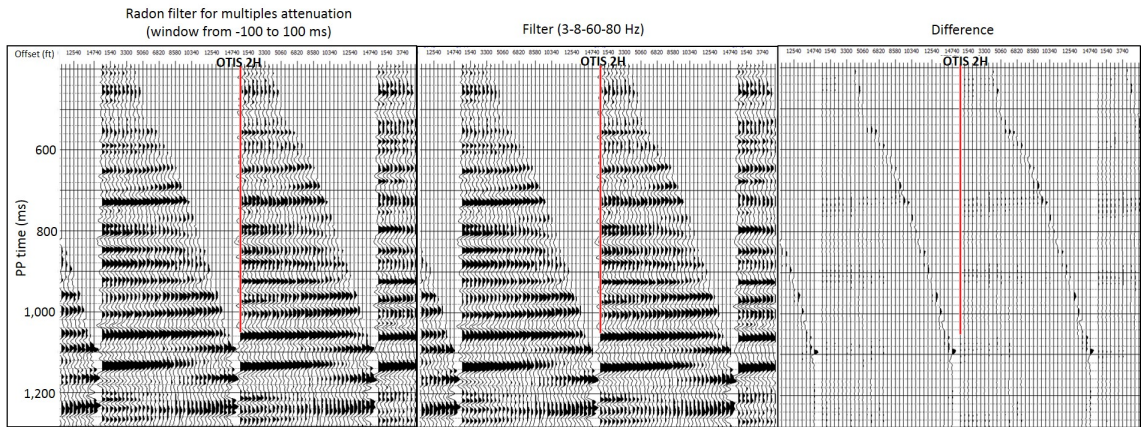


Figure A.8: Comparison between the migrated P-wave pre-stack gathers near the OTIS 2H well before the bandpass filter (left panel), after the bandpass filter (middle panel), and the residual (right panel).

As final step in the conditioning workflow, trim statics are applied to correct for residual move-out errors, aligning the events on pre-stack gathers. A pilot trace is formed by stacking each CDP gather, and then each trace is correlated with the pilot trace. The cross-correlation is used to calculate an optimal time shift for each trace, using a maximum allowed time shift of 12 ms. Figure A.9 shows the data before and after trim statics. The red polygon encloses the target interval. Note that the shifts are applied mostly to the far-offset traces.

The comparison between the original P-wave gathers and the gathers after the conditioning is shown in Figure A.10. Note how the high-frequency noise, multiples and ground-roll has been effectively removed.

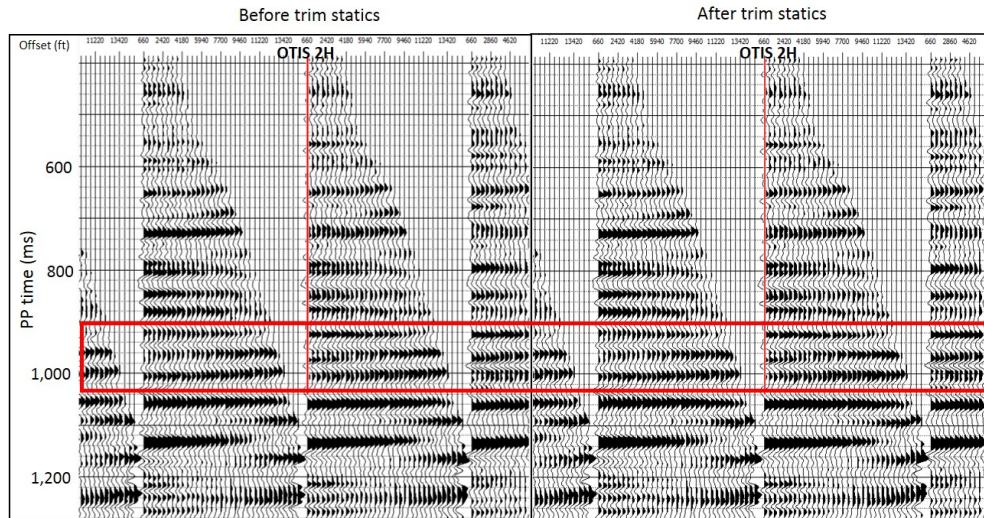


Figure A.9: Comparison between the migrated P-wave pre-stack gathers near the OTIS 2H well before (left panel) and after trim statics are applied (right panel). The red polygon encloses the target interval. Note that the shifts are applied mostly to the far-offset traces.

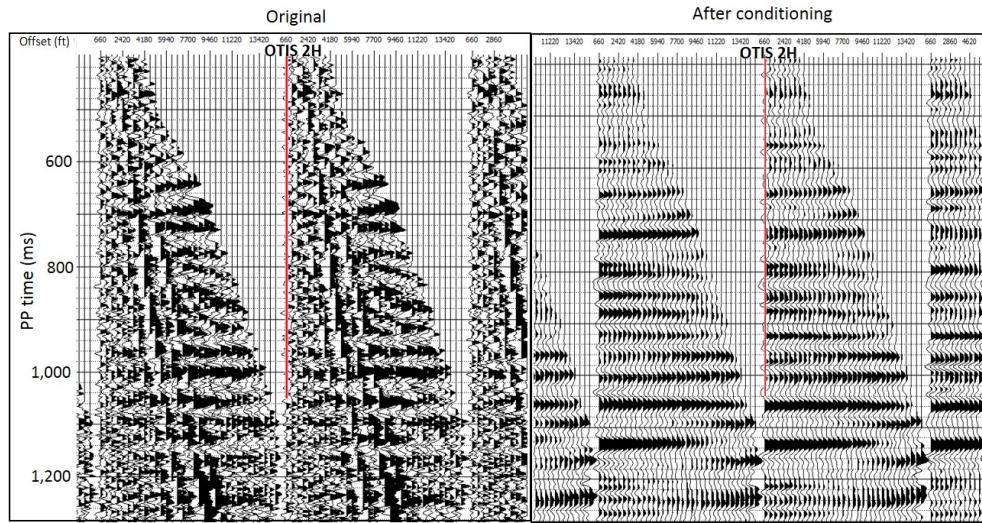


Figure A.10: Comparison between the original migrated P-wave pre-stack gathers near the OTIS 2H well (left panel) and the gathers after the application of the conditioning workflow (right panel). Note how the high-frequency noise, multiples and ground-roll has been effectively removed.

The AVO modeled response is now compared to the AVO of the real gathers before and after applying the Radon transform for multiple attenuation (Figure A.11). AVO curves are fitted with the three-term Aki-Richards AVO approximation. The Aki-Richards approximation A, B, and C coefficients for each curve are shown in Table A.1. Note how the gradient changes from positive to negative after removing the multiples, matching the negative gradient of the modeled response, however the curvature remains positive even after removing the multiples.

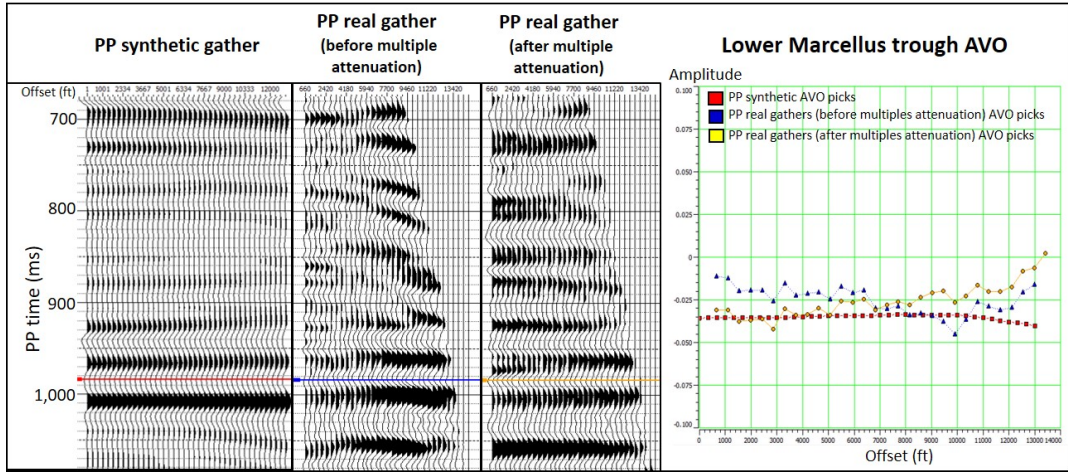


Figure A.11: Comparison between the synthetic PP AVO response (red) and the real gathers AVO response before (blue) and after (yellow) multiple attenuation using the Radon transform.

Coefficient	A	B	C
Synthetic AVO	-0.035	0.033	-0.098
Real AVO (before multiple attenuation)	-0.012	-0.205	0.412
Real AVO (after multiple attenuation)	-0.0338	0.016	0.152

Table A.1: Aki-Richards three-term AVO approximation coefficients for the AVO curves shown in Figure A.11. Coefficients A, B and C correspond to the intercept, gradient and curvature, respectively. The gradient changes from negative to positive after attenuating the multiples, matching the negative gradient of the modeled AVO response. The modeled AVO curvature is negative, while the real gathers AVO curvature is positive before and after multiples attenuation.

# Appendix B

## PS seismic gather conditioning

The PS gather conditioning follows a similar workflow:

- 1) Mute to remove traces corresponding to angles higher than  $45^\circ$
- 2) Bandpass filter for high-frequency noise attenuation
- 3) Parabolic-Radon filter for random noise attenuation
- 5) Bandpass filter for high-frequency noise attenuation

Figure B.1 show the PS pre-stack gathers overlaid by the P-wave incident angle. The red polygon encloses the target area, where the maximum P-wave incidence angle is, approximately,  $38^\circ$ .

The PS gathers  $f-k$  spectrum show less low-frequency coherent noise and random noise than the PP data (Figure B.2). A 3-8-60-80 Hz bandpass filter is also applied to the PS gathers since we want the final bandwidth of both PP and PS data to be as

similar as possible. Figure B.3 shows the comparison between the original migrated PS gathers before and after the bandpass filter (left and middle panel, respectively) and the difference between these two (left panel). Note how, as in the PP case, the filter effectively removes high-frequency noise.

The parabolic-Radon transform is used in the PS gathers only for random noise attenuation (Figure B.4), since multiples are not obviously observed and don't seem to be as prominent as in the PP data. The operator length goes from -20 to 30 ms. As for the PP data, the PS gathers are bandpass-filtered again to remove any artifact that the Radon transform might have produced (Figure B.5).

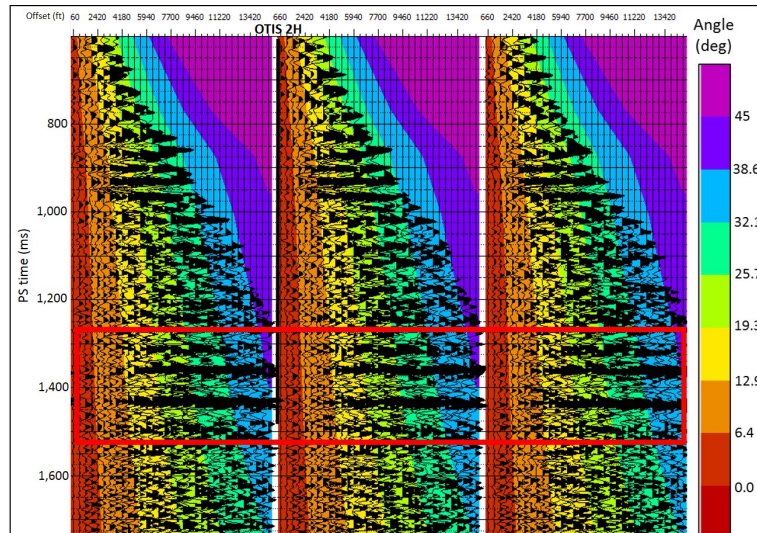


Figure B.1: PS migrated pre-stack gathers near the OTIS 2H well overlaid by the P-wave incidence angle. The red polygon encloses the target area, where the maximum P-wave incidence angle is, approximately,  $38^\circ$ .

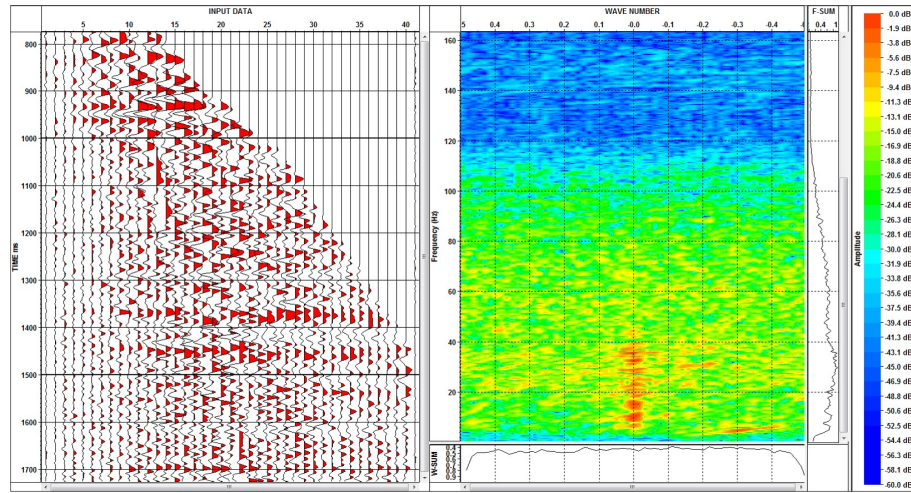


Figure B.2:  $f - k$  spectrum plot of the PS data. PS data show less random and coherent noise than the PP data.

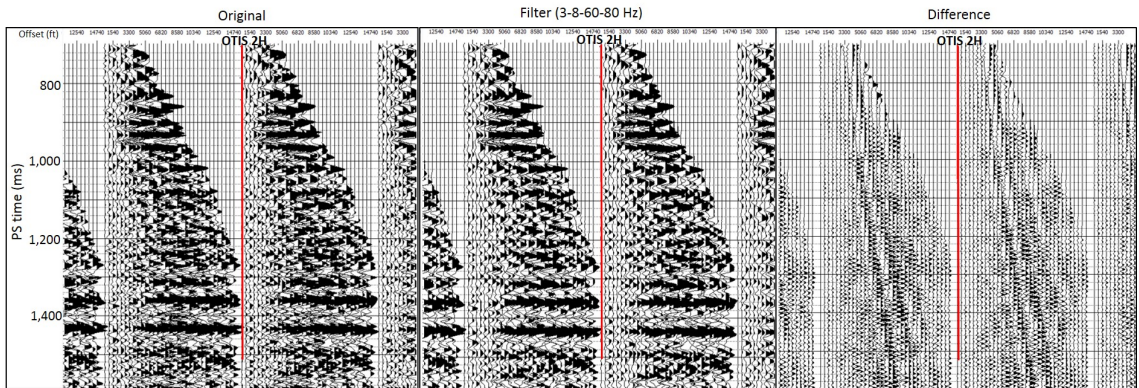


Figure B.3: Comparison between the migrated PS pre-stack gathers near the OTIS 2H well location before (left panel) and after the 3-8-50-80 Hz bandpass filter (middle panel), and the residual (right panel), that is, the original PS gathers minus the filtered PS gathers.

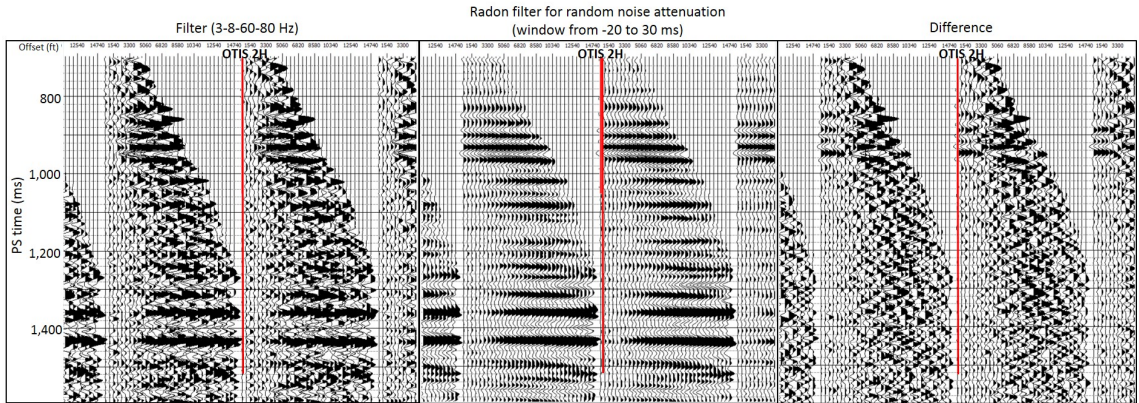


Figure B.4: Comparison between the filtered migrated PS pre-stack gathers near the OTIS 2H well (left panel), after the parabolic-Radon transform for random noise attenuation using a window between -20 and 30 ms (middle panel), and the residual (right panel).

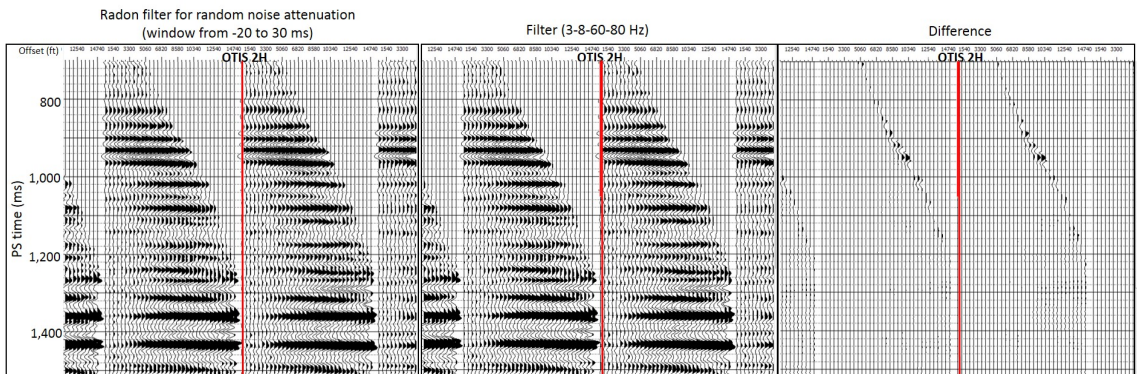


Figure B.5: Comparison between the migrated PS pre-stack gathers near the OTIS 2H well before the bandpass filter (left panel), after the bandpass filter (middle panel), and the residual (right panel).

The comparison between the original PS gathers and the gathers after the conditioning is shown in Figure B.6. Note how the high-frequency noise has been effectively removed.

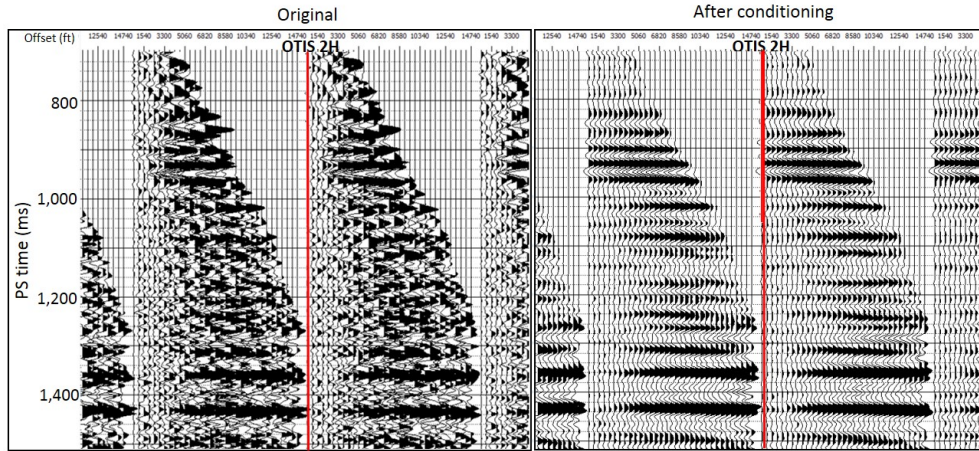


Figure B.6: Comparison between the original migrated PS pre-stack gathers near the OTIS 2H well (left panel) and the gathers after the application of the conditioning workflow (right panel). Note how the high-frequency noise has been effectively removed.

The PS AVO modeled response is now compared to the AVO response of the real PS gathers after the conditioning process (Figure B.7). Both curves show very similar behavior.

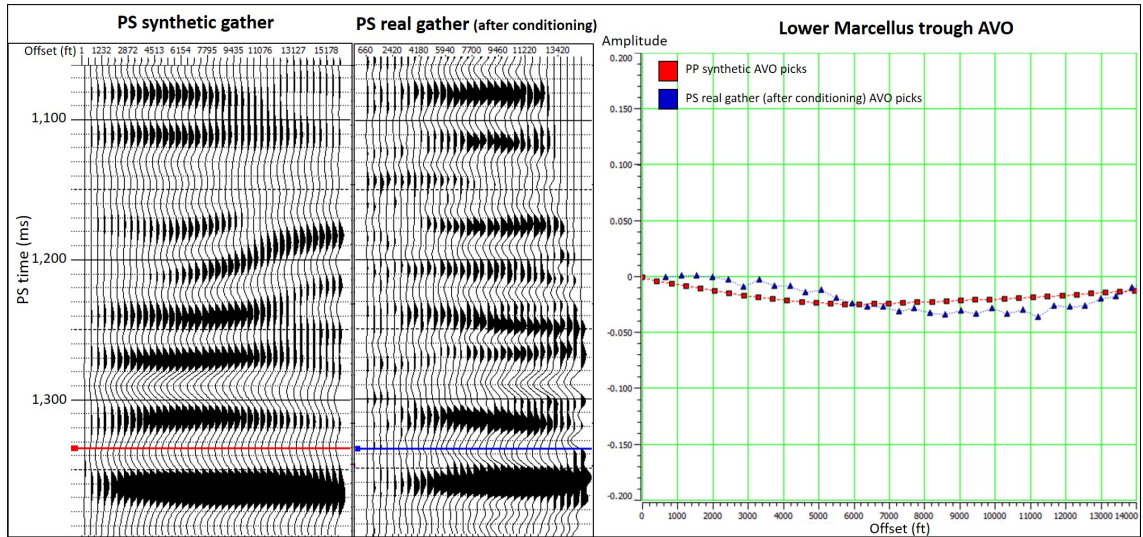
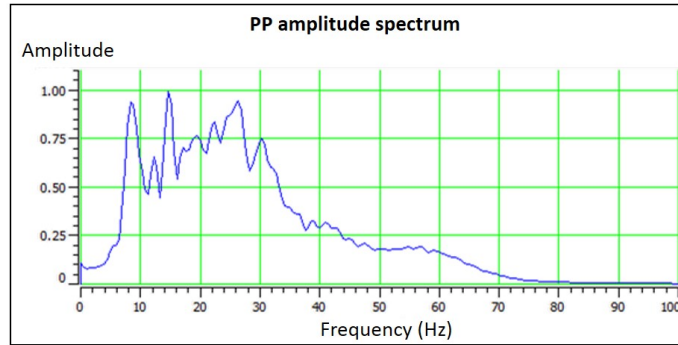
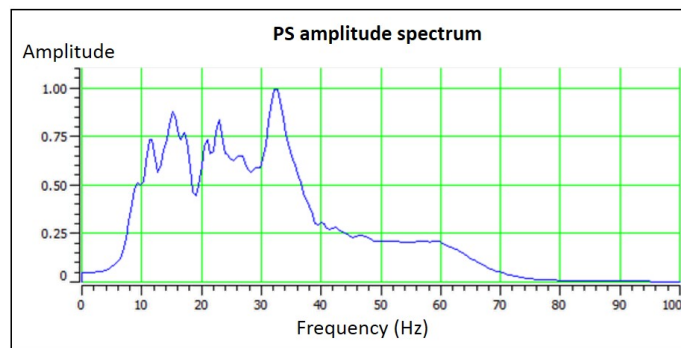


Figure B.7: Comparison between the synthetic PS AVO response (red) and the real gathers AVO response after the conditioning process (blue).

Both PP and PS amplitude spectra after the conditioning process are shown in Figure B.8. Their bandwidths are very similar, however the PS data shows higher amplitudes at high frequencies.



(a)



(b)

Figure B.8: Comparison between the PP (a) and PS (b) amplitude spectra after conditioning. Their bandwidths are very similar, however the PS data shows higher amplitudes at high frequencies.

## References

Alfred, D., and Vernik, L., 2013, A new petrophysical model for organic shales, *Geophysics*, 54(3), 240-247.

Alkahtani, A., and Tutuncu, A. N., 2014, Quantification of total organic carbon content in shale source rocks: an Eagle Ford case study, *Unconventional Resources Technology Conference*.

Asquith, G., 2014, Log analysis of hydrocarbon-bearing shales: AAPG 2015 Course Notes.

Avseth, P., and Carcione, J., 2015, Rock-physics analysis of clay-rich source rocks on the Norwegian Shelf, *The Leading Edge*, 34(11), 1340-1384.

Bowker, K. A., 2007, Barnett Shale gas production, Fort Worth Basin: Issues and discussion: *AAPG Bulletin*, 91(4), 523-533.

Boyce, M.L. 2010. Sub-surface stratigraphy and petrophysical analysis of the middle Devonian interval of the central Appalachian basin; West Virginia and southwest Pennsylvania, Doctoral dissertation.

Boyce, M. L., and Carr T.R., 2010, Stratigraphy and petrophysics of the Middle Devonian black shale interval in West Virginia and Southwest Pennsylvania, *Search and discovery article # 10265*.

Bruner, K., and Smosna, R., 2011, A comparative study of the Mississippian Barnett Shale, Fort Worth Basin, and Devonian Marcellus Shale, Appalachian Basin:

US Department of Energy.

Castagna, J. P., M. L. Batzle, and R. L. Eastwood, 1985, Relationships between compressional-wave and shear-wave velocities in clastic silicate rocks, *Geophysics*, 50, 571581.

Castagna, J. P., and Swan, H.W., 1997, Principles of AVO crossplotting, *The Leading Edge*, Society of Exploration Geophysicists, 17, 337342.

Carcione, J., and Avseth P., 2014, Rock-physics templates for hydrocarbon source rocks, Report for Tullow Oil plc.

Charsky, A, and Herron, M, 2014, Quantitative analysis of kerogen and mineralogy in shale cuttings by Diffuse Reflectance Infrared Fourier Transform Spectroscopy, SPWLA 55th Annual Logging Symposium, Cambridge USA.

Chaveste, A., Zhao, Z., Altan, S., and Gaiser, J., 2013, Robust rock properties through PP-PS processing and interpretation Marcellus Shale: *The Leading Edge*, 32(1), 86-92.

Chopra, S., Alexeev, V., Sudakhar, V., 2003, High-frequency restoration of surface seismic data, *The Leading Edge*, 22(8), 730-738.

Coyle, S., and K. T. Spikes, 2014, Rock-type model characterization of composition and fabric the Haynesville Shale: Expanded Abstracts of the 84th Annual Meeting of the SEG, 28402844.

Crain, E. R., and Holgate, D., 2014, A 12-step program to reduce uncertainty in kerogen-rich reservoirs, CSPG-CSEG-CWLS GeoConvention.

Curtis, M.E., R.J. Ambrose, C.H. Sondergeld, and C.S. Rai, 2011, Investigating the microstructure of gas shales by FIB/SEM tomography and STEM imaging, University of Oklahoma.

Energy Information Administration, 2016, Drilling Productivity Report, January 2016.

Engelder, T., Lash, G. G., and Uzcategui, R., 2009, Joint sets that enhance production from Middle and Upper Devonian gas shales of the Appalachian Basin, AAPG Bulletin, 93, 857889.

Enomoto, C. B., J. L. Coleman, Jr., J. T. Haynes, S. J. Whitmeyer, R. R. McDowell, J. E. Lewis, T. P. Spear, and C. S. Swezey, 2011, Geology of the Devonian Marcellus Shale - Valley and Ridge Province, Virginia and West Virginia: A Field Trip Guidebook for the American Association of Petroleum Geologists Eastern Section Meeting: Openfile report, 20121194.

Godfrey, R., and Bachrach, R., 2008, Seismically guided fracture characterization, CSEG RECORDER, 33(3), 30-36.

Gray, D., 2003, PS converted-wave AVO, CSEG Technical Abstracts.

Guo, Z., Chapman, M., and Li, X., 2012, A shale rock physics model and its application in the prediction of brittleness index, mineralogy, and porosity of the Barnett Shale. 82nd Annual International Meeting, SEG, Expanded Abstracts.

Jiang, M., and K. T. Spikes, 2011, Pore-shape and composition effect on rock-physics modeling in the Haynesville Shale, 81st Annual International Meeting, SEG,

Expanded Abstracts.

Jiang, M., and K. T. Spikes, 2012, Estimation of the porosity and pore aspect ratio of the Haynesville Shale using the self-consistent model and a grid search method, 82nd Annual International Meeting, SEG, Expanded Abstracts.

Hampson, D., and Russell, B., 2013, Joint simultaneous inversion of PP and PS angle gathers, CSEG RECORDER, 38, 32-39.

Hardage, B., M. deAngelo, and D. Sava., 2011, Marcellus shale geophysics. Bureau of Economic Geology, UT Austin. RPSEA Meeting.

Jarvie, D. M., R. J. Hill, T. E. Ruble, and R. M. Pollastro, 2007, Unconventional shale-gas systems: the Mississippian Barnett Shale of North-Central Texas as one model for thermogenic shale-gas assessment: AAPG Bulletin, 91, 475-499.

Kennett, B.L.N., 1983, Seismic Wave Propagation in Stratified Media: Cambridge University Press.

Kuila, U., and Prasad, M., 2013, Surface area and pore-size distribution in clays and shales, Geophysical Prospecting, 61(2), 341-362

Lash, G. G., and T. Engelder, 2011, Thickness trends and sequence stratigraphy of the Middle Devonian Marcellus Formation Appalachian Basin: Implications for Acadian foreland basin evolution: AAPG Bulletin, 95, 61-103.

Loucks, R. G., R. M. Reed, S. C. Ruppel, and U. Hammes, 2012, Spectrum of pore types and networks in mudrocks and a descriptive classification for matrix-related mudrock pores: American Association of Petroleum Geologists Bulletin, v.

96, p. 10711098.

Luker, A., 2012, A comparison of sequence stratigraphy and mineralogical variations associated with total organic carbon in the Marcellus Formation: Washington County, Pennsylvania, MS Thesis, University of Houston.

Mavko, G., T. Mukerji, and J. Dvorkin, 2009, *The rock physics handbook*: Cambridge University Press, 2nd ed.

Milliken, K. L., Rudnicki, M., Awwiller, D. N., and Zhang, T., 2013, Organic matter-hosted pore system, Marcellus Formation (Devonian), Pennsylvania, *AAPG Bulletin*, 97(2), 177-200.

Mondt, J.C. (1993) Use of dip and azimuth horizon attributes in 3D seismic interpretation. *SPE Paper 20943-PA*, 253-257.

Moyano, B., K. T. Spikes, T. A. Johansen, and N. H. Mondol, 2012, Modeling compaction effects on the elastic properties of clay-water composites, *Geophysics*, 77, D171D183.

Passey, Q.R., S. Creaney, J.B. Kulla, F.J. Moretti, and J.D. Stroud, 1990, A practical model for organic richness from porosity and resistivity logs: *AAPG Bulletin*, 74, 1777-1794.

Perez, M., and Cho, D., 2014, Brittleness revisited, *GeoConvention: Focus*.

Piotrowski, R., and Harper, J., 1979, Black shale and sandstone facies of the Devonian Catskill clastic wedge in the subsurface of Western Pennsylvania: US Department of Energy.

Prasad, M., and Zargari, S., 2014, Porosity evolution in oil-prone source rocks: SEG Annual Meeting Conference.

Qin, X., 2013, Vp/Vs relations of organic-rich shales, MS Thesis, University of Houston.

Qin, X., Han, D., and Zhao, L., 2014, Rock physics modelling of organic-rich shales with different maturity levels: SEG Annual Meeting Conference.

Rebec, T., and Zhao, Z., 2013, Complementary role of multi-component and conventional 3D seismic for risk reduction in unconventional resource plays a Marcellus Shale example, SPE Unconventional Resources Technology Conference.

Rickman, R., 2008, A practical use of shale petrophysics for stimulation design optimization: All shale plays are not clones of the Barnett shale, SPE Annual Technical Conference and Exhibition, 21-24 September 2008, Denver, Colorado, USA, SPE 115258.

Rowan, E. L., Engle, M. A., Kirby, C. S., and Kraemer, T. F., 2011, Radium Content of Oil- and Gas-Field Produced Waters in the Northern Appalachian Basin (USA): Summary and Discussion of Data, USGS, Scientific Investigations Report 20115135.

Ruiz, F., and Azizov, I., 2011, Tight shale elastic properties using the soft-porosity and single aspect ratio models, 81st Annual International Meeting, SEG, Expanded Abstracts.

Russell, B., Hampson, D., Hirsche, K., and Peron, J., 2005, Joint simultaneous

inversion of PP and PS angle gathers: Crewes Research Report, 17, 1-14.

Russell, B., 2014, Prestack seismic amplitude analysis: An integrated overview, *Interpretation*, 2(2), 19-36.

Sayers, C. M., 2013, The effect of kerogen on the AVO response of organic-rich shales, *The Leading Edge*, 32(12), 1514-1519.

Schmoker, J., 1979, Determination of Organic Content of Appalachian Devonian Shales from Formation-Density Logs, *American Association of Petroleum Geologists Bulletin*, 63, 1504-1537.

Sharma, K. R., and Chopra, S., 2015, Identification of thin sweet spots in the Duvernay Formation of north central Alberta, 85th Annual International Meeting, SEG, Expanded Abstracts.

Sharma, K. R., and Chopra, S., 2015, Determination of lithology and brittleness of rocks with a new attribute, *The Leading Edge*, 34(5), 554.

Smith, T. M., C. M. Sayers, and C. H. Sondergeld, 2009, Rock properties in low-porosity/low permeability sandstones: *The Leading Edge*, 28(1), 4859.

Smith, L.B., and J. Leone, 2010, Integrated Characterization of Utica and Marcellus Black Shale Gas Plays, New York State, AAPG Search and Discovery Article # 50289.

Sondergeld, C., Ambrose, R. J., Rai, C. S., 2010, Micro-structural studies of gas shales, SPE Unconventional Gas Conference.

Stewart, R.R., Gaiser, J.E., Brown, J.R., and Lawton, D.C., 2002, Converted-wave seismic exploration: Methods: Geophysics, 67 (5), 1348-1363.

Varga, R., 2009, Using multicomponent seismic data to delineate hydrocarbon reservoirs: 2D-3C Willesden Green, Alberta and 3D-3C Manitou Lake, Saskatchewan, MS Thesis, University of Calgary.

Vernik, L., and Landis, C., 1996, Elastic anisotropy of source rocks: implications for hydrocarbon generation and primary migration: AAPG Bulletin, 80(4), 531544.

Vernik, L., and Milovac, J., 2011, Rock physics of organic shales: The Leading Edge, 30, 318323.

Vernik, L., and Khadeeva, Y., 2013, Rock physics of organic shale and its implications, GeoConvention: Integration.

Wang, G., 2012, Black Shale lithofacies prediction and distribution pattern analysis of Middle Devonian Marcellus Shale in the Appalachian basin, Northeastern U.S.A., PhD Dissertation, West Virginia University.

Wang, G., and Carr, T., 2013, Organic-rich Marcellus Shale lithofacies modeling and distribution pattern analysis in the Appalachian Basin, AAPG Bulletin, 79(12), 2173-2205.

Widess, M.B., 1973, How thin is a thin bed, Geophysics, 38, 1176-1180.

Yenugu, M., and Han, D.-H., 2013, Seismic characterization of kerogen maturity: An example from Bakken shale, SEG Technical Program Expanded Abstracts.

Yenugu, M., and Vernik, L., 2015, Constraining seismic rock-property logs in

organic shale reservoirs, *The Leading Edge*, 34(11), 1326-1331.

Yilmaz, O., 2001. *Seismic data analysis: processing, inversion, and interpretation of seismic data*, Series: Investigations in Geophysics, no. 10, Doherty, S. F., ed., SEG, Tulsa.